Ultrasonic Pulse Wave Imaging for *in vivo* Assessment of Vascular Wall Dynamics and Characterization of Arterial Pathologies

Ronny X. Li

Submitted in partial fulfillment of the
requirements for the degree of
Doctor of Philosophy
in the Graduate School of Arts and Sciences

COLUMBIA UNIVERSITY

2016

© 2016

Ronny Li

All Rights Reserved

ABSTRACT

Ultrasonic Pulse Wave Imaging for *in vivo* Assessment of Vascular Wall Dynamics and Characterization of Arterial Pathologies

Ronny Li

Arterial diseases such as hypertension, carotid stenosis, and abdominal aortic aneurysm (AAA) may progress silently without symptoms and contribute to acute cardiovascular events such as heart attack, stroke, and aneurysm rupture, which are consistently among the leading causes of death worldwide. The arterial pulse wave, regarded as one of the fundamental vital signs of clinical medicine, originates from the heart and propagates throughout the arterial tree as a pressure, flow velocity, and wall displacement wave, giving rise to the natural pulsation of the arteries. The dynamic properties of the pulse wave are intimately related to the physical state of the cardiovascular system. Thus, the assessment of the arterial wall dynamics driven by the pulse wave may provide valuable insights into vascular mechanical properties for the early detection and characterization of arterial pathologies.

The focus of this dissertation was to develop and clinically implement Pulse Wave Imaging (PWI), an ultrasound elasticity imaging-based method for the visualization and spatio-temporal mapping of the pulse wave propagation at any accessible arterial location. Motion estimation algorithms based on cross-correlation of the ultrasound radio-frequency (RF) signals were used to track the arterial walls and capture the pulse wave-induced displacements over the cardiac cycle. PWI facilitates the image-guided measurement of clinically relevant pulse wave features such as

propagation speed (pulse wave velocity, or PWV), uniformity, and morphology as well as derivation of the pulse pressure waveform.

A parametric study investigating the performance of PWI in two canine aortas *ex vivo* and 10 normal, healthy human arteries *in vivo* established the optimal image acquisition and signal processing parameters for reliable measurement of the PWV and wave propagation uniformity. Using this framework, three separate clinical feasibility studies were conducted in patients diagnosed with hypertension, AAA, and carotid stenosis.

In a pilot study comparing hypertensive and aneurysmal abdominal aortas with normal controls, the AAA group exhibited significantly higher PWV and lower wave propagation uniformity. A "teetering" motion upon pulse wave arrival was detected in the smaller aneurysms (< 5 cm in diameter) but not in the larger aneurysms (> 5.5 cm in diameter). While no significant difference in PWV or propagation uniformity was observed between normal and hypertensive aortas, qualitative differences in the pulse wave morphology along the imaged aortic segment may be an indicator of increased wave reflection caused by elevated blood pressure and/or arterial stiffness.

Pulse Wave Ultrasound Manometry (PWUM) was introduced as an extension of the PWI method for the derivation of the pulse pressure (PP) waveform in large central arteries. A feasibility study in 5 normotensive, 9 pre-hypertensive, and 5 hypertensive subjects indicated that a significantly higher PP in the hypertensive group was detected in the abdominal aorta by PWUM but not in the peripheral arteries by alternative devices (i.e. a radial applanation tonometer and the brachial sphygmomanometer cuff). A relatively strong positive correlation between aortic PP and both radial and brachial PP was observed in the hypertensive group but not in the normal and pre-hypertensive groups, confirming the notion that PP variation throughout the arterial tree may not be uniform in relatively compliant arteries.

The application of PWI in 10 stenotic carotid arteries identified phenomenon such as wave convergence, elevated PWV, and decreased cumulative displacement around and/or within regions of atherosclerotic plaque. Intra-plaque mapping of the PWV and cumulative strain demonstrated the potential to quantitatively differentiate stable (i.e. calcified) and vulnerable (i.e. lipid) plaque components. The lack of correlation between quantitative measurements (PWV, modulus, displacement, and strain) and expected plaque stiffness illuminates to need to consider several physiological and imaging-related factors such as turbulent flow, wave reflection, imaging location, and the applicability of established theoretical models *in vivo*.

PWI presents a highly translational method for visualization of the arterial pulse wave and the image-guided measurement of several clinically relevant pulse wave features. The aforementioned findings collectively demonstrated the potential of PWI to detect, diagnose, and characterize vascular disease based on qualitative and quantitative information about arterial wall dynamics under pathological conditions.

Table of Contents

List of Figures ………………………………………………………………………….. v

List of Tables ………………………………………………………………………... xxv

Acknowledgements …………………………………………………………………….. xxviii

Chapter 1 Background, Motivation, and Clinical Significance of the Arterial Pulse Wave …………………………………………………………………….. 1

1.1 Vascular Mechanics and Arterial Stiffness ………………………………… 1

1.1.1 Vascular disease ………………………………………………….. 1

1.1.2 Pathophysiology of arteries ………………………………………. 4

1.1.3 Clinical significance of arterial elasticity and stiffness …………….. 6

1.2 The Arterial Pulse Wave …………………………………………………. 7

1.2.1 Pulse wave components ………………………………………….. 9

1.2.2 Pulse wave velocity ………………………………………………. 11

1.2.3 Wave reflections ………………………………………………….. 12

1.3 Current Measurement Techniques ………………………………………... 14

1.3.1 Applanation tonometry …………………………………………… 14

1.3.2 Imaging-based methods …………………………………………... 16

Chapter 2 Ultrasound Imaging and Its Use for Arterial Pulse Wave Assessment … 18

2.1 Vascular Ultrasound ……………………………………………………… 18

2.1.1 Diagnostic ultrasound imaging of the arteries ………………………. 19

2.1.2 Conventional vs. plane wave ultrasound architectures ……………... 20

2.2 Ultrasound Elasticity Imaging ……………………………………………. 23

2.2.1 Speckle tracking ………………………………………………….. 24

2.2.2 Arterial applications of ultrasound elasticity imaging ……………… 25

2.3 Pulse Wave Imaging (PWI) ………………………………………………. 26

2.3.1 PWI methodology and advantages ………………………………….. 26

2.3.2 History of PWI …………………………………………………… 29

Chapter 3 Performance assessment and optimization of the PWI method ……… 30

3.1 Introduction …………………………………………………………………. 30

3.1.1 Considerations for performance assessment and optimization ……... 30

3.1.2 Theoretical framework for the tradeoff between spatial and temporal resolution ………………………………………………………………. 31

3.2 Parametric Study Design ……………………………………………………. 32

3.2.1 *Ex vivo* experiments ……... 32

3.2.2 *In vivo* study …………………………………………………… 35

3.3 Results ………………………………………………………………………. 38

3.3.1 *Ex vivo* results ……... 38

3.3.2 *In vivo* results ……………………………………………………….. 42

3.4 Discussion and Conclusions ………………………………………………… 44

Chapter 4 Feasibility Study in Hypertensive and Aneurysmal Human Aortas …… 49

4.1 Introduction …………………………………………………………………. 49

4.1.1 Background on hypertension (HTN) ………………………………... 49

4.1.2 Background on abdominal aortic aneurysm (AAA) ………………… 50

4.2 Study Design ……………………………………………………………….... 51

4.2.1 Patient recruitment and exclusion criterion …………………………. 51

4.2.2 Data acquisition ……………………………………………………... 52

4.2.3 Data processing ……………………………………………………... 53

4.3 Results ………………………………………………………………………. 54

4.3.1 Qualitative results …………………………………………………..... 54

4.3.2 Quantitative results – PWV and r^2 ……………………...................... 60

4.4 Discussion and Conclusions ………………………………………………… 62

Chapter 5 Central pulse pressure measurement using Pulse Wave Ultrasound Manometry (PWUM) ……………………………………………………. 68

5.1 Introduction …………………………………………………………………. 68

5.1.1 Clinical significance of central pulse pressure ……………………… 69

5.1.2 Current measurement techniques ……………………...................... 69

5.1.3 PWUM methodology ……………………………………………….. 70

5.2 Methods and Study Design ………………………………………………… 72

5.2.1 Brachial sphygmomanometry ……………………………………… 72

5.2.2 PWUM 73
5.2.3 Radial applanation tonometry 75
5.3 Results 76
5.3.1 Radial and aortic pulse pressure waveforms 76
5.3.2 Quantitative results 77
5.4 Discussion and Conclusions 79
Chapter 6 Pulse Wave Imaging in Carotid Artery Stenosis Human Subjects 83
6.1 Introduction 83
6.1.1 Clinical challenges in plaque detection and stroke prediction 84
6.1.2 Characteristics of vulnerable vs. stable plaques 86
6.1.3 Imaging-based for plaque characterization 88
6.2 Methods: Pulse Wave Imaging of stenotic carotid arteries 89
6.2.1 Piece-wise PWI for regional PWV and modulus mapping 90
6.2.2 Intra-plaque PWV and modulus mapping using plane wave ultrasound 94
6.2.3 Intra-plaque cumulative displacement and strain mapping 95
6.3 Methods: Study Design 97
6.3.1 *In vivo* study in carotid stenosis patients 97
6.3.2 Patient undergoing carotid endarterectomy (CEA) 98
6.3.3 Quantitative measurements 99
6.4 Results 100
6.4.1 PWV, modulus and cumulative displacement maps 100
6.4.2 Intra-plaque displacement, strain, PWV, and modulus maps 108
6.4.3 Quantitative results 112
6.5 Discussion and Conclusions 117
Chapter 7 Summary and Ongoing Work 124
7.1 Summary and Key Findings 124
7.2 Towards Clinical Implementation of PWI 126
7.2.1 Improved B-mode quality 126
7.2.2 Automated processing 127
7.2.3 Real-time PWI 128

7.3 Unsupervised Machine Learning of PWI Parameters ………………………. 129
    7.3.1 Machine learning for clinical data analysis and medical diagnosis … 130
    7.3.2 Proposed methods: Pulse wave feature extraction ………………….. 131
    7.3.3 Proposed methods: Unsupervised learning …………………………. 134
    7.3.4 Preliminary results ………………………………………………….... 138

Bibliography ……………………………………………………………………………. 141

Appendix Full derivation of tradeoff between spatial and temporal resolution ………... 173

List of Figures

Figure 1.1 Diagram of the major arteries. The aorta is the main artery of the human body, originating from the left ventricle of the heart and ascending into the sternum before forming the aortic arch and descending down past the thorax (i.e. thoracic aorta) into the abdomen (i.e. abdominal aorta). The coronary arteries supply blood to the heart while the carotid arteries, which supply blood to the brain, branch from the aortic arch. The renal arteries branch from the descending aorta and supply blood to the kidney, and the abdominal aorta branches into the iliac and femoral arteries supplying blood to the hips, legs, and lower extremities. Source: *International Registry of Acute Aortic Dissection*. ………………………………………………………. 2

Figure 1.2 Histological structure of the arterial wall, which is primarily composed of three layers that surround the luminal cavity. The intima is comprised of a single layer of endothelial cells embedded in an extracellular matrix. The media, separated from the intima by the internal elastic lamina, consists of smooth muscle cells, elastic laminae, and bundles of collagen and elastin fibers. The outermost layer, the adventitia, contains dense fibroelastic issue, nutrient vessels, and nerves. Source*: Callanan et al* 2011. ………………... 5

Figure 1.3 Simplified animation depicting the pulse wave-induced arterial wall expansion. (a) Each left ventricular contraction expels a volume of blood into the arterial tree. (b-d) The large elastic arteries distend to absorb kinetic energy of the flowing blood and buffer the increase in pressure, causing the pulse wave to propagate as a pressure and flow velocity wave through the circulation and giving rise to the natural pulsation of the arteries. Source: *www.goldiesroom.org*. 8

Figure 1.4 Pressure and velocity pulse waveforms in the aorta and arterial branches of a dog, demonstrating the variation in the pulse wave morphology due to the sophisticated nature of the arterial tree. *Source:* Ku 1997, *Blood flow in Arteries*. …………………………………………………………………. 10

Figure 1.5 A simplified illustration of wave reflection in the aorta. The forward wave originates from the heart and propagates down the aorta until it gets partially reflected at the aortic bifurcation and other downstream sites. The reflected wave travels back towards the heart and merges with the next cycle's forward wave, forming the composite pulse waveform. Source: Adapted from *Complior Info Center*. ………………………………………….......... 13

Figure 1.6 Implementation of the two-site method for PWV measurement using applanation tonometry entails measuring the travel time (Δt) and distance (ΔL) of the pressure waveform between two remote sites, commonly the carotid and femoral arteries. Source: *Cardiac Imaging Group, University of Queensland, Australia*. ………………………………............................. 15

Figure 2.1 Triplex mode sonography combines B-Mode ultrasound with pulsed-wave (PW) Doppler and color flow imaging in order to image arterial structure and blood flow simultaneously. The light blue trapezoid in the image represents the CFI area, while the light blue lines in the lumen of the artery represents the sample gate at which the PW Doppler flow spectrum is measured. ………………………………………………………………... 20

Figure 2.2 A conventional ultrasound imaging sequence involves sweeping a transmit-focused beam across the imaged area, reconstructing the image line by line. Typically, up to 256-512 scan lines are used to generate the full image, depending on the size of the transducer array. ……………………………… 21

Figure 2.3 In the plane wave ultrasound architecture, all transducer elements are excited at once, sending a single plane wave into the tissue. The image is reconstructed using delay-and-sum beamforming techniques. ……………... 22

Figure 2.4 Speckle tracking for arterial wall motion estimation on one ultrasound scan line. The displacement (i.e. shift) of the vessel walls can be quantified by locating the peak of the normalized cross-correlation function between a reference window (red rectangle) within the wall in a given frame and a larger comparison window (purple dashed rectangle) containing the wall in the next frame. ………………………………………………………………… 25

Figure 2.5 Block diagram of the Pulse Wave Imaging (PWI) method on a normal human aorta *in vivo*. *(A)* A sequence of RF frames is acquired at the minimum depth required to visualize both walls of the artery of interest. *(B)* A 1D normalized cross-correlation-based motion estimation method (Luo and Konofagou 2010) is used on the RF signals to compute the inter-frame axial (i.e. parallel to the ultrasound beams) displacements in the arterial walls. The displacement amplitudes are normalized by multiplying by the frame rate. The arrival of the pulse wave induces positive (i.e. towards the transducer) displacements in the anterior wall and negative (i.e. away from the transducer) displacements in the posterior wall. The white arrows indicate the propagation of the wavefront along the anterior wall. *(C)* The anterior wall is manually segmented (red dotted line) in the first frame of the acquisition sequence, and this trace is automatically updated in subsequent frames based on the estimated displacements. *(D)* The anterior wall motion is spatio-temporally mapped over one cardiac cycle by plotting the displacements in the wall trace over time. *(E)* The normalized displacement waveform at three scan line positions along the anterior wall, corresponding to the light gray, dark gray, and black lines in *(D)*, are shown. The time point corresponding to a characteristic tracking feature (e.g. the 50% upstroke as indicated by the blue dots) is automatically detected in the waveform at each position. *(F)* Linear regression is performed on the spatio-temporal variation of the characteristic time points along the imaged segment to obtain the slope as the PWV and the coefficient of determination r^2 as an index of propagation uniformity. …………………………………… 27

Figure 3.1 Freshly excised canine aortas were used for the *ex vivo* experiments. ……... 33

Figure 3.2 Schematic of the setup used for *ex vivo* experiments. The canine aorta was held in place within a PBS-filled tank using plastic fittings. The peristaltic pump circulated pulsatile flow from the tank through the specimen and back into the tank. ……………………………………...................................... 33

Figure 3.3 Schematic for *in vivo* data acquisition in the abdominal aorta. In order to minimize rigid motion, each subject was asked for perform breath-holding during each 2.5-second acquisition. ……………………………………….. 36

Figure 3.4 A representative (a) normalized displacement waveform from the carotid artery of a normal (M, 26) subject is shown along with the corresponding (b) first and (c) second derivative curves. The six waveform features investigated in this study (zero-crossing, 25% upstroke, 50% upstroke, peak, maximum first derivative, and maximum second derivative) are indicated on the curves as color-coded markers. ……………………........................... 37

Figure 3.5 Consecutive PWI frames showing the propagation of the pump-induced pulse wave from left to right. The white arrows indicate the approximate position of the 50% upstroke in each frame. ……………………………….... 38

Figure 3.6 Effect of temporal upsampling on a spatio-temporal map of ex vivo data acquired using 128 scan lines (160 FPS). (A) Without upsampling, the r^2 is relatively low due to fewer discrete time samples. (B) With an upsampling factor of 2, the PWV value remains similar, however the r^2 increases dramatically. (C) An upsampling factor of 8 further increases the r^2. This demonstrates that a falsely low r^2 may result from insufficient frame rate, and may be improved by temporal upsampling. …………………………… 39

Figure 3.7 (a) Mean PWV, (b) SNR of the PWV measurement, and (c) magnitude of the r^2 value for each combination of scan line quantity and temporal upsampling factor in the first canine aorta. The value in each element of the matrices was obtained from PWV and r^2 measurements over 10 pulse cycles.

The black dashed box in (b) indicates the combinations of scan line quantity and temporal upsampling factor that yielded the highest PWV SNR, while combinations below the black line in (c) resulted in saturation of the r^2 magnitudes. ………………..……………………………………………… 40

Figure 3.8 (a) Mean PWV, (b) SNR of the PWV measurement, and (c) magnitude of the r^2 value for each combination of scan line quantity and temporal upsampling factor in the second canine aorta. The value in each element of the matrices was obtained from PWV and r^2 measurements over 10 pulse cycles. The black dashed box in (b) indicates the combinations of scan line quantity and temporal upsampling factor that yielded the highest PWV SNR, while combinations below the black line in (c) resulted in saturation of the r^2 magnitudes. ………………………………………………………………… 41

Figure 3.9 (a) SNR of the PWV measurement and (b) magnitude of the r^2 value averaged over N = 10 human carotid arteries and N = 10 human aortas *in vivo* from tracking each of the six waveform features indicated (i.e. zero-crossing, 25% upstroke, 50% upstroke, peak, maximum first derivative, and maximum second derivative). The PWV SNR and mean r^2 for each tracking feature were obtained from PWV and r^2 measurements over at least 10 cardiac cycles per subject. * denotes a tracking feature that yielded significantly higher PWV SNR and r^2 when compared to other tracking features using the Bonferri multiple comparisons test. ……………………... 43

Figure 4.1 (a) A normal aorta is generally cylindrical in geometry and exhibits a collagen-to-elastin ratio of ~ 1.58. The majority of AAAs occur at the infrarenal abdominal aorta (i.e. the segment below the renal artery branches) indicated by the white square. (b) During the early stages of AAA formation, elastin depredates while collagen production increases. Subsequent collagen degradation then causes the aneurysm to expand slowly. (c) Rapid AAA expansion may occur as a result of the collagen degradation. When the stress on the aortic wall exceeds its strength, AAA rupture may occur. …………… 51

Figure 4.2 Consecutive PWI frames (B-mode image overlaid with pulse wave-induced displacements) showing the propagation of the pulse wave along the anterior aortic wall in (a) a normal (23, M), (b) a hypertensive (42, F), and (c) a 6.0-cm diameter AAA (72, F) subject. The time stamp represents the time elapsed from the beginning of the PWI cine loop and is not intended to correlate with a particular point in the cardiac cycle. For the AAA case, the dynamic range of the normalized displacements was reduced for more clear visualization of the pulse wave propagation. ……………………………….. 55

Figure 4.3 (a, c, e) Spatio-temporal maps of the anterior aortic wall displacement in three normal subjects, ages (a) 23, (c) 31, and (e) 55. (b), (d), and (f) show the displacement waveforms at five locations along the imaged segment corresponding to the spatio-temporal maps in (a), (c), and (e), respectively. The blue squares represent the 50% upstroke in each waveform as it propagates along the wall. The PWV and r^2 values were obtained from the linear regression of the spatio-temporal variation of the 50% upstroke, represented by the black line in (a), (c), and (e). (a) and (b) correspond to the same subject shown in 4.2a. …………………………………………….. 56

Figure 4.4 (a, c, e) Spatio-temporal maps of the anterior aortic wall displacement in three hypertensive subjects (a) 42, (c) 77, and (e) 45. (b), (d), and (f) show the displacement waveforms at five locations along the imaged segment corresponding to the spatio-temporal maps in (a), (c), and (e), respectively. The blue squares represent the 50% upstroke in each waveform as it propagates along the wall. The PWV and r^2 values were obtained from the linear regression of the spatio-temporal variation of the 50% upstroke, represented by the black line in (a), (c), and (e). (a) and (b) correspond to the same subject shown in 4.2b. …………………………………………….. 57

Figure 4.5 (a, c, e) Spatio-temporal maps of the anterior aortic wall displacement in three AAA subjects, aged (a) 72 (6.0 cm AAA), (c) 80 (4.1 cm AAA), and (e) 66 (4.6 cm AAA). (b), (d), and (f) show the displacement waveforms at five locations along the imaged segment corresponding to the spatio-temporal maps in (a), (c), and (e), respectively. The blue squares represent the 50% upstroke in each waveform as it propagates along the wall. The upstroke markers that were not part of a positive linear trend were manually removed, and remaining makers were used for PWV and r^2 estimation via linear regression, represented by the black line in (a), (c), and (e). (a) and (b) correspond to the same subject shown in 4.2c. The pink lines in (a), (c), and (e) indicate the boundaries of the dilated aneurysmal segment as qualitatively approximated from the B-Mode images. …………………….... 58

Figure 4.6 PWI frames showing the “teetering” phenomenon (i.e. upward motion at the proximal end and downward motion at the distal end, as indicated by the red and blue arrows, respectively) of the aneurysmal segment that was observed in three out of the five AAA cases. (a) and (b) correspond to the cases in 4.5c/d and 4.5e/f, while (c) represents a 68 y.o. male with a 3.9 cmm AAA. The time stamp represents the time elapsed from the beginning of the PWI cine loop and is not intended to correlate with a particular point in the cardiac cycle. 60

Figure 4.7 PWV measurements averaged over at least five cardiac cycles for each subject. Standard deviations are shown as black error bars. 61

Figure 4.8 (a) PWV and (b) r^2 averaged over all subjects for each of the three subject groups. Standard deviations are shown as black error bars. The average PWV in all normal, hypertensive, and AAA subjects was 6.03 ± 1.68, 6.69 ± 2.80, and 10.54 ± 6.52 m/s, respectively. The average r^2 in all normal, hypertensive, and AAA subjects was 0.93 ± 0.05, 0.88 ± 0.11, and 0.46 ± 0.23, respectively. * denotes statistical significance with $p < 0.001$ measured using a two-sample t-test. 62

Figure 5.1 Estimation of the central aortic PP waveform using radial applanation tonometry. (a) A tonometer is placed on the surface of the wrist, above the radial artery. (b) The change in pressure is recorded over time to obtain the radial PP waveform. (c) A generalized transfer function is applied to derive the aortic PP waveform in which the reflected wave merges with the forward wave, creating an inflection point before the main peak. Source: Adapted from *Sphygmocor Info Sheet*. 70

Figure 5.2 Block diagram of the Pulse Wave Ultrasound Manometry (PWUM) method on a human aorta *in vivo*. Pulse Wave Imaging (PWI) provides local PWV measurements by tracking the estimated aortic wall displacement waveform. The incremental distension waveform (pink) obtained at the central scan line (pink squares) was used along with the PWV to arrive at the pulse pressure waveform based on the Laplace law and the Moens-Korteweg equation. …... 71

Figure 5.3 Custom applanation tonometry system consisting of (a) a noninvasive pulse tonometer (SPT-301, Millar Instruments, Houston, TX, USA), (b) an amplifier/pressure calibration unit (PCU-2000, Millar Instruments), and (c) a data acquisition device (NI USB-6501, National Instruments, Austin, TX, USA) attached to the back of the SonixTouch scanner (Analogic Corp., Peabody, MA, USA). ……………………….. 75

Figure 5.4 Representative radial and aortic pulse pressure waveforms, manually aligned by the foot of the wave, over a full cardiac cycle from (a) one normal subject (brachial BP 113/70), (b) one pre-hypertensive subject (brachial BP 136/87), and (c) one hypertensive subject (brachial BP 153/91). In each case, the times corresponding to the peak of the forward wave, reflected wave, and dicrotic notch in the radial PP waveform are indicated by blue lines and labels. ………………………………………………………………………. 76

Figure 5.5 Summary of the average blood pressure measurements for each subject group (Pre-HTN = pre-hypertensive, HTN = hypertensive). For each of the five pressure measurements, statistical significances amongst the subject groups were determined using two-way ANOVA (*** denotes $p < 0.001$, ** denotes $0.001 < p < 0.01$, and * denotes $0.01 < p < 0.05$). ……………...... 78

Figure 5.6 Aortic PP vs. (a) radial and (b) brachial PP for all subjects. In both plots, linear regression was performed on the data within each subject group. The greatest correlation between aortic PP and radial/brachial PP was observed in the hypertensive group. ……………………………………………….. 79

Figure 6.1 (a) Carotid artery anatomy and stenosis. The common carotid artery (CCA) bifurcates into the internal and external carotid arteries (ICA and ECA, respectively). Carotid artery stenosis is characterized by plaque buildup, typically around the carotid bifurcation. If a carotid plaque ruptures, it may cause a blood clot or travel upstream and get lodged in the small arteries in the brain, leading to a stroke. (b) In patients with severe blockage, a carotid endarterectomy may be performed to reduce the risk of stroke by surgically removing the plaque. Source: *Neurosurgeons of New Jersey*. …………........ 84

Figure 6.2 (a-c) Consecutive PWI frames showing pulse wave propagation along the anterior wall of a normal common carotid artery (M, 27 y.o.). (d) Manual segmentation and automated tracking of the inner and outer layers of the walls allow for measurement of the anterior wall thickness and inner diameter at each scan line position over time. Regional PWV estimation (e) generates a single PWV estimate across the imaged segment, while a piece-wise kernel outputs an array of PWV measurements that can be color-coded and overlaid onto the B-mode (g). (h) The incremental modulus along the artery can be derived based on the Modified Moens-Korteweg equation using the diameter, thickness, and PWV value at each scan line position. (i) The maximum cumulative displacement at each pixel in the anterior wall is computed by summing the inter-frame displacements from the beginning of the waveform upstroke (i.e. end diastole) to the point of maximum distension (i.e. peak systole), shown in Figure 6.3. …………………………. 92

Figure 6.3 Diameter (blue curve) and anterior wall thickness (brown curve) variation over the cardiac cycle at the central scan line position in the normal carotid artery shown in Figure 6.2, obtained by tracking the inner and outer layers of the walls over time. As the artery dilates to accommodate the increase in blood volume during systole, the sudden rise in intra-luminal pressure causes the wall to compress, decreasing the wall thickness. All modulus calculations were performed using the maximum diameter and associated anterior wall thickness (black line), thus representing the stiffness of the maximally distended artery. ……………………………………………….. 93

Figure 6.4 1D cumulative displacement estimation is performed within a region of interest (ROI) by summing the inter-frame displacements that are used to track each pixel in the axial direction over time. …………………………… 95

Figure 6.5 (a-c) Consecutive PWI frames showing pulse wave propagation along the anterior wall of a stenotic common carotid artery (F, 70 y.o.) exhibiting a bilateral plaque region. (d) Manual segmentation of the inner and outer layers of both walls (blue lines) accounted for the decrease in diameter and increase in thickness at the anterior wall plaque region, indicated by the red contour. (e) The spatio-temporal map from a single wall trace shows an absence of pulse wave-induced displacements in the plaque region (dashed lines). Regional PWV estimation (e) yielded a PWV and r^2 similar to those in the normal case in Figure 6.2, while the piece-wise measurements (f) revealed regions of high PWV and modulus immediately preceding and following the plaque (white arrows in g and h, respectively). (i) Decreased pulse wave-induced displacement within the plaque region and in the normal segment following it were observed on the cumulative displacement map … 101

Figure 6.6 Diameter (blue curve) and anterior wall thickness (brown curve) variation over the cardiac cycle in the stenosis case from Figure 6.5 at (a) a point in the normal wall preceding the plaque, and (b) a point within the plaque. The black line indicates maximum distension (i.e. greatest diameter), which does not occur at the same point in the cardiac cycle for the normal wall and the stenotic region. …………………………………………………………... 103

Figure 6.7 (a) B-Mode from the right CCA of a 72-y.o. female (50-79% stenosis) containing atherosclerotic lesions on both the anterior and posterior walls (white arrows). (b) Decreased cumulative displacement was observed in the anterior wall plaques (white arrows). The presence of the acoustic shadow (pink arrow) obstructing a portion of the posterior wall suggests that the plaque directly above is moderately calcified. (c) The PWV map reveals a region where the wave appears to converge inside the plaque. (d) The modulus map shows a transition from soft to stiff between the plaque and the normal segment (white arrow). …………………………………………. 104

Figure 6.8 (a) B-mode image, (b) displacement map, (c) PWV map, and (d) modulus map from the right CCA of a 76-y.o. male obtained using a conventional ultrasound sequence. The pink arrow points to the acoustic shadow caused by the calcified posterior wall plaque, and the white arrows indicate regions of decreased displacement, pulse wave convergence, and a transition in modulus. The same location was scanned again during a 6-month follow up using a plane wave sequence (e-h), and similar results were observed. ……. 106

Figure 6.9 (a) CTA longitudinal cross-section of the right CCA in a 56-y.o. male taken 2 weeks prior to ultrasound imaging, which was performed using both a conventional sequence (b, d, f, h) and a plane wave sequence (c, e, g, i) on the same day. Two plaque regions on the anterior wall can be identified (labeled 1 and 2 in a-c), both causing acoustic shadows on the B-mode image (pink arrows in c). The displacement, PWV, and modulus maps (d-i) obtained using the two sequences provided very similar results. The white arrows indicate regions of decreased displacement, increased PWV, and increased modulus. The greater degree of calcification in plaque #2 is reflected by its larger acoustic shadow (c), higher brightness intensity on the CTA (a), and lower displacement (d, e). PWV and modulus maps were only computed for plaque #1 due to the lack of wave propagation through plaque #2. ………………………………………………………………………….. 107

Figure 6.10 (a) Enlarged view of plaque #1 from the CTA in Figure 6.9a. The intra-plaque cumulative displacements (b) appeared uniformly distributed within the plaque ROI, while regions of tissue compression (blue) and elongation (red) were observed on the cumulative strain map. (d) Multiple wall traces were generated for intra-plaque PWV and modulus mapping. The PWV map (e) shows regions of negative PWV (white arrows) in between regions of positive PWV that appear to correlate with the two calcified inclusions observed on the enlarged CTA image (a). The modulus map (f) appeared mostly uniform with a small region of increased modulus immediately before the plaque (white arrow). …………………………………………. 108

Figure 6.11 The CTA (a) from a 79-y.o. male undergoing CEA showed severely-calcified, high-grade stenosis at the carotid bifurcation. However, PWI was performed in the CCA (blue dashed box), where two smaller calcified regions were observed (white arrows) and confirmed by H&E staining of the resected CCA segment (white arrows in c and d). The calcifications appear to correlate with regions of slightly lower intra-plaque displacement (white arrows in e) and elongation (white arrows in f). These same regions are depicted as areas of alternating positive and negative PWV (g) and increased modulus (h) throughout the depth of the plaque. …………………. 109

Figure 6.12 (a) CTA showing a severely-calcified, high-grade stenosis (80-99%) at the carotid bifurcation in an 80-y.o. male generating a severe acoustic shadow (pink arrow in b). A highly-calcified white nodule was identified on the gross pathology image (blue dashed box in c), correlating with the echoreflective region of the plaque on the B-mode (red contour in b). The intra-plaque displacement (d) and strain (e) maps revealed regions of varying displacement and strain amplitude, while the intra-plaque PWV map showed a region of alternating positive and negative PWVs throughout the depth of the plaque at the distal end (white arrow in f). …………………. 110

Figure 6.13 (a) The B-mode image of the carotid bifurcation in a 75-y.o. male shows the plaque (red contour) situated at the bifurcation and extending into the proximal ICA. Acoustic shadowing (pink arrow) is observed. (b) An enlarged image of the plaque ROI (blue box in a) shows an echolucent region (red arrow) surrounded by an echogenic border indicative of the fibrous cap (white arrow). (c) Gross pathology reveals bilateral plaques with liquid-like fatty substance oozing from the plaque of interest (blue dashed box). The white calcified nodule (yellow) in the far wall plaque is likely the main contributor to the acoustic shadowing observed in (a). The intra-plaque cumulative displacement map (d) is mostly uniform, while the cumulative strain map (e) reveals compression in the solid fibrous cap (white arrow) and elongation in the liquid-like fatty region (red arrow). The intra-plaque PWV map (f) revealed a transition from negative PWV to positive PWV in the direction of wave propagation at all depths of the plaque. ………………. 111

Figure 6.14 Cumulative displacement, cumulative strain, and PWV of both the normal wall (a, c, e) and the plaque region (b, d, f) for the each of the stenosis patients (P1 – P10). A red bar denotes a severely calcified plaque, while a blue bar denotes a moderately calcified plaque and the orange bar represents the lipid-filled case presented in Figure 6.13. The green bars denote the normal control group. In the label for each subject, RCA = right carotid artery, LCA = left carotid artery, and Bif = a plaque that was located at the bifurcation. ** denotes statistical significance with $p < 0.001$ compared to the normal controls. …………………………………………………… 113

Figure 6.15 The percent change in (a) cumulative displacement, (b) cumulative strain, and (c) PWV of the plaque region compared to the normal wall in all 10 patients. A red bar denotes a severely calcified plaque, while a blue bar denotes a moderately calcified plaque and the orange bar represents the lipid case presented in Figure 6.13. In the label for each patient, RCA = right carotid artery, LCA = left carotid artery, and Bif = a plaque that was located at the bifurcation. …………………………………………………… 114

Figure 6.16 No significant difference in PWV was observed between the plaque cases (non-calcified/lipid, moderately calcified, and severely calcified) and the normal controls …………….. 115

Figure 6.17 (a) Cumulative displacement and (b) cumulative strain were computed within the normal carotid wall for the control group and within the 13 plaque regions for each of the stenosis patients. * denotes statistical significance with $p < 0.10$, while ** denotes statistical significance with $p < 0.05$ ………. 116

Figure 6.18 Compliance was computed based on the Bramwell-Hill model across the normal carotid segment for the control group and through 12 of the plaque regions for the stenosis patients. * denotes statistical significance with $p < 0.10$, while ** denotes statistical significance with $p < 0.05$ …...................... 116

Figure 7.1 Contrast in the compound method versus number of plane waves. Source: Montaldo *et al* 2009). ……………………………………………………. 127

Figure 7.2 A normal carotid artery segmented using semi-automated methods. ………. 128

Figure 7.3 Time-domain features of the displacement waveforms include (a) the delay in the absolute value of the maximum displacement between the anterior (top) and posterior (bottom) walls, (b) the time lapsed for the waveform to reach its peak displacement value starting from its zero-crossing point, and (c) the peak width, which is defined as the full-width half-maximum. …….. 132

Figure 7.4 Frequency-domain features include the frequency and power of the (a) first, (b) second, and (c) third highest-amplitude frequency components obtained using a Fast Fourier Transform. …………………………………………….. 133

Figure 7.5 Illustration of the PCA transformation. The original data is plotted in terms of features x_1 and x_2. PCA computes the orthogonal eigenvectors ϕ_1 and ϕ_2 as the first and second principal components and maps the data onto the principal components coordinate system. Source: *Imperial College London, Department of Computing, Intelligent Data Analysis and Probabilistic Inference course, Lecture 15.* …………………………………………….. 136

Figure 7.6 Illustration of the *k*-means clustering algorithm. (a) The 2D data is represented in terms of variables X and Y. In the context of PWI, X and Y can represent the first two principal components determined by PCA or any two pulse wave features (PWV, r^2, maximum displacement, peak width, etc.). Visual observation suggests that three distinct clusters exist. (b) Three cluster centroids (+’s) are randomly initialized in the X-Y space. (c) Each data point is assigned to a cluster based on the centroid it is closest to (i.e. minimum Euclidean distance). (d) New cluster centroids are computed using the newly assigned data points. (e) In the second iteration, the data points are re-assigned based on the newly computed cluster centroids. (f) After several iterations, the solution is achieved when no points are re-assigned (i.e. the within-cluster sum of squares is minimized) …………….. 137

Figure 7.7 PCA bi-plot showing the principal component representation of the 30-dimensional data set containing the pulse wave features from the left carotid arteries and abdominal aortas of 15 healthy subjects. Each red point represents either a carotid artery or an aorta, and each blue line represents the loading vector of one of the 30 pulse wave features. The orange box indicates a group of features exhibiting variance in the first (i.e. primary) principal component, while the green box indicates a group of features exhibiting variance in the second principal component. ……………………. 138

Figure 7.8 (a) Two highly correlated variables – maximum distension (MaxDist) and root-mean-square (RMS) vs. (b) two non-correlated variables – root mean square (RMS) and root mean square variability (RMSVar). ……………….. 139

Figure 7.9 *k*-means clustering in (a) the principal components domain and (b) the 2D domain represented by the PWV (in m/s) and the lag in peak displacement between the anterior and posterior walls (WallLagP, in ms). Each data point represents a subject, and the X's represent cluster centroids. ………………. 140

Figure A B-mode image of an *ex vivo* canine aorta acquired in the reverse scan orientation, used to illustrate the theoretical framework on the tradeoff between temporal and spatial resolution. In the field of view, the pulse wave (pink arrow) propagates in the same direction as that of beam sweeping (red arrow). The pulse wave is captured by beam 1 at time t_1 and reaches the lateral position insonicated by beam K at time $t_K = t_1 + \frac{N}{FR}$ where FR is the frame rate. ………………………………………………………………….. 141

List of Tables

Table 3.1 Scan line quantities (K) used along with their corresponding frame rates (FR) and PWV upper limits (PWV_{max}) as determined by Eqn. 3.1. The imaged segment length (L) is fixed under the assumption that the 38-mm wide linear array transducer is orientated exactly parallel to the specimen. ……………. 34

Table 5.1 Blood pressure categories defined by the American Heart Association. Source: *www.heart.org*. …………………………………………………………………. 73

Acknowledgements

Many thanks to:

- My advisor, Dr. Elisa Konofagou, for her constant support and guidance through the course of this dissertation.
- Our funding source, National Institutes of Health R01-HL098830, for, well, funding this work.
- Our clinical collaborators at New York Presbyterian Hospital and Columbia University Medical Center, for all their help in recruiting patients and providing clinical perspective:
    - *Department of Neurological Surgery*: Dr. E. Sander Connolly, Hope Poulos, Kimberly Farro, Dr. Jason Ellis, Dr. Chris Kellner
    - *Department of Anesthesiology*: Dr. Eric Heyer, Kaitlin Mallon
    - *Department of Vascular Surgery*: Dr. James McKinsey, Helen Galdieri
    - *Department of Cardiothoracic Surgery*: Dr. Michael Borger, Jackie Rodriguez
    - *Department of Pathology*: Dr. Charles Marboe
    - *Department of Radiology*: Dr. Elizabeth Hecht, Dr. Tony Wong, Dr. Sherelle Laifer-Narin, Lancelot Walker
    - *School of Dental Medicine*: Dr. Elena Sanz-Mareilles, Dr. Panos Papapanou
- Our collaborators at St. Luke's-Roosevelt Hospital Center, for their support and guidance during initial clinical feasibility studies:
    - Dr. Farooq Chaudhry, Dr. Sandhya Balaram, Debbie Kim, Daniel Pudpud, Gene Parks
- My lab mates at the Ultrasound and Elasticity Imaging Laboratory, for helpful discussion and great laughs:

    - Iason Apostolakis, Jianwen Luo, Jonathan Vappou, Sacha Nandlall, Danial Shahmirzadi, William Qaqish, Prathyush Narayanan, Isaac Jourard, Kristin Salomon, Jean Provost, Julien Grondin, Gary Hou, Ethan Bunting
- My committee members, for their time and dedication:
    - Dr. Gerard Ateshian, Dr. E. Sander Connolly, Dr. Andreas Hielscher, Dr. Andrew Laine
- My parents, for their endless love and support no matter what I do:
    - Gary Li, Yufang Zhao

Chapter 1

Background, Motivation, and Clinical Significance of the Arterial Pulse Wave

1.1 Vascular Mechanics and Arterial Stiffness

1.1.1 Vascular disease

Vascular disease encompasses any condition that affects the circulatory system, which is comprised of two primary types of vessels – veins and arteries – that transport blood throughout the body. This dissertation focuses on diseases of the arteries, which are responsible for carrying oxygenated blood from the heart to all parts of the body. The arterial tree (Figure 1.1) refers the large network of arteries that extend and branch throughout the anatomy [1]. Arterial disease can result in narrowing of the arteries supplying the heart (i.e. coronary artery disease), the brain (i.e. cerebrovascular disease), or the extremities (i.e. peripheral artery disease) [2]. A focal dilation (i.e. aneurysm) can also occur due to the degradation of the arterial wall [3], while elevated blood pressure in the arteries (i.e. hypertension) is a significant risk factor for heart disease, coronary artery disease, stroke, peripheral artery disease, and chronic kidney disease [4-9]. Because the circulatory system extends throughout the anatomy, vascular disease can affect all parts of the body. According to the Centers for Disease Control and Prevention, nearly one out of two people will suffer from vascular disease in his/her lifetime, and it is estimated that by 2024, vascular disease will be responsible for over 2 million deaths each year in America.

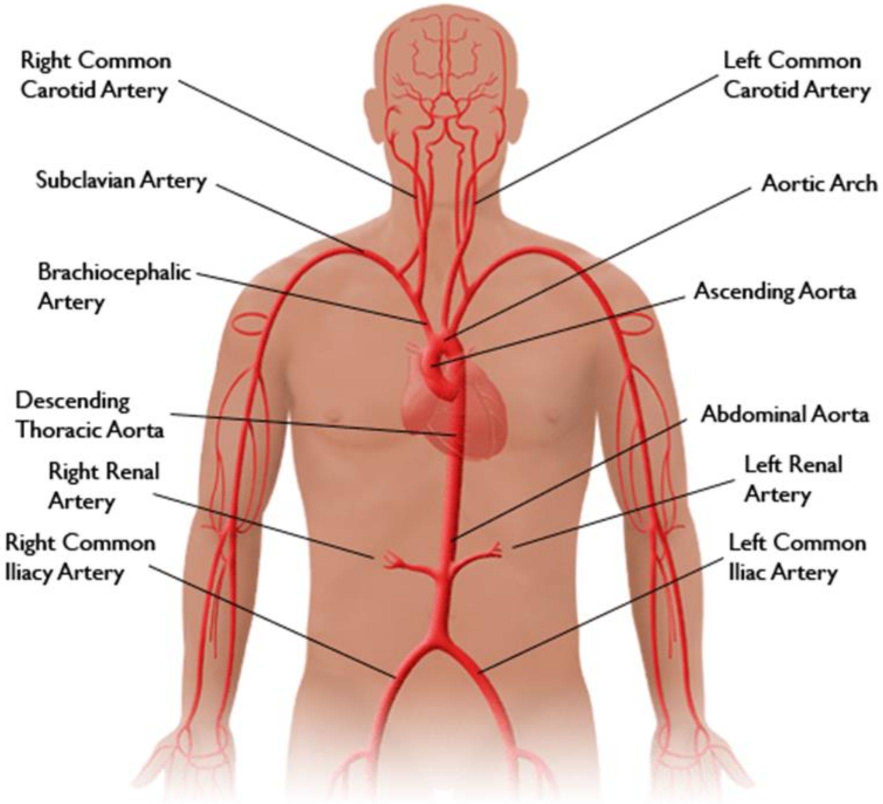
Right Common Carotid Artery
Left Common Carotid Artery
Subclavian Artery
Aortic Arch
Brachiocephalic Artery
Ascending Aorta
Descending Thoracic Aorta
Abdominal Aorta
Right Renal Artery
Left Renal Artery
Right Common Iliacy Artery
Left Common Iliac Artery

Figure 1.1: Diagram of the major arteries. The aorta is the main artery of the human body, originating from the left ventricle of the heart and ascending into the sternum before forming the aortic arch and descending down past the thorax (i.e. thoracic aorta) into the abdomen (i.e. abdominal aorta). The coronary arteries supply blood to the heart while the carotid arteries, which supply blood to the brain, branch from the aortic arch. The renal arteries branch from the descending aorta and supply blood to the kidney, and the abdominal aorta branches into the iliac and femoral arteries supplying blood to the hips, legs, and lower extremities. Source: *International Registry of Acute Aortic Dissection*.

Epidemiology and diagnosis of vascular disease

Many vascular diseases are lethal because they can develop asymptomatically and lead to acute cardiovascular events. Consequently, vascular diseases have often been labeled as “silent killers” [10-14]. For example, coronary artery disease (CAD) is characterized by atherosclerosis (i.e. the buildup of plaque) within the coronary arteries, restricting blood flow to the heart. This can occur without symptoms until the plaque ruptures and forms a clot, completely occluding blood flow through the coronary artery and resulting in a myocardial infarction. CAD is the number one cause of death in the U.S., affecting more than 13 million Americans [15]. Atherosclerosis can also occur in the carotid arteries, resulting in carotid artery stenosis [16]. Plaque rupture at this site may eliminate blood flow the brain and cause a stroke, which is the third leading cause of death in the U.S [17]. “Vulnerable” plaques (i.e. those prone to rupture) will be discussed in Chapter 6 of this dissertation.

While CAD and carotid stenosis result in arterial narrowing, an abdominal aortic aneurysm (AAA) is characterized by bulging of the artery walls. If the wall stress exceeds the wall strength [18, 19], the aneurysm will rupture, which carries up to a 90% mortality rate and is the 10th leading cause of death in the U.S [20]. Because most intact AAAs are asymptomatic and often cause no health problems, they frequently remain undiagnosed until the time of rupture. The mechanisms of AAA and their effects on arterial wall properties will be further discussed in Chapter 4.

Hypertension is one of the most common cardiovascular risk factors, affecting 1 in 3 adults in the U.S [21]. Although there exists a strong relationship between blood pressure and cardiovascular disease, it is unclear which hypertensive patients will experience future cardiovascular events and which will not [22]. Consequently, hypertension can progress silently over time, placing stress on several target organs and playing a major role in the development of a variety of cardiovascular complications [23]. The clinical assessment and management of hypertension, particularly in central arteries such as the aorta, will be discussed in Chapter 5.

Due to their silent nature, many vascular diseases are diagnosed during routine physical examinations for unrelated reasons. Oftentimes, vascular disease is discovered as a result of a life-threatening event such a heart attack or stroke. Thus, there is an important need to develop fast, low-cost, and reliable methods for early detection and screening of vascular disease. The scope of this dissertation focuses on diseases of the large conduit arteries, namely hypertension, AAA, and carotid atherosclerosis.

1.1.2 Pathophysiology of arteries

One of the key mechanical parameters used to describe an artery is its elasticity, or ability to distend in response to an increase in intraluminal pressure [24]. Compliance, defined as the change in arterial blood volume (ΔV) due to a given change in arterial blood pressure (ΔP), is one of the primary indices used to quantify arterial elasticity [25]. When healthy, the large conduit arteries (aorta, carotid, iliac, femoral, and brachial) are highly elastic, which allows them to buffer the oscillation in blood pressure caused by ventricular pumping. By distending and recoiling, these large arteries help convert intermittent blood flow from the ventricle into continuous blood flow in the vasculature. This is known as the Windkessel effect [24, 26, 27]. Assessment of the arterial wall elasticity is of great clinical interest due to its correlation with advanced atherosclerotic disease as well as aging and other risk factors for cardiovascular pathology [28].

The arterial wall is primarily composed of three layers that surround the luminal cavity – an inner layer of endothelial cells (tunica intima) surrounded by layers of collagen, elastin, and smooth muscle bundles (tunica media) and an outer layer (tunica adventitia) consisting of loose fibrous connective tissue [26, 29] (Figure 1.2). The mechanical integrity of the arterial wall is mainly determined by its matrix constituents, namely elastin, collagen, and smooth muscle [29]. Elastin is highly distensible and load-bearing at low pressures to provide reversible extensibility during cardiac loading, while collagen is 100-1000 times stiffer and load-bearing at high pressures to prevent structural failure [25, 30]. While smooth muscle cells contribute significantly to the mechanical behavior of small, muscular arteries, they contribute minimally to the mechanical behavior of large conduit arteries [31]. In fact, it is the high ratio of elastic laminae to smooth muscle cells that gives large conduit arteries their elastic properties. Thus, the elasticity of large arteries is primarily mediated by its collagen-to-elastin ratio [26].

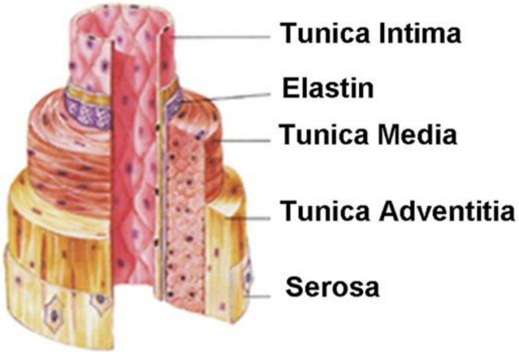

Figure 1.2: Histological structure of the arterial wall, which is primarily composed of three layers that surround the luminal cavity. The intima is comprised of a single layer of endothelial cells embedded in an extracellular matrix. The media, separated from the intima by the internal elastic lamina, consists of smooth muscle cells, elastic laminae, and bundles of collagen and elastin fibers. The outermost layer, the adventitia, contains dense fibroelastic issue, nutrient vessels, and nerves. Source*: Callanan et al* 2011.

Arterial wall tissue adapts to physiological and pathophysiological stimuli through an active process known as *vascular remodeling* that involves rearrangement of its microstructure as well as changes in mass (growth) and geometry (morphogenesis) [32]. In most cases, these structural changes lead to increased arterial stiffness. For example, vascular aging is strongly associated with elastin depletion and fragmentation as well as collagen deposition, which increases the collagen-to-elastin ratio and results in arterial stiffening [33]. Similarly, clinical observations of aortic aneurysm formation and atherosclerotic plaque buildup have identified biomechanical attributes resulting from wall restructuring that lead to increased arterial stiffness [3, 34].

The biological mechanisms associated with arterial stiffening are dependent on dynamic interactions between structural and cellular elements of the vessel wall as well as hemodynamic forces and external factors such as hormones, salt, and glucose regulation [35]. The elastin fibers are subject to proteolytic degradation and chemical alterations, while collagen deposition and degradation is a continuous process in the artery walls [36].

1.1.3 Clinical significance of arterial elasticity and stiffness

As large arteries lose their elasticity, the Windkessel effect is diminished, which elevates blood pressure and stimulates vascular remodeling. The relationship between arterial stiffness and cardiovascular risk has been well documented by numerous clinical longitudinal studies. Stiffening of large arteries such as the aorta and carotid arteries has been shown to be a strong predictor of coronary heart disease, congestive heart failure, and stroke in well-functioning older adults [37], all-cause and cardiovascular mortality in end-stage renal disease [38, 39], and all-cause and cardiovascular mortality, fatal stroke, and primary coronary events in hypertensive patients [40-42]. Besides functioning as a risk factor, increased arterial stiffness begins a negative feedback cycle that increases the mechanical load on the heart and accelerates heart failure [25].

Stiffening is not uniformly distributed throughout the arterial tree, tending to occur in the large conduit arteries rather than the peripheral arteries [35, 43]. Thus, the accurate and reliable quantification of large artery stiffness may have a widespread impact on the early detection, diagnosis, and prognosis of cardiovascular risk. While it is difficult to noninvasively assess the biological composition of the artery walls, the mechanical changes associated with vascular remodeling are manifested in the intrinsic dynamics of the cardiovascular system – abnormalities in arterial pulsatility may serve as markers for underlying disorders and aging [44-46]. From a clinical diagnosis perspective, the spatial and temporal characteristics of arterial pulsation can be evaluated using noninvasive medical imaging and sensor technologies. This dissertation seeks to investigate the effects of vascular pathology and arterial stiffening on one of the most fundamental phenomenon in circulation – the arterial pulse wave.

1.2 The Arterial Pulse Wave

The arterial pulse is the most fundamental sign of life, deeply rooted in thousands of years of ancient medicine [47]. It has been studied and interpreted dating back to 2500 B.C., when the Chinese Emperor Hoamti described a variety of pulses through three-finger palpation and correlated them to different physiological and pathological states [48]. Around 1000 A.D., medieval physician Avicenna's descriptions and observations revealed the understanding of the arterial pulse as a wave rather than an impact generated by a cylindrical tube [49]. This basic concept was later confirmed by William Harvey's discovery of greater circulation, and has formed the foundation for pulse wave studies in modern medicine [50]. Each heart contraction expels a volume of blood into the circulation, generating a pulse wave that originates at the left ventricle and travels throughout the vasculature, causing the arteries to expand [26, 29] (Figure 1.3). The propagation of the pulse wave is driven by the exchange of energy between the kinetic energy of the flowing blood and the potential energy of the elastic artery wall [51, 52].

The importance of the arterial pulse and its propagation has long been recognized, including in the following quotes:

"Since the information which the pulse affords is of so great importance, and so often consulted, surely it must be to our advantage to appreciate fully all it tells us, and to draw from it every detail that it is capable of imparting." – F.A. Mahomed 1872 [53].

"If we were able to read all the messages in the arterial pulse waves, then all we need for noninvasive diagnosis is to observe these waves in some conveniently located arteries. If the messages are clear and unequivocal, then the art of noninvasive diagnosis would have been moved ahead a big step." – Y.C. Fung 1997 [29].

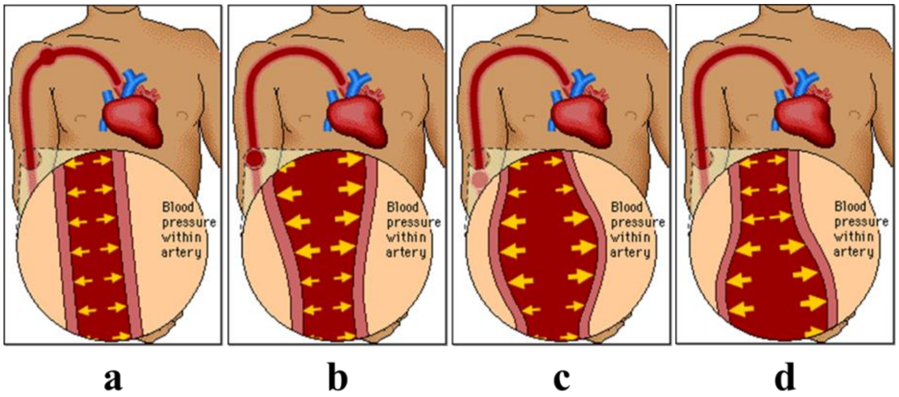
Blood pressure within artery
Blood pressure within artery
Blood pressure within artery
Blood pressure within artery
a
b
c
d

Figure 1.3: Simplified animation depicting the pulse wave-induced arterial wall expansion. (a) Each left ventricular contraction expels a volume of blood into the arterial tree. (b-d) The large elastic arteries distend to absorb kinetic energy of the flowing blood and buffer the increase in pressure, causing the pulse wave to propagate as a pressure and flow velocity wave through the circulation and giving rise to the natural pulsation of the arteries. Source: *Goldie's Room Online*.

As technological advancements led to novel methods of measuring and analyzing the arterial pulse wave, the correlation between cardiovascular pathophysiology and the behavior of the pulse wave became increasingly evident [54]. As previously mentioned, changes in the structure, function, and mechanical properties of the arterial wall tend to be indicative of risk factors for cardiovascular disease [55]. Thus, the ability to detect and monitor variations in the functional and physical properties of the arteries holds great potential to prevent and/or attenuate disease progression at a preclinical stage [56]. The potential of using features such as pulse wave shape, propagation speed, and amplitude to detect and characterize arterial diseases and infer the condition of the heart has been repeatedly demonstrated in literature [29, 42, 54, 57]. Clinical applications of pulse wave studies are generally aimed at detecting and explaining arterial pathologies such as atherosclerosis, stenosis, and aneurysm, locating sites that require surgical treatment, and inferring the condition of the heart [29]. Recent interest has also turned to the effect on pulse wave propagation of surgical interventions such as vascular stents and grafts [58].

1.2.1 Pulse wave components

The conduit arteries adapt to varying hemodynamic conditions by dilating to accommodate the pressure increase from ventricular ejection (i.e. systole) and contracting when the elastic energy accumulated during distension is released (i.e. diastole) [26, 59, 60]. Thus, at any given location in any conduit artery, the intraluminal pressure, blood flow velocity, and vessel diameter all vary in a pulsatile manner over time, giving rise to the pulse waveform. Thus, the pulse wave can be described as a pressure, flow velocity, and diameter wave [61, 62]. Due to branching, tapering, tethering, and viscous losses that occur throughout the arterial tree, the pressure and flow have characteristic pulsatile shapes that vary at different sites in the circulation (Figure 1.4). These differences in morphology arise due to wave reflections, which will be discussed in greater detail in Section 1.2.3.

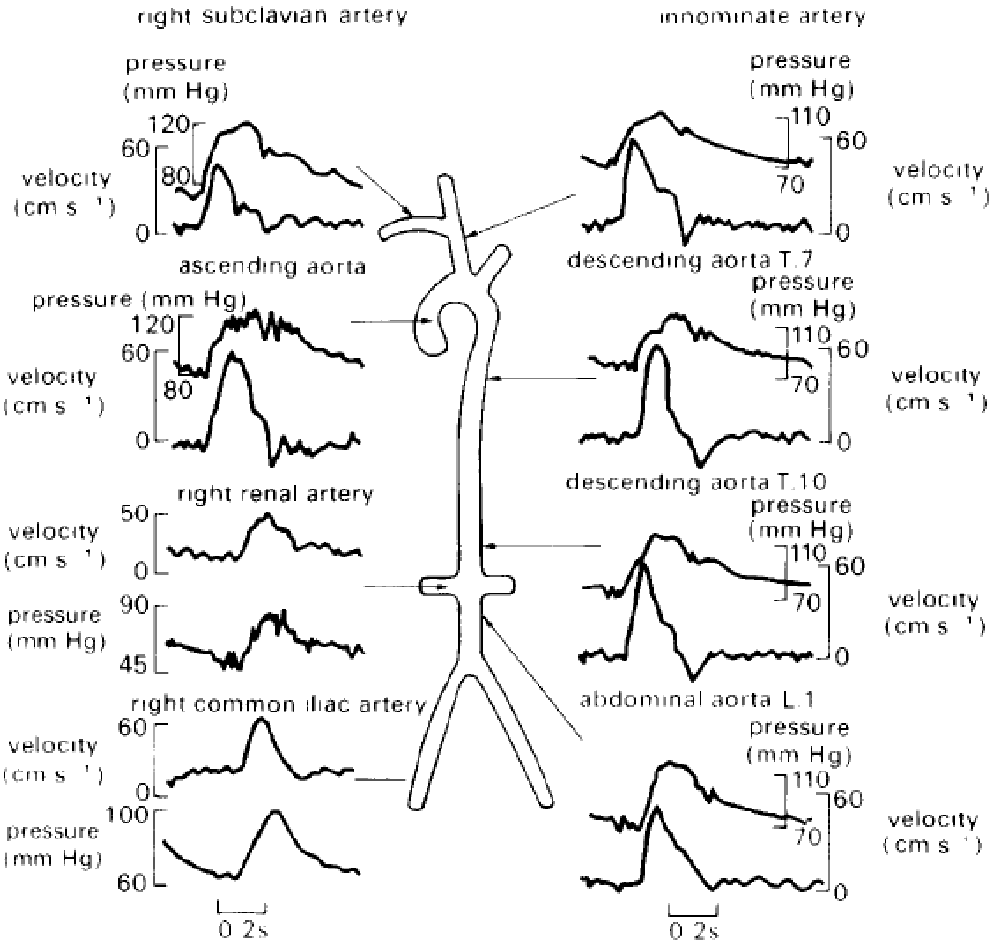

Figure 1.4: Pressure and velocity pulse waveforms in the aorta and arterial branches of a dog, demonstrating the variation in the pulse wave morphology due to the sophisticated nature of the arterial tree. *Source:* Ku 1997, *Blood flow in Arteries*.

While most of the methods currently used to observe the pulse wave focus on measuring either pressure, flow, or distension, a complete understanding would require the assessment of all three, preferably simultaneously. This is of particular importance for localized diseases such aneurysm and stenosis, where the inhomogeneity of the arterial wall may result in turbulent flow and non-uniform pressure gradients that in turn affect the wall motion [3, 63]. Although this dissertation primarily focuses on measurement and analysis of the pulse wave-induced arterial wall displacements, the derivation of arterial pulse pressure will be presented in Chapter 5 and flow-mediated changes in wall motion will be discussed on Chapter 6.

1.2.2 Pulse wave velocity

The pulse wave velocity (PWV) is the speed at which the pulse wave propagates throughout the arterial tree. Due to the aforementioned branching, tapering, and stiffness variations in the vasculature, PWV varies throughout the circulation [26, 29, 51]. The PWV in humans has been reported to fall anywhere within the 4-12 m/s range [64], although the actual velocity in any individual depends on the elastic condition of the arterial wall, which is affected by a variety of factors in both health and disease.

The interest in PWV stems from the realization that vascular changes lead to variations in arterial stiffness, which in turn affect the rate at which the pulse wave travels along the vessel [65]. Changes in the biomechanical properties of the arterial walls arising from disease and/or aging affect the morphology and speed of the pulse wave [51]. The PWV increases as the walls become stiffer, or less distensible, so that the state of the vessel can be described functionally by the PWV. As such, the PWV has become one of the most robust and widely used parameters for characterizing arterial mechanical properties [37, 66-69]. The theoretical basis for using PWV to determine arterial stiffness can be found in the Moens-Korteweg equation, which directly and quantitatively relates PWV to the Young's modulus of the artery:

$$PWV = \sqrt{\frac{Eh}{2\rho R(1-\nu^2)}} \, , \qquad [1.1]$$

where E is the incremental Young's modulus, ν is the and Poisson's ratio ($\nu \approx 0.49999$ for soft quasi-compressible tissues), R is the lumen radius, h is the wall thickness, and ρ is the density of the blood ($\rho \approx 1060$ kg/m^3).

In the early 20th century, British scientists Crighton Bramwell and Archibald Hill cited the Moens-Korteweg equation and proposed a series of substitutions relevant to the observable hemodynamic measures. The Bramwell-Hill model was formulated to describe the proportional variation of PWV to arterial wall tension and blood pressure, establishing the PWV as an indirect measure of the arterial wall elasticity:

$$PWV = \sqrt{\rho\left(\frac{\Delta A}{(A_{min} * \Delta P)}\right)}\ , \qquad [1.2]$$

Here, the expression $\Delta A/(A\_min * \Delta P\ )$ represents the vessel distensibility, expressed in terms of the minimum luminal area (A_{min}) the difference between the maximum and minimum luminal area (ΔA), and blood pressure (ΔP). The ρ in the Bramwell-Hill equation also represents the blood density.

1.2.3 Wave reflections

Reflections are a crucial component of arterial pulse wave propagation. Sections 1.2.1 and 1.2.2 touched on the variations in pulse wave shape and speed due to the heterogeneous nature of the arterial tree. The pulse wave originating at the left ventricle, known as the *forward wave*, is partially reflected back towards the heart at junctures of arterial bifurcation, tapering, and non-uniform mechanical properties (i.e. stiff inclusions due to elastin fragmentation and/or the onset of atherosclerosis) [70]. These *reflected waves* are integrated into the forward wave at different points in the cardiac cycle depending on the arterial location and stiffness. Thus, the waveform at any given site in the arterial tree is a combination of the forward wave and any reflected waves originating from further down the vasculature [26, 29].

Figure 1.5 presents a simplified illustration of wave reflection. The heart produces a forward wave that travels down the large aorta and gets reflected at the aortic bifurcation as well as less significant reflection sites further downstream. This reflected wave propagates back towards the heart and merges with the next cardiac cycle's forward wave, forming the composite pulse waveform. The issue of clinical importance is the point in the cardiac cycle at which the reflected and forward waves merge close to the heart. In young healthy individuals, the reflected wave usually returns in late systole or early diastole [71], aiding perfusion by pushing the blood through the coronary vessels. In older individuals with stiffer arteries and hence higher wave speed, the reflected wave travels faster and arrives earlier in the cardiac cycle, elevating systolic pressure and increasing the mechanical load against which the heart pumps [72, 73]. Thus, both the forward and reflected wave speeds are of clinical importance because they represent the stiffness of the artery.

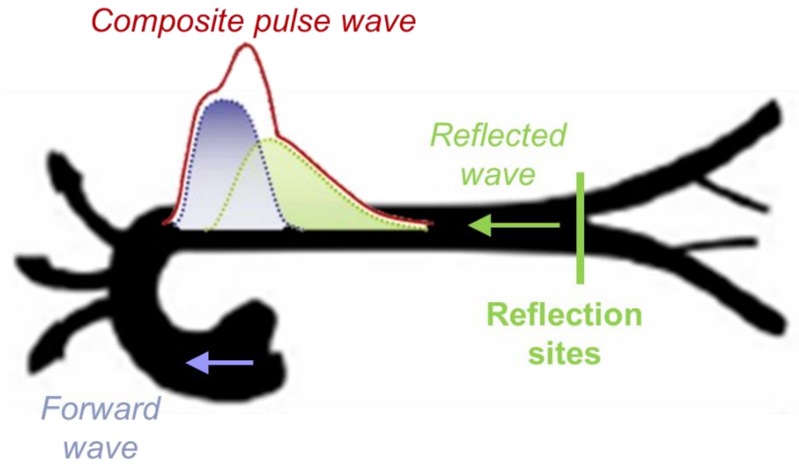

Figure 1.5: A simplified illustration of wave reflection in the aorta. The forward wave originates from the heart and propagates down the aorta until it gets partially reflected at the aortic bifurcation and other downstream sites. The reflected wave travels back towards the heart and merges with the next cycle's forward wave, forming the composite pulse waveform. Source: Adapted from *Complior Info Center*.

Reflected waves are also present in the common carotid arteries, as the carotid bifurcation is a significant reflection site [74]. Analysis of carotid wave reflection may be clinically useful for assessing of changes in cerebral vasomotor tone [74] and explaining increases in carotid intima-media thickness [75], both of which are significant predictors of cardiovascular mortality.

The separation of the composite pulse waveform into forward and backward components is an active area of research [76] that involves complex mathematical equations and simultaneous knowledge of the changes in pressure and flow velocity at the arterial site. This dissertation focuses on measurement and analysis of the wealth of information in the composite waveform rather than separation of the forward and reflected waves. However, the concept of wave reflection will be discussed throughout.

1.3 Current Measurement Techniques

The first arterial pulse wave studies were performed in the 19th century by French physiologist Etienne Marey, who used the sphygmograph to graphically trace and depict the differences in the arterial pulse pressure waveforms between the elderly and young adults [77]. Graphical pulse wave tracing gradually gave way to the cuff sphygmomanometer [67], which made clinical interpretation easier and has remained the gold standard for measuring blood pressure in the clinic. However, the study of the pulse waveform is undergoing a resurgence with the development of advanced computing technology [66] to improve reproducibility and reliability.

1.3.1 Applanation tonometry

Nowadays, the preferred method for recording the pulse waveform is applanation tonometry [47], which uses high fidelity force sensors to flatten the artery underneath the sensor. The force exerted on the sensor by the pulsating artery is converted into a calibrated electronic signal that depicts the approximated arterial pressure recording. Applanation tonometry is typically performed on superficial, easily accessible arteries such as the radial. It has also been used for deeper arteries such as the carotid and the femoral, however the accuracy and reproducibility of the recordings may be compromised by the soft tissue that intervenes between the skin and the anterior wall of the artery. The indirect derivation of the central aortic pressure waveform is possible using generalized empirical transfer functions [78] and will be discussed in greater detail in Chapter 5.

Based on the implementation shown in Figure 1.6, applanation tonometry has been used to measure PWV in virtually all large-scale longitudinal studies that use PWV as an index of arterial stiffness [37, 40-42, 69]. The travel time and distance of the pressure waveform between two remote sites, commonly the carotid and femoral arteries, are used for PWV measurement. The carotid-femoral PWV has been reported within the range of 6 - 7.5 m/s in healthy, middle-aged populations [79]. Such a technique suffers from major limitations, primarily arising from the fact that vascular elastic properties are changing throughout the arterial tree due to its varying geometry, surrounding environment, and composition of the vessel wall constituents [26, 80]. The carotid-femoral method produces a global estimate of the PWV averaged across the entire circulation, thus inherently lacking the sensitivity to detect variations in the *regional* arterial stiffness. This is a major pitfall because vascular diseases such as atherosclerosis and aneurysm only affect localized regions in the arterial tree [3, 19]. In addition, the carotid-femoral technique is prone to sizeable errors in the distance measurement [66, 81], which is performed extracorporeally. For these reasons, the PWV is currently not widely used as a diagnostic index despite its promise.

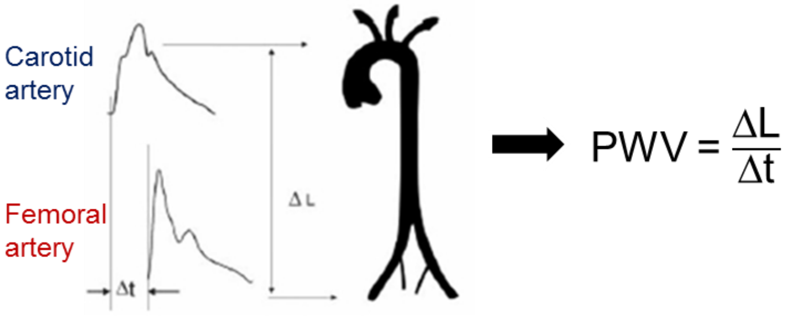

Figure 1.6: Implementation of the two-site method for PWV measurement using applanation tonometry entails measuring the travel time (Δt) and distance (ΔL) of the pressure waveform between two remote sites,

commonly the carotid and femoral arteries. Source: *Cardiac Imaging Group, University of Queensland, Australia*.

1.3.2 Imaging-based methods

In efforts to provide more localized measurements of PWV, a number of image-guided methods have been proposed. Rather than recording the waveform at two remote sites, these methods attempt to measure the PWV over a short arterial segment. The direct measurement of velocity requires at least two measurement sites. However, single-site methods employing mathematical models such as the Bramwell-Hill equation (Eqn. 1.2) have also been implemented.

Cardiovascular magnetic resonance imaging (cMRI) techniques typically involve tracking the blood flow over a segment of the artery using velocity-encoded gradients [82, 83]. While MRI offers unparalleled spatial resolution compared to other imaging modalities, one of its primary drawbacks for PWV measurement is low temporal resolution. Since the pulse wave is a fast propagating phenomenon, it is desirable to image the arterial segment at high frame rates with a high spatial resolution in order to obtain numerous spatial and temporal samples of the waveform. For vascular disease screening purposes, MRI is also not ideal due to its large size, long examination duration, and high cost. To this end, ultrasound imaging is a portable, fast, and low-cost solution that provides both superior frame rate and a high scan line density.

Early ultrasound imaging methods for PWV measurement consisted of measuring either flow velocity [84] or vessel diameter [48] at two arterial sites located close together using Doppler imaging or echo tracking, respectively. Such methods typically suffered from unexpected artifacts that turned out to be wave reflections, suggesting the need for a greater number of measurement sites (i.e. spatial resolution) along the same arterial segment in order to assess pulse wave dynamics in greater spatial detail. The use of multiple ultrasound scan lines in B-Mode [85] or tissue Doppler

[86] allowed for wall tracking at multiple positions along the arterial segment. However, B-Mode wall tracking lacks reproducibility while tissue Doppler suffers from angle-dependence. Ultrasound elasticity imaging, a relatively new research area in ultrasound and the focus of this dissertation, offers a promising means for PWV measurement based on speckle tracking of the radiofrequency signals reflected by the artery walls.

This dissertation is structured as follows. Chapter 2 provides an overview of ultrasound imaging, particularly ultrasound elasticity imaging, with emphasis on arterial applications. Pulse Wave Imaging (PWI), the core technique of this dissertation, is introduced as a novel ultrasonic imaging tool for the visualization and spatio-temporal mapping of the pulse wave-induced arterial wall motion, facilitating the guided measurement of the pulse wave velocity (PWV). Chapter 3 describes an *ex vivo* and *in vivo* performance assessment of the PWI method using different combinations of image acquisition and signal processing parameters. Chapter 4 presents the results of a feasibility study in the abdominal aortas of patients with hypertension and AAA. Chapter 5 introduces Pulse Wave Ultrasound Manometry (PWUM), an extension of the PWI method for pulse pressure measurement in large central arteries, and presents the results from a pilot study in the abdominal aortas of patients with pre-hypertension and hypertension. Chapter 6 describes the application of PWI in patients with carotid artery stenosis for the characterization of atherosclerotic plaques and ultimately stroke prediction. Finally, Chapter 7 summarizes the key findings from this dissertation and offers future directions for clinical implementation of the PWI method, including an unsupervised machine learning framework to correlate pulse wave features with disease states.

Chapter 2

Ultrasound Imaging and Its Use for Arterial Pulse Wave Assessment

2.1 Vascular Ultrasound

Ultrasound is advantageous for vascular applications because it does not use ionizing radiation and provides a clear picture of soft tissues that may not show up well on x-ray images. The high temporal resolution of ultrasound also allows for real-time imaging of moving structures such as the pulsating arteries. Vascular sonography is commonly used for monitoring blood flow and identifying abnormal regions (i.e. clots, plaque, emboli, aneurysm, etc.) in the circulatory system.

Diagnostic ultrasound imaging transducers are composed of an array of piezoelectric elements that produce a vibration when electrically excited, generating high-frequency acoustic waves (3-12 MHz for vascular applications) in short pulses that are transmitted into the tissue as mostly longitudinal compression waves. The interaction of these waves with the tissue gives rise to two distinct patterns of reflection that make up an ultrasound image – specular reflection, which occurs at distinct boundaries such as the artery walls, and scattering, which occurs at small boundaries relative to the wavelength of the ultrasound pulses. Specular reflection is responsible for the bright appearance of tissue interfaces, while scattering gives rise to the characteristic texture (i.e. speckle) of the image [87]. The transducer elements also act as receivers, converting the reflected echoes into electrical signals according to their intensity. The depth in the imaging field of view (FOV) from where the reflected echoes originated are calculated based on their time delays, assuming a constant speed of sound (typically 1540 m/s in soft tissue) [88]. An image of the internal body structure is formed by exciting the piezoelectric elements sequentially to generate multiple scan lines. Image formation will be discussed in greater detail in Section 2.1.2. A standard 2D B-Mode (brightness mode) image represents the grayscale intensity of the reflected echoes at their appropriate depths in the FOV. The duration (bandwidth) and center frequency of the electrical pulses used to excite the piezoelectric elements define the axial resolution (i.e. along the ultrasound scan line), while the aperture of the transducer defines the lateral resolution.

2.1.1 Diagnostic ultrasound imaging of the arteries

While B-Mode ultrasound is relied on clinically for the visualization and assessment of arterial structure, such as to locate a region of narrowing or measure the diameter of an aneurysm, Doppler mode ultrasound is used to visualize and quantify blood flow. Doppler techniques use the frequency shift caused by moving blood to derive the flow velocity based on the Doppler equation

$$v = c\left(\frac{\Delta f}{f_0}\right), \qquad [2.1]$$

where c is the speed of sound, f_0 is the frequency of the transmitted ultrasound pulse, and Δf is the frequency shift of the reflected echo.

The two primary types of flow imaging used in vascular sonography are pulsed-wave (PW) Doppler and color flow imaging (CFI). PW Doppler sends short ultrasound pulses to a user-specified depth in the image, called the “sample gate”. For arterial applications, the sample gate is placed in the lumen of the artery of interest. The phase shifts of the returning echoes are measured over time in order to obtain the Doppler frequency shift. In this way, PW Doppler generates a spectrum of the blood flow velocities at a specific location in the lumen of the artery. In CFI, PW

Doppler is performed at multiple sample gates covering an area of the image, and the velocity values are color-coded and superimposed onto the B-Mode image. This provides a spatial map of the blood flow within the entire lumen.

B-Mode and Doppler ultrasound can be combined into a single image in order to visualize artery structure and blood flow simultaneously. Triplex mode (Figure 2.1) refers to a combination of B-Mode, CFI, and PW Doppler in real-time.

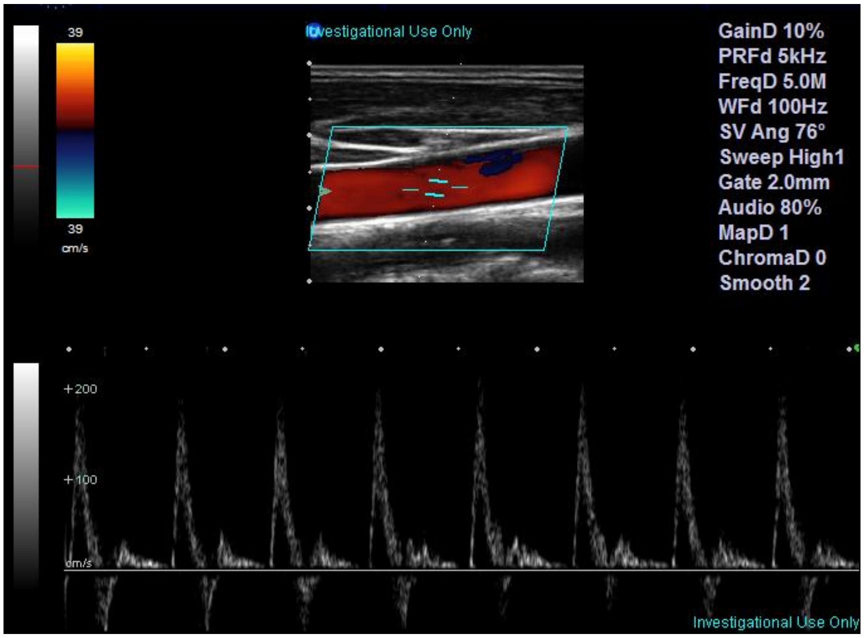

GainD 10%
PRFd 5kHz
FreqD 5.0M
WFd 100Hz
SV Ang 76°
Sweep High1
Gate 2.0mm
Audio 80%
MapD 1
ChromaD 0
Smooth 2

Figure 2.1: Triplex mode sonography combines B-Mode ultrasound with pulsed-wave (PW) Doppler and color flow imaging in order to image arterial structure and blood flow simultaneously. The light blue trapezoid in the image represents the CFI area, while the light blue lines in the lumen of the artery represents the sample gate at which the PW Doppler flow spectrum is measured.

2.1.2 Conventional vs. plane wave ultrasound architectures

Conventional

In conventional imaging sequences (Figure 2.2), image frames are acquired by sweeping a focused acoustic beam across the image plane and acquiring echoes sequentially. Each focused beam allows for the reconstruction of one scan line in the imaging plane. The frame rate is determined by the time required to transmit a beam, receive and process the backscattered echoes from the medium, and repeat the process for all scan lines of the image.

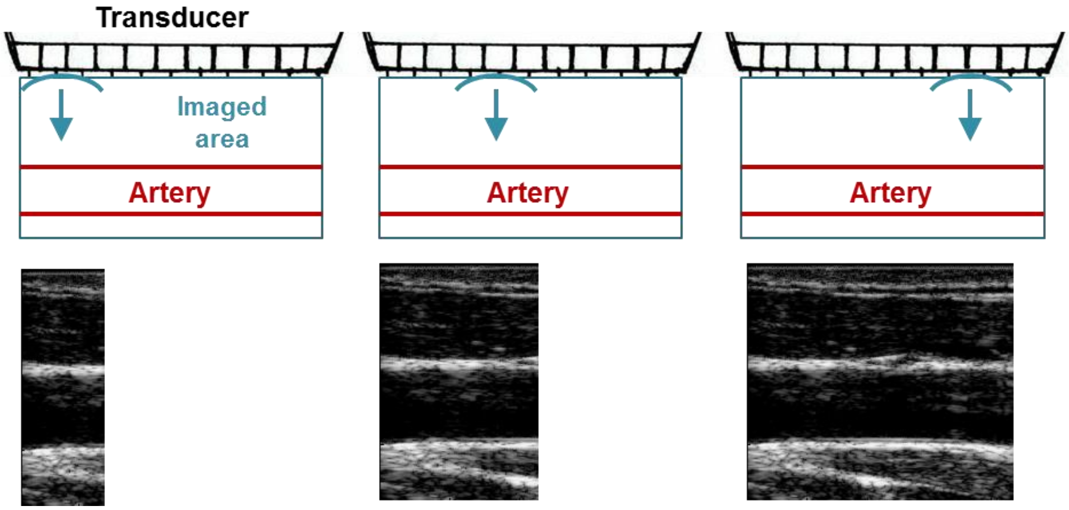

Figure 2.2: A conventional ultrasound imaging sequence involves sweeping a transmit-focused beam across the imaged area, reconstructing the image line by line. Typically, up to 256-512 scan lines are used to generate the full image, depending on the size of the transducer array.

Plane wave

When imaging very fast moving phenomena such as cardiac motion or arterial pulse wave propagation, conventional ultrasound frame rates may not detect important details such as wave reflections. The motivation behind plane wave ultrasound imaging was to enable novel and previously impossible methods for visualizing and analyzing phenomenon such as transient shear wave propagation [89] and 2D blood flow [90, 91]. Ultrafast frame rates (> 2000 frames/sec) are achieved by insonificating the entire imaging plane with a single plane wave transmission (Figure 2.3) instead of sweeping a focused beam line-by-line. Plane wave beamforming techniques such as the delay-and-sum method [92] then enable the reconstruction of individual scan lines.

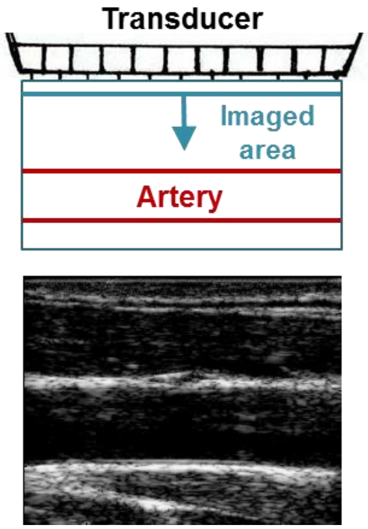

Figure 2.3: In the plane wave ultrasound architecture, all transducer elements are excited at once, sending a single plane wave into the tissue. The image is reconstructed using delay-and-sum beamforming techniques.

In this dissertation, data acquisition was performed using both conventional and plane wave imaging architectures on open-source ultrasound systems. Although imaging of the fast propagating arterial pulse wave can benefit from higher frame rates, plane wave imaging systems have not yet made their way into the clinic due to long image acquisition times and reduced image quality. New imaging methods that are implemented using conventional scanners have the potential for immediate clinical translation. The conventional systems used are the SonixTouch and the SonixRP (Analogic Corp., Peabody, MA, USA), two diagnostic scanners packaged with an Ultrasound Research Interface that allows for the acquisition and storage of radio-frequency (RF) data. The plane wave systems used are the Verasonics V-1 and Vantage (Verasonics, Inc., Seattle, WA, USA). These machines are highly flexible research systems that provide control over plane wave transmission sequences and access to the raw signals from each individual transducer element.

2.2 Ultrasound Elasticity Imaging

Elasticity imaging is a relatively new medical imaging modality that reveals the elastic properties of soft tissue by measuring the tissue deformation in response to a mechanical force [93]. Its goal is to noninvasively detect and map the relative stiffness (e.g. Young's modulus) of tissue within the body, providing additional and clinically relevant information that may not be apparent from traditional imaging exams. The most prominent techniques use magnetic resonance (MR) or ultrasound to generate both a stiffness map and an anatomical image for comparison [94]. All elasticity imaging techniques rely on the same basis – an external force is applied to the tissue of interest and the resulting deformation is observed and quantified.

Ultrasound elasticity imaging methods can be classified according to the source of excitation used to deform the tissue. The first ultrasound-based elasticity imaging methods employed an external force, such as a transducer, to compress the skin as in elastography or strain imaging [95]. In sonoelasticity, a mechanical vibrator can be used to vibrate the tissue at specific frequencies [96]. Some methods also take advantage of natural physiological motion such as breathing, cardiac contraction, and arterial pulsation [97-101]. Newer methods include acoustic radiation force impulse (ARFI) imaging [102] and shear wave elastography (SWE) [103, 104], which rely on an acoustic excitation "push" to induce localized displacements in the tissue of interest.

The pulsation of the arteries exerts a mechanical force that deforms the walls by causing the artery to distend. This eliminates the need to apply an external force, and ultrasound elasticity image processing techniques can be applied to quantify the natural pulsation of the arteries. Quantification of the arterial wall motion presents a wealth of information that can be used to evaluate phenomenon such as arterial distensibility and pulse wave propagation, as well as derive mechanical parameters such as compliance and Young's modulus [105, 106].

2.2.1 Speckle tracking

The measurement of tissue deformation in ultrasound elasticity imaging is generally achieved by tracking the movement of the speckle pattern in between frames. This can be done in 1D using time-shift cross-correlation techniques among segments of ultrasound A-lines [95], or in 2D using block-matching techniques [107]. Over the past two decades, different approaches based on B-Mode [108] or RF speckle tracking [109-111] or phase-tracking techniques [112] have been proposed. Two-dimensional speckle-tracking-based motion estimation techniques have also been implemented in clinical systems.

Due to the scattering that occurs within the artery walls, speckle tracking can be used to quantify the wall motion. An illustration of speckle tracking for arterial wall tracking is shown in Figure 2.4. In frame k, a window for each wall is defined as the *reference window*. In the next frame, a search range for each wall is defined as the *comparison window*. The normalized cross-correlation (NCC) function between the reference and comparison windows is defined as

$$R_{NCC}(u,\tau) = \frac{\sum_{n=u}^{u+W-1} f(n) g(n+\tau)}{\sqrt{\sum_{n=u}^{u+W-1} f^2(n) \cdot \sum_{n=u}^{u+W-1} g^2(n+\tau)}}, \qquad [2.2]$$

where u is the origin of the reference window, W is the size of the reference window, and τ is the shift between the reference and comparison windows. In other words, the standard cross-correlation between the two windows (numerator) is normalized by the square root of the product of their energies (denominator) in order to obtain the NCC as a function of time shift. The time shift corresponding to the peak of the NCC function represents the most likely new position of the wall in frame $k+1$. This time shift can then be converted to the wall displacement based on the speed of sound and the ultrasound system's sampling frequency. By tracking the 1D wall displacement in the axial direction (i.e. parallel to ultrasound beam) at all scan lines in between each frame, the dilation of the artery can be captured over time.

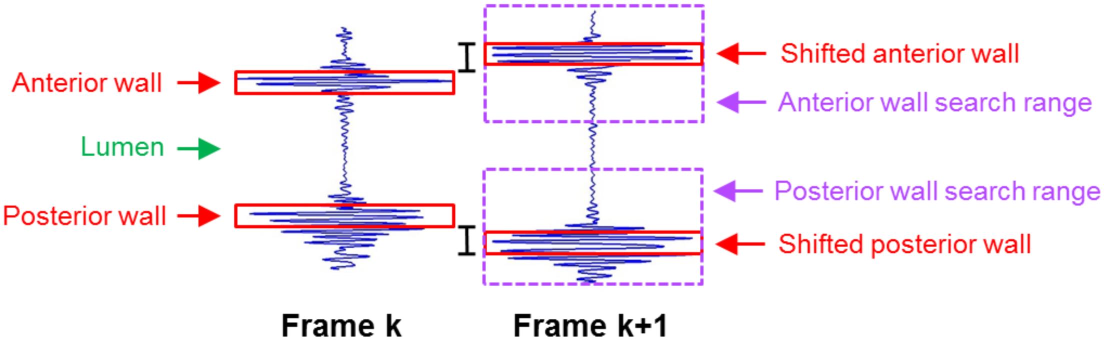

Figure 2.4: Speckle tracking for arterial wall motion estimation on one ultrasound scan line. The displacement (i.e. shift) of the vessel walls can be quantified by locating the peak of the normalized cross-correlation function between a reference window (red rectangle) within the wall in a given frame and a larger comparison window (purple dashed rectangle) containing the wall in the next frame.

2.2.2 Arterial applications of ultrasound elasticity imaging

The clinical use of ultrasound elasticity imaging techniques is an expanding field that includes applications such as lesion detection and classification, liver fibrosis staging, ablation treatment monitoring, assessment of musculoskeletal mechanical properties, and vascular imaging [113]. Speckle tracking has been applied on ultrasound signals from major arteries such as the abdominal aorta, carotid artery, and brachial artery for the measurement of parameters such as distension, compliance, and strain [114-116]. Intravascular ultrasound (IVUS) elastography uses the RF signals from an ultrasound catheter to quantify the deformation of the wall by estimating strains from within vessels such the coronary and femoral arteries [101]. ARFI imaging has also been used for plaque characterization in the carotid artery based on the distribution of acoustic radiation force-induced displacements within plaque regions [117], and will be further discussed in Chapter 6.

2.3 Pulse Wave Imaging (PWI)

The application of RF speckle-tracking principles to quantify the motion of the naturally pulsating artery walls has led to the development of Pulse Wave Imaging (PWI) by our lab [118-125]. PWI serves as a noninvasive technique to visualize and map the estimated pulse wave-induced arterial wall displacement waveforms over localized segments, allowing for direct imaged-guided measurement of clinically relevant parameters such as PWV, pulse wave propagation uniformity, and distension.

2.3.1 PWI methodology and advantages

A block diagram describing the PWI method in a normal human aorta is shown in Figure 2.5. Since the frame rate may vary depending on the imaging depth and number of ultrasound scan lines used, it is important to normalize the inter-frame arterial wall displacements by the frame rate. Data acquired at low frame rates will exhibit higher displacements due to the increased time in between each frame. Normalization is performed by multiplying the displacement values by the frame rate, which is equivalent to dividing by the time in between each frame to arrive at inter-frame velocities in units of mm/s.

In the abdominal aorta, the posterior wall exhibits very little motion due to its close proximity to the spine [126], while the pulse wave propagation is apparent in the anterior wall (2.5b). Thus, the anterior wall displacements are typically used for spatio-temporal mapping of the pulse wave (2.5d). The PWV is estimated as the slope of the linear regression line fitted to the spatio-temporal variation of a particular waveform tracking feature (e.g. the 50% upstroke), which also allows the pulse wave propagation uniformity to be assessed as the coefficient of determination r^2. A high r^2 indicates the presence of a dominant PWV equal to the slope of the regression line, suggesting relatively uniform stiffness across the segment. A low r^2 implies that the PWV may be changing throughout the imaged segment due to non-uniform arterial mechanical properties and/or wave reflections.

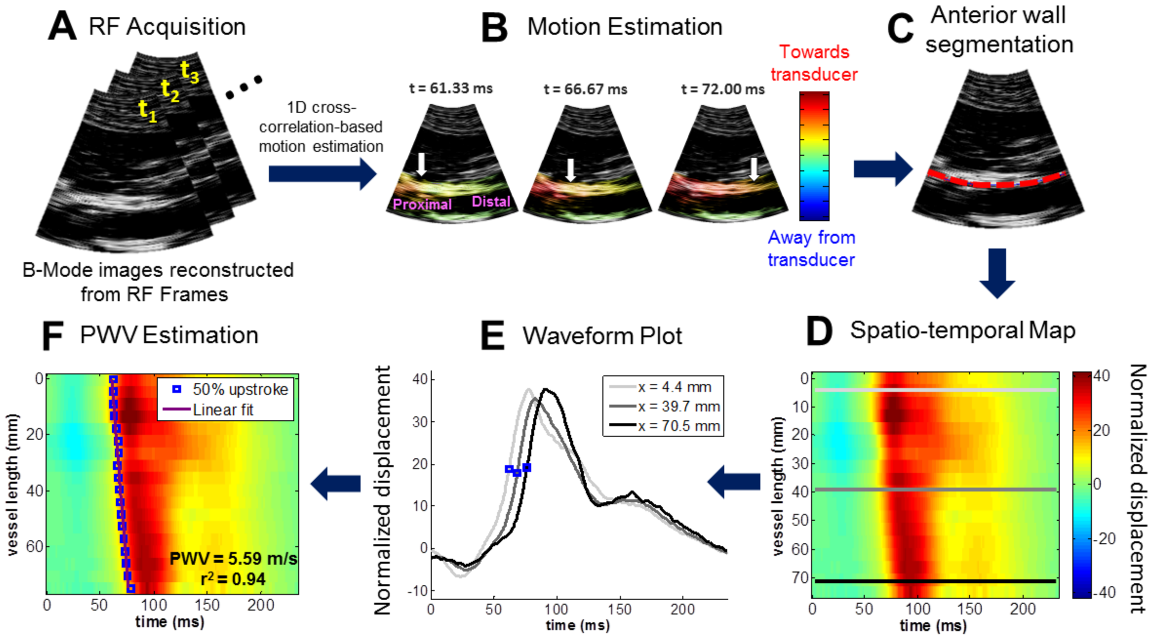

A RF Acquisition
t1
t2
t3
B-Mode images reconstructed from RF Frames
1D cross-correlation-based motion estimation
B Motion Estimation
t = 61.33 ms
t = 66.67 ms
t = 72.00 ms
Proximal
Distal
Towards transducer
Away from transducer
C Anterior wall segmentation
D Spatio-temporal Map
vessel length (mm)
time (ms)
Normalized displacement
E Waveform Plot
x = 4.4 mm
x = 39.7 mm
x = 70.5 mm
Normalized displacement
time (ms)
F PWV Estimation
50% upstroke
Linear fit
PWV = 5.59 m/s
r² = 0.94
vessel length (mm)
time (ms)

Figure 2.5: Block diagram of the Pulse Wave Imaging (PWI) method on a normal human aorta *in vivo*. *(A)* A sequence of RF frames is acquired at the minimum depth required to visualize both walls of the artery of interest. *(B)* A 1D normalized cross-correlation-based motion estimation method (Luo and Konofagou 2010) is used on the RF signals to compute the inter-frame axial (i.e. parallel to the ultrasound beams) displacements in the arterial walls. The displacement amplitudes are normalized by multiplying by the frame rate. The arrival of the pulse wave induces positive (i.e. towards the transducer) displacements in the anterior wall and negative (i.e. away from the transducer) displacements in the posterior wall. The white arrows indicate the propagation of the wavefront along the anterior wall. *(C)* The anterior wall is manually segmented (red dotted line) in the first frame of the acquisition sequence, and this trace is automatically updated in subsequent frames based on the estimated displacements. *(D)* The anterior wall motion is spatio-temporally mapped over one cardiac cycle by plotting the displacements in the wall trace over time. *(E)* The normalized displacement waveform at three scan line positions along the anterior wall, corresponding to the light gray, dark gray, and black lines in *(D)*, are shown. The time point corresponding to a characteristic tracking feature (e.g. the 50% upstroke as indicated by the blue dots) is automatically detected in the waveform at each position. *(F)* Linear regression is performed on the spatio-temporal variation of the characteristic time points along the imaged segment to obtain the slope as the PWV and the coefficient of determination r^2 as an index of propagation uniformity.

Due to its ability to dynamically visualize and map the pulse wave with high spatial and temporal resolution, PWI has the potential to detect and characterize arterial disease based on the regional PWV and r^2. PWI presents several advantages over other methods of assessing the arterial pulse wave that contribute to its clinical utility:

1) **High spatial and temporal resolution**: Multiple waveforms (i.e. equal to the number of ultrasound scan lines used) can be acquired along an imaged segment over the same cardiac cycle at high frame rates (up to ~500 FPS using conventional ultrasound *in vivo*), providing numerous spatial and temporal samples for mapping the pulse wave propagation.
2) **Direct measurements**. Unlike alternative techniques [127, 128], PWI does not require a generalized transfer function to provide imaged-guided measurements of the abdominal aorta, which is a deep vessel that is inaccessible by superficial force tonometers.
3) **Localized**. Rather than performing measurements over the entire circulation [80, 129], PWI captures the wall dynamics of an imaged arterial segment, allowing for localized assessment.

4) **Low cost**. PWI is based on ultrasound technology, which is relatively inexpensive and highly suitable for screening and dynamic testing purposes.

5) **Highly translational**. The only required equipment to perform PWI is a clinical ultrasound scanner.

2.3.2 History of PWI

Early PWI studies in $CaCl_2$ and AngII-induced abdominal aortic aneurysm (AAA) mouse models [119, 122] revealed that the uniformity of the pulse wave propagation may serve as a valuable biomarker to differentiate between normal and diseased arteries. Mouse studies involving PWI are also geared towards the staging and monitoring of AAA and atherosclerosis over time based on changes in the PWV and propagation uniformity within and around the aneurysmal region [125]. In general, the PWV was not significantly between normal and aneurysmal mouse aortas, but the r^2 was significantly lower, suggesting that the wave propagation uniformity may be a viable biomarker for AAA staging and characterization.

The *in vivo* feasibility of PWI has also been demonstrated in the carotid arteries and abdominal aortas of healthy human subjects [121, 130], yielding average PWV values of 4.4 ± 0.6 m/s and 4.0-5.2 m/s, respectively. Comparison of the PWV measurements obtained using PWI with those obtained using carotid-femoral applanation tonometry yielded an average bias of 0.25 m/s [124].

Chapter 3

Performance assessment and optimization of the PWI method

3.1 Introduction

Variance and inconsistency of the PWV and r^2 measurements obtained by PWI may arise due to several imaging and signal processing parameters. In order for PWI to be considered as a reliable measurement tool, the effects of these parameters must be assessed in order to improve the precision and accuracy of the measurements.

3.1.1 Considerations for performance assessment and optimization

Since PWI is based on sampling the pulse wave and tracking its propagation in both space and time, the PWV and r^2 measurements are contingent upon the tradeoff between spatial resolution (i.e. the number of scan lines) and temporal resolution (i.e. the frame rate), which are interdependent, i.e., decreasing the number of scan lines will increase the frame rate, and vice versa. For a given scan line density and PWV, a frame rate below the Nyquist rate may result in aliasing. That is, the pulse wave may appear to arrive at multiple scan line positions simultaneously, resulting in imprecise PWV measurements and low r^2. The frame rate also determines the fundamental upper limit on the PWV that can be reliably measured with PWI. Since we do not know the exact speed of the pulse wave prior to imaging, the tradeoff between scan line density and frame rate must be evaluated experimentally.

Signal processing parameters may have additional effects on the PWV and r^2 measurements. The waveform at each scan line position may be temporally up-sampled to artificially increase the frame rate, which may result in more precise PWV and r^2 measurements. Tracking different characteristic features of the waveform has also been shown to have an impact on the precision of the local PWV measurement [80, 131].

A conventional ultrasound scanner acquires image frames by sweeping a focused acoustic beam across the image plane and acquiring echoes sequentially. Beam sweeping induces delays in the acquisition of each RF scan line (and hence the motion estimation) as the pulse wave is propagating along the imaged segment, necessitating time delay compensation to obtain the true pulse wave arrival time at each spatial position [85, 118]. By contrast, plane wave imaging has been proposed to achieve ultrafast frame rates [89, 132-136]. The use of plane wave transmissions rather than line-by-line focused beam transmissions eliminates the beam sweep compensation and transducer orientation considerations of conventional ultrasound. However, the clinical applicability of plane wave technology is limited by slower processing speed, lower quality B-mode, and reduced portability. Implementation of PWI in conventional scanners would make the method universal to all scanners, promoting the highly translational nature of the method and allowing for a wide range of large-scale clinical studies using PWI.

3.1.2 Theoretical framework for the tradeoff between spatial and temporal resolution

The upper limit of the PWV measured by PWI is dependent on the frame rate *FR*, the scan line quantity *K*, and the imaged segment length *L*. By considering the spatiotemporal propagation of the pulse wave across *L*, we can derive the following expression for the maximum measurable PWV:

$$PWV_{max} = \frac{L*K*FR}{(K*2)-(K-1)} = \frac{L*K*FR}{3K-1} = \frac{K}{K+1}(L*FR) \qquad [3.1]$$

A full derivation of Eq. 3.1 is presented in the Appendix. Any PWV measurement that exceeds the upper limit established by Eq. 3.1 may likely have arisen from aliasing due to insufficient frame rate and may be deemed invalid.

3.2 Parametric Study Design

The objective of this parametric study was to establish a theoretical and experimental framework for assessing the performance of PWI under various image acquisition parameters (number of scan lines and frame rate) and signal processing parameters (temporal upsampling factor and waveform tracking feature). The framework was implemented in canine aortas *ex vivo* and human carotid arteries and aortas *in vivo* to determine the optimal PWI parameters based on the precision of the PWV measurement and the magnitude of the r^2 value.

3.2.1 *Ex vivo* experiments

Benchtop *ex vivo* experiments were performed in order to provide a controlled environment in which the image acquisition parameters could be varied while maintaining the exact same field of view. N = 2 freshly excised canine aortas (Figure 3.1) were mounted separately in a water tank of phosphate-buffered saline (PBS) using plastic fittings on either side (Figure 3.2). The tension applied on the canine aorta specimens served to minimize the rigid motion in the *ex vivo* setup. A peristaltic pump (Manostat Varistaltic, Barrington, IL) operating at 2 Hz was used to generate pulsatile flow through each specimen. Ultrasound RF signals were acquired using a 10-MHz linear array transducer (SonixTouch, Ultrasonix Medical Corp., Burnaby, Canada) within a constant 25 mm (depth) x 38 mm (width) field of view while varying the number of scan lines.

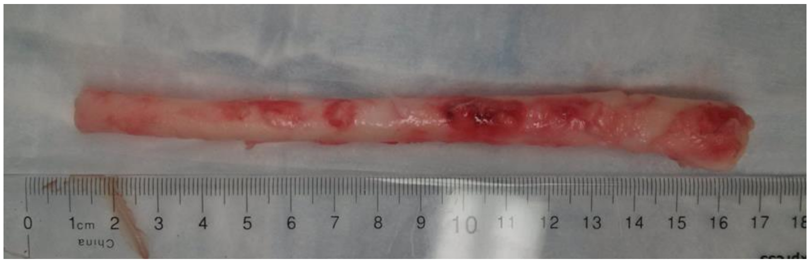
0
1cm
2
3
4
5
6
7
8
9
10
11
12
13
14
15
16
17

Figure 3.1: Freshly excised canine aortas were used for the *ex vivo* experiments.

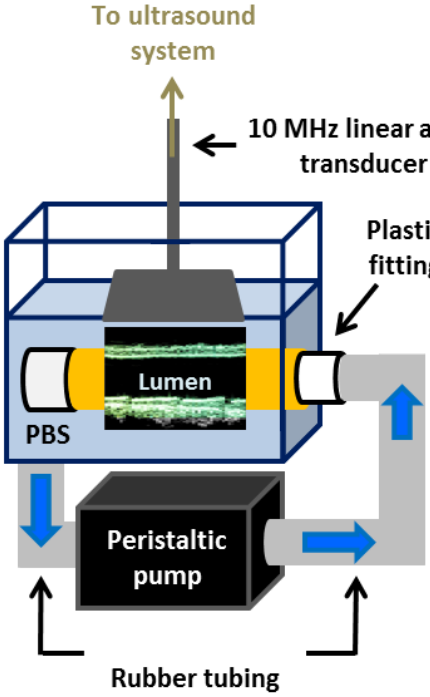
To ultrasound system
10 MHz linear array transducer
Plastic fitting
Lumen
PBS
Peristaltic pump
Rubber tubing

Figure 3.2: Schematic of the setup used for *ex vivo* experiments. The canine aorta was held in place within a PBS-filled tank using plastic fittings. The peristaltic pump circulated pulsatile flow from the tank through the specimen and back into the tank.

The upper limits of the PWV estimation for the different scan line quantities (K) studied in this paper are listed in Table 3.1 along with their corresponding frame rates. Since the linear transducer was oriented parallel to the canine aorta for the *ex vivo* portion of this study, the imaged segment length *L* is fixed and equal to the width of the transducer. In practice, when scanning human subjects, *L* may vary depending on the angle between the transducer and the artery. This paper focused on the tradeoff between spatial and temporal resolution with other parameters such as focal configuration and imaging depth kept constant.

L (mm)	K	FR (fps)	PWV_{max} (m/s)
38	128	160	6.03
38	96	214	8.05
38	64	321	12.01
38	48	428	15.93
38	32	642	23.66
38	24	856	31.23
38	16	1248	44.63

Table 3.1: Scan line quantities (*K*) used along with their corresponding frame rates (*FR*) and PWV upper limits (PWV_{max}) as determined by Eqn. 3.1. The imaged segment length (*L*) is fixed under the assumption that the 38-mm wide linear array transducer is orientated exactly parallel to the specimen.

Following data acquisition, the inter-frame axial wall displacements were computed offline using a 1D cross correlation-based motion estimation method [137] on the RF signals with a 3.5-mm window size and 95% overlap. Manual segmentation of the upper wall (Figure 2.5c) in the first frame of the acquisition sequence generated a wall trace that specified the depth of the wall at each scan line. The displacements at each point along the trace were used for spatio-temporal mapping of the wall motion. The normalized displacement waveform (i.e. multiplied by the frame rate) at each scan line position was temporally upsampled by factors of 1, 2, 4, 8, 16, 32, and 64 using 1D linear interpolation (table lookup) in MATLAB (Mathworks Inc., Natick, MA, USA).

For each combination of scan line quantity and upsampling factor, the PWV and r^2 were measured over 10 pump cycles using linear regression on the spatio-temporal variation of the 50% upstroke. The methods for calculating the 50% upstroke and other waveform tracking features will be discussed in Section 3.2.2. Prior to linear regression, beam sweep compensation as described in the Appendix was applied at each scan line position.

PWV precision and r^2 magnitude for PWI optimization

The precision of the PWV measurements was defined as the SNR in dB, i.e. the logarithm of the ratio of the mean and standard deviation (μ/σ) over 10 pulse cycles. The greater the SNR, the more precise the measurement. Thus, performance assessment of PWI entails finding the combination of scan line quantity and temporal upsampling factor that yields the highest SNR.

The r^2 value is an approximate measure of the pulse wave propagation uniformity. A low r^2 may result from varying PWV within the imaged segment due to inhomogeneous vascular mechanical properties, but may also be caused by a low number of spatial and temporal samples, which would result in a false r^2 value. Hence, performance assessment of PWI also entails identifying the combination of scan line quantity and temporal upsampling factor that yields the highest r^2 values.

3.2.2 *In vivo* study

PWI was performed on the left common carotid arteries and infrarenal abdominal aortas (Figure 3.3) of ten normal human subjects (8 M, 2 F, mean age 24.8 ± 3.3 y.o.) in the supine position using the same 10 MHz linear array transducer (SonixTouch, Ultrasonix Medical, Burnaby, BC, Canada) for the carotid and a 3.3 MHz curvilinear array transducer for the aorta. To minimize rigid motion, each subject was requested to perform breath-holding for the entire duration of the 2.5-second RF acquisition. 5-8 acquisitions were performed on each artery in all subjects in order to average the PWV and r^2 measurements over multiple cardiac cycles.

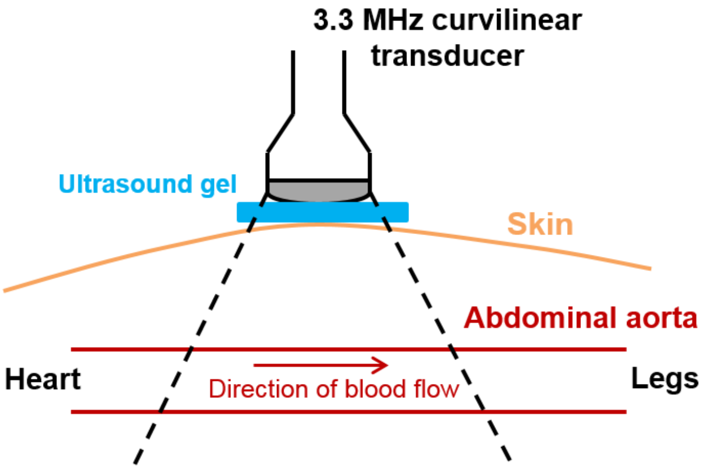

Figure 3.3: Schematic for *in vivo* data acquisition in the abdominal aorta. In order to minimize rigid motion, each subject was asked for perform breath-holding during each 2.5-second acquisition.

PWI in young, healthy subjects typically measures PWVs of 2-6 m/s in the carotid artery [118] and 4-8 m/s in the abdominal aorta [120, 121]. Several other studies using image-guided methods to measure local PWV in normal subjects have reported values within the same range [138-142], while the global PWV measured using carotid-femoral applanation tonometry in young healthy adults typically ranges from 5-7 m/s [143-148]. For the *in vivo* portion of this study, the carotid arteries were imaged at depths of 25-30 mm using the same transducer as that in the *ex vivo* experiments. From Table 3.1, it was determined that 32 scan lines would be used to achieve a PWV upper limit that is almost four times higher than the typical values found in literature. The aortas were imaged at depths of 70-90 mm and segment lengths of 80-100 mm. Based on these conditions and Eqn. 3.1, it was determined that 24 scan lines would be used to achieve frame rates of 309-347 fps and PWV upper limits of 23.19 – 33.31 m/s, also four times higher than typical values.

For consistency, the temporal upsampling factor was fixed at 10. Over each cardiac cycle, the absolute maximum of the normalized displacement waveform at each scan line position was automatically detected as the peak. From this point, the waveform was traversed backwards in time until the zero-crossing point was reached. The upstrokes were located as the points when the waveform reached 25% and 50% of the peak magnitude. The maximum first and second derivatives were detected by locating the peak of the first and second gradients of the normalized displacement waveform, respectively. A summary of the tracking features studied is shown in Figure 3.4 on representative waveforms from one subject's carotid artery. The SNR of the PWV measurement and magnitude of the r^2 value obtained by tracking different features of the waveform (i.e. zero-crossing, peak, 25% and 50% upstrokes, and maximum first and second derivatives) were assessed.

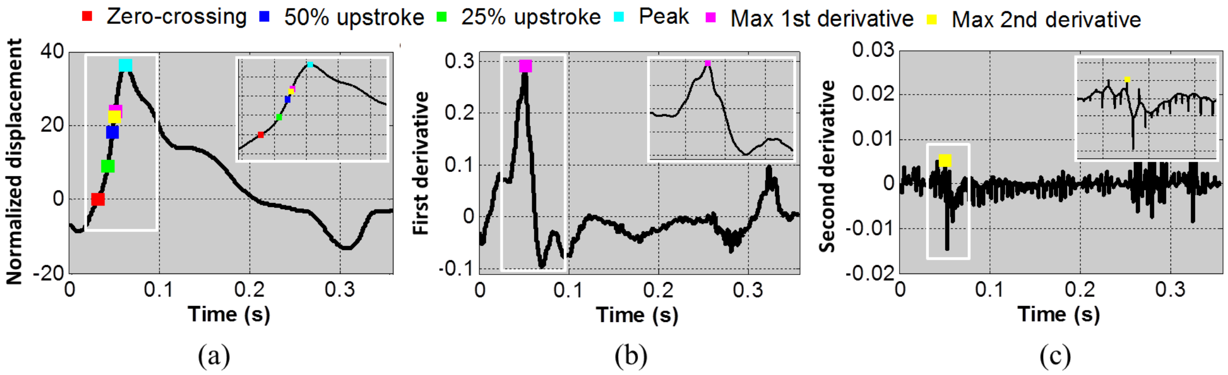

Figure 3.4: A representative (a) normalized displacement waveform from the carotid artery of a normal (M, 26) subject is shown along with the corresponding (b) first and (c) second derivative curves. The six waveform features investigated in this study (zero-crossing, 25% upstroke, 50% upstroke, peak, maximum first derivative, and maximum second derivative) are indicated on the curves as color-coded markers.

3.3 Results

3.3.1 *Ex vivo* results

Figure 3.5 shows the propagation of the pulse wave along the anterior wall of the first *ex vivo* canine aorta. The data was acquired using 48 scan lines, corresponding to a frame rate of 428 FPS (Table 3.1).

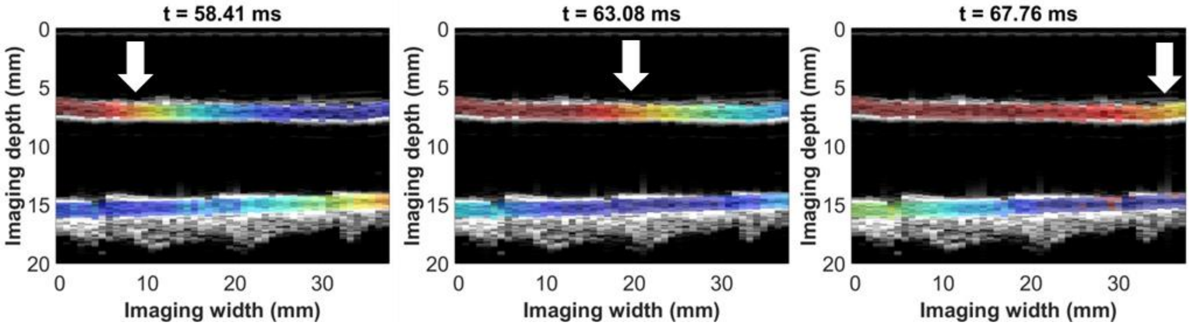

Figure 3.5: Consecutive PWI frames showing the propagation of the pump-induced pulse wave from left to right. The white arrows indicate the approximate position of the 50% upstroke in each frame.

Figure 3.6 illustrates the effect of temporal upsampling on the spatio-temporal map from data acquired using 128 scan lines (160 FPS). Without upsampling (3.6a), the PWV = 3.66 m/s and the r^2 was relatively low (0.69). When the waveform at each scan line position was upsampled by a factor of 2 (3.6b), the PWV value remained similar (3.29 m/s) while the r^2 increased dramatically (0.93). An upsampling factor of 8 (3.6c) further increased the r^2 to 0.99. This demonstrates that a falsely low r^2 may result from insufficient frame rate, thus necessitating the need to optimize the spatial and temporal resolution of PWI by saturating the r^2 magnitude.

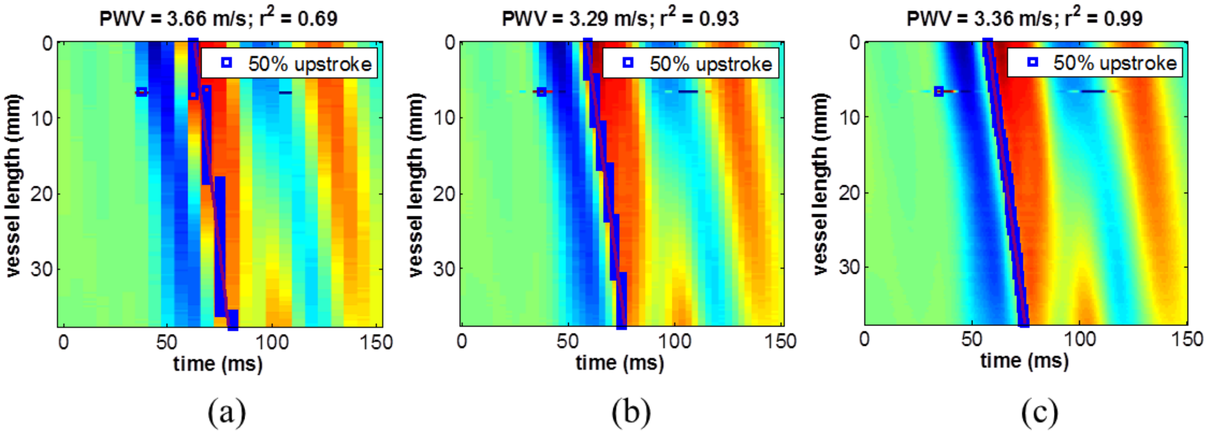

(a) (b) (c)

Figure 3.6: Effect of temporal upsampling on a spatio-temporal map of ex vivo data acquired using 128 scan lines (160 FPS). (A) Without upsampling, the r^2 is relatively low due to fewer discrete time samples. (B) With an upsampling factor of 2, the PWV value remains similar, however the r^2 increases dramatically. (C) An upsampling factor of 8 further increases the r^2. This demonstrates that a falsely low r^2 may result from insufficient frame rate, and may be improved by temporal upsampling.

Figure 3.7 shows (a) the mean PWV value, (b) SNR of the PWV measurement (SNR_{PWV}) in dB, and (c) the mean r^2 magnitude, all averaged over 10 pump cycles, for each combination of scan line quantity and temporal upsampling factor in the first of the two *ex vivo* canine aortas. The PWV averaged over all combinations was 3.33 ± 0.17 m/s, representing a standard error of only 2.4%. Figure 3.8 shows the same results for the second specimen, which exhibited an overall average PWV of 2.48 ± 0.12 m/s (standard error 1.7%). Both overall values were within the lowest upper limit on the PWV, which was 6.03 m/s for that of 128 scan lines and 160 FPS. The variation in the mean PWV obtained with different scan line quantities was deemed insignificant.

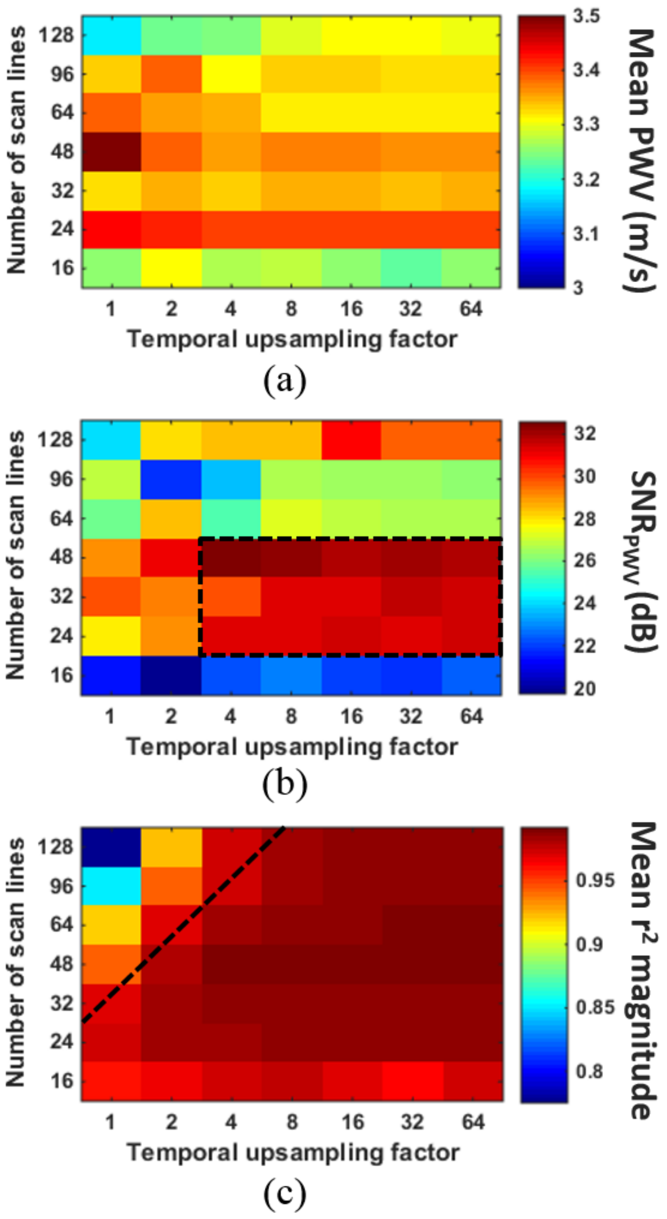

Figure 3.7: (a) Mean PWV, (b) SNR of the PWV measurement, and (c) magnitude of the r^2 value for each combination of scan line quantity and temporal upsampling factor in the first canine aorta. The value in each element of the matrices was obtained from PWV and r^2 measurements over 10 pulse cycles. The black dashed box in (b) indicates the combinations of scan line quantity and temporal upsampling factor that yielded the highest SNR$_{PWV}$, while combinations below the black line in (c) resulted in saturation of the r^2 magnitudes.

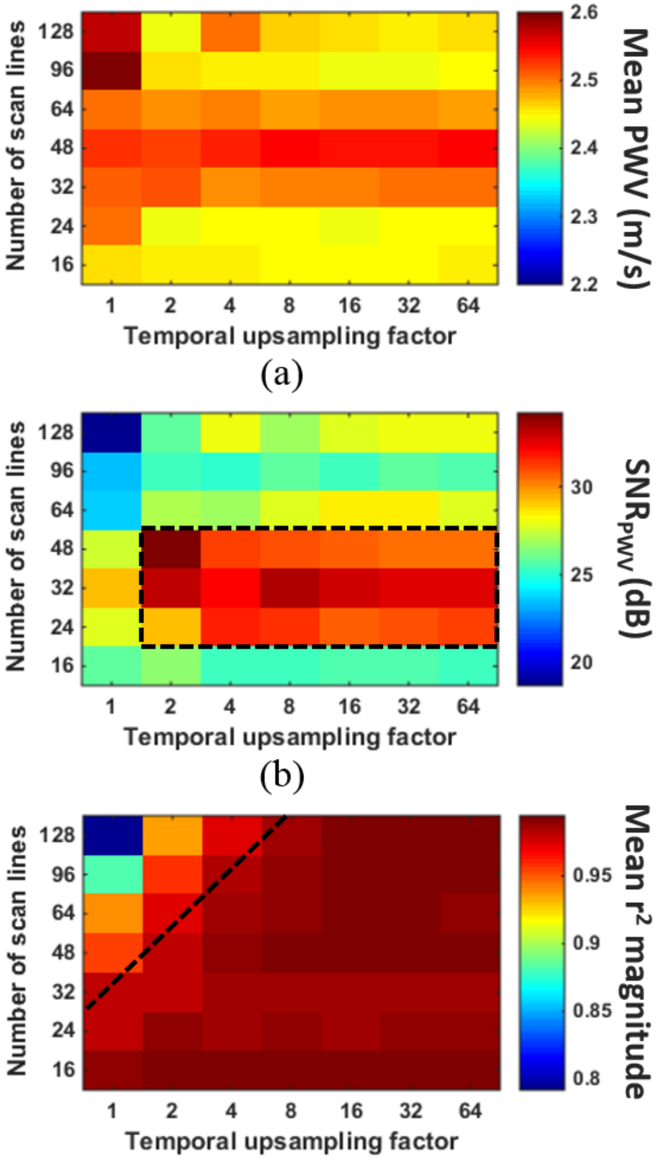

(a)

(b)

(c)

Figure 3.8: (a) Mean PWV, (b) SNR of the PWV measurement, and (c) magnitude of the r^2 value for each combination of scan line quantity and temporal upsampling factor in the second canine aorta. The value in each element of the matrices was obtained from PWV and r^2 measurements over 10 pulse cycles. The black dashed box in (b) indicates the combinations of scan line quantity and temporal upsampling factor that yielded the highest SNR$_{PWV}$, while combinations below the black line in (c) resulted in saturation of the r^2 magnitudes.

In both specimens, the mean PWV for a particular scan line quantity remained relatively consistent over all upsampling factors. That is, the mean PWV did not seem to be affected by the temporal upsampling factor. The only exception was in the case of 128 scan lines in the first specimen (3.7a), where the PWV appears to increase as the temporal upsampling factor is increased. Also in both specimens, scan line quantities of 24, 32 and 48 consistently yielded the highest SNR_{PWV} for upsampling factors greater than 4, as indicated by the black dashed square in Figures 3.7b and 3.8b. Given the fixed 38 mm imaging plane width, this translated to scan line densities of 0.63-1.26 lines/mm, respectively.

The black dashed line in Figures 3.7c and 3.8c indicates the cutoff at which the r^2 values become relatively saturated. In both specimens, r^2 saturation occurs below the same cutoff line. This suggests that the greater the number of scan lines used, the greater the temporal upsampling factor must be in order to achieve r^2 saturation.

3.3.2 *In vivo* results

Figure 3.9 shows the SNR_{PWV} (a) and r^2 magnitude (b) in the carotid artery and aorta averaged over all 10 normal subjects for each waveform tracking feature. The Bonferri multiple comparisons test was used to identify features that measured significantly SNR_{PWV} and r^2 magnitude for aortas and carotids separately. In the carotid arteries, the 50% upstroke and maximum first derivative yielded significantly higher ($p < 0.05$) SNR_{PWV} compared to the other tracking features, and the 25% and 50% upstrokes yielded significantly higher r^2. In the aortas, the 25% and 50% upstrokes yielded significantly higher SNR_{PWV} and r^2. While the maximum first derivative also yielded significantly higher r^2,' its SNR_{PWV} was significantly lower than those obtained by the 25% and 50% upstrokes.

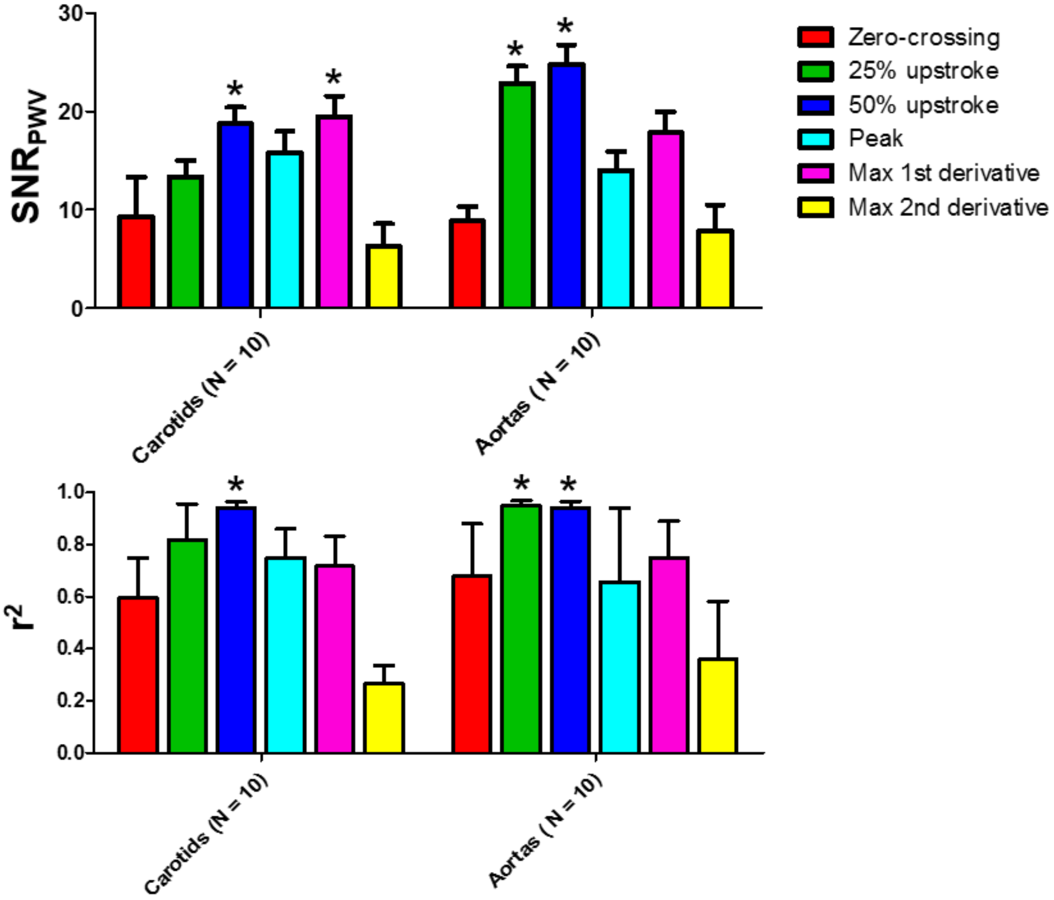

Figure 3.9: (a) SNR of the PWV measurement and (b) magnitude of the r^2 value averaged over N = 10 human carotid arteries and N = 10 human aortas *in vivo* from tracking each of the six waveform features indicated (i.e. zero-crossing, 25% upstroke, 50% upstroke, peak, maximum first derivative, and maximum second derivative). The SNR_{PWV} and mean r^2 for each tracking feature were obtained from PWV and r^2 measurements over at least 10 cardiac cycles per subject. * denotes a tracking feature that yielded significantly higher SNR_{PWV} and r^2 when compared to other tracking features using the Bonferri multiple comparisons test.

It is important to note that tracking different waveform features resulted in different mean PWVs when averaged over all 10 subjects. In the carotid arteries, the 25% upstroke, 50% upstroke, peak, and maximum first derivative yielded very similar PWVs of 4.61 ± 1.51 m/s, 4.76 ± 1.33

m/s, 4.83 ± 1.25 m/s, 4.25 ± 1.05 m/s, respectively. These four features also exhibited the highest SNR_{PWV} and r^2. The mean PWVs obtained from the zero-crossing and maximum second derivative were 5.74 ± 3.20 m/s and 3.05 ± 1.98 m/s, respectively. In the aortas, the mean PWVs averaged across all 10 subjects were 8.03 ± 4.15 m/s for the zero-crossing, 5.77 ± 1.35 m/s for the 25% upstroke, 5.62 ± 1.24 m/s for the 50% upstroke, 7.70 ± 4.65 m/s for the peak, 5.43 ± 1.78 m/s for the maximum first derivative, and 6.72 ± 5.47 m/s for the maximum second derivative. Once again, the PWV values that were most similar to each other (25% and 50% upstroke and maximum first derivative) corresponded to the tracking features that exhibited the highest SNR_{PWV} and r^2.

3.4 Discussion and Conclusions

By mapping the pulse wave at numerous spatial positions and high frame rates over a single cardiac cycle, PWI may provide new avenues for pulse wave analysis and local PWV estimation in any major artery accessible by ultrasound. This parametric study was aimed at establishing a performance assessment framework to improve the clinical reliability of PWI for *in vivo* measurements. Since accuracy cannot be measured *in vivo* because the value of the ground truth PWV is unknown in a clinical setting, we must rely on the repeatability (PWV precision) and uniformity (r^2 magnitude) to assess the reliability of the measurements.

The precision of the PWV measurement (i.e. SNR_{PWV}) in both *ex vivo* canine aortas was highest with 24, 32 and 48 scan lines rather than 128 or 16, the maximum and minimum number of lines investigated in this study, respectively. This phenomenon demonstrates the balance between spatial and temporal resolution – sacrificing the frame rate to increase the number of scan lines, or vice versa, may result in a lower SNR_{PWV}. The relatively low SNR_{PWV} at high scan line densities (64, 96, and 128) may be explained by the lower frame rates. Due to fewer temporal samples, the waveform at each spatial position along the vessel lacks detail and appears less smooth, resulting in greater variation of the 50% upstroke positions detected by the waveform feature tracking algorithm used in this study. Low frame rate data provides a limited number of points along each waveform with which to perform temporal upsampling, which may also result in greater feature tracking variability. In the cases of 24, 32, and 48 scan lines, each waveform contains more temporal information, facilitating more accurate detection of the true 50% upstroke. In the case of 16 scan lines, the relatively low SNR_{PWV} may be attributed to fewer regression points due to decreased spatial resolution.

In addition to SNR_{PWV}, r^2 saturation also plays a role in determining the optimal combination of spatial and temporal resolution, as shown in Figure 4. The frame rate and line density must both be high enough so that the likelihood of low r^2 resulting from insufficient spatial and temporal resolution is minimized. Temporal interpolation serves to maximize the r^2 magnitude when the frame rate is low. The *ex vivo* results in Figures 5 and 6 indicate that for scan line quantities > 32, temporal upsampling factors < 8 may result in false (i.e. unsaturated) r^2 values. Based on the results from both canine aortas, the optimal combination of parameters for PWVs ~ 2.5 – 3.5 m/s will likely be a scan line density between 0.63 (24/38) and 1.26 (48/38) lines/mm with a temporal upsampling factor of 4 or more.

The two *ex vivo* aortas came from two different canines and may also have been subject to different levels of tension, which may explain the difference in their PWV values. Because the specimens were embedded in a water bath for the *ex vivo* experiment, they were stretched to a certain length in order to minimize rigid motion. The effects of longitudinal stretch on pulse wave propagation are under investigation in ongoing studies [123]. However, the goal of this experiment was to merely generate a pulse wave through the specimens and evaluate the reproducibility in each.

Complete validation of the beam sweep compensation scheme requires knowledge of the exact value of the ground truth PWV. This can be done through mechanical testing to find the Young's modulus of the specimen and using the Moens-Korteweg equation to derive PWV. However, the Moens-Korteweg equation is based upon several major simplifying assumptions such as uniform vessel geometry and zero wave reflections [26], which do not apply in our *ex vivo* experiments nor *in vivo*. Future work will focus on the utilization of pressure sensors and Doppler ultrasound to find the true PWV reference through flow velocity and pressure wave measurements in *ex vivo* canine aortas. Ongoing studies are also aimed at the implementation and performance assessment of PWI using plane wave imaging sequences, and preliminary results will be presented in Chapter 6.

Previous studies have suggested that the foot of the pressure waveform or the point of maximum upslope is best suited for the measurement of local PWV [80, 131] due to lower interference from noise and reflections. In this study, wall displacement waveforms were used instead of pressure waveforms. Our *in vivo* results indicated that for clinical PWI in normal human aortas and carotid arteries, tracking the 50% upstroke consistently yielded the most precise PWV measurements (highest SNR_{PWV}) and most reliable r^2 values (highest magnitude). The low SNR_{PWV} from tracking the zero-crossing may be explained by the degree of separation between the waveforms. For example, the normalized displacement waveforms shown in Figure 2.5e appear relatively close together near the zero-crossing, while exhibiting more separation in their upstrokes. The closer the waveforms are, the more difficult it is to distinguish them, which may explain the higher variability in the PWV values arising from tracking the zero-crossing.

Identification of the maximum derivatives requires taking the gradients of the normalized displacement waveform. It is well known that the gradient operation results in displacement noise amplification [149]. Figure 2.2 illustrates the noise that arises when performing the first and second gradient operations. The noise in the first derivative curve may cause shifts in the position of its peak, and the more severe noise in the second derivative curve renders peak identification unreliable. This may explain why the maximum first and second derivatives were not as precise as the 25% and 50% upstrokes.

The PWV is believed to vary over the cardiac cycle because different points on the waveform correspond to different levels of pressure exerted on the wall [26]. For example, we would expect that tracking the peak would yield a higher mean PWV compared to the other features because we are following the wave during peak systole. This was the case in the aorta, but not the carotid artery. Tracking the zero-crossing (end diastole) yielded lower mean PWVs in the carotid arteries, but not in the aorta. In both vessels, the 25% upstroke, 50% upstroke, and maximum first derivative yielded very similar PWVs because they all lie on the waveform upstroke (Figure 3.4a).

Due to the variation of the waveform morphology along the arterial tree [26], tracking the same waveform feature at different imaging sites may yield different results. In addition to imaging location, the PWV and morphology may vary depending on the disease state. For the *in vivo* part of this study, efforts to standardize the imaging location across all subjects were made by scanning immediately upstream from the carotid and iliac bifurcations, which both serve as reflection-generating sites [29]. Thus, it is possible that the *in* vivo results presented in this paper are specific to the standardized imaging location and the normal subject population. However, the scope of this paper was to form and test a theoretical and experimental basis on which to optimize the consistency and reliability of the PWI measurements. The framework that was introduced and implemented in this paper may be used in future studies to examine different imaging locations and disease states.

Conclusions

The conclusions from this study serve to improve the clinical utility of PWI for more accurate diagnosis and characterization of cardiovascular disease. In cases of disease such as aneurysm and atherosclerosis, the altered geometry and mechanical properties of the vessel results in non-uniform pulse wave propagation patterns, and hence the PWV may vary within the imaged segment. By eliminating the imaging and signal processing factors that may contribute to imprecise PWV and low r^2 measurements, we may be able to more reliably detect variations in disease cases.

Chapter 4

Feasibility Study in Hypertensive and Aneurysmal Human Aortas

4.1 Introduction

From September 2010 to August 2011, our group conducted an *in vivo* pilot study to assess the clinical feasibility of PWI in normal, hypertensive, and aneurysmal human abdominal aortas. The results were published in *Physics in Medicine and Biology* [120]. While the mechanical properties are expected to remain mostly uniform over short aortic segments in normal subjects, this may not be the case in pathological subjects. We hypothesized that the quantitative measurements of local aortic PWV and r^2 provided by PWI, as well as qualitative observation of the PWI images and spatio-temporal maps, may provide new insights into arterial wall dynamics and pulse wave propagation in the normal, hypertensive and AAA subject groups.

4.1.1 Background on hypertension (HTN)

Hypertension is a highly prevalent cardiovascular risk condition that may affect up to 90% of individuals in their lifetime [21]. Although the exact mechanisms of hypertension are largely unknown, it is firmly believed that the pulse pressure in large arteries is a key determinant of the degenerative changes that characterize hypertension [150]. Thus, assessment of the aortic elasticity may be of great clinical interest for the general understanding of hypertension. Due to the load-bearing of collagen at high pressures [29], we expect an increase in the intraluminal pressure to exert a greater force on the wall, engaging more stiff collagen fibers and theoretically increasing the stiffness and associated PWV of the aorta.

4.1.2 Background on abdominal aortic aneurysm (AAA)

The abdominal aortic aneurysm (AAA) is responsible for 15,000 fatalities annually in the United States and is the 10th leading cause of death [151, 152]. An AAA is a focal dilation of an abdominal aortic segment that may asymptomatically progress for several years [19]. If undetected or left untreated, AAA rupture carries a 75-90% mortality rate [3]. In current clinical practice, the risk of rupture is assessed by measuring the transverse diameter of the aneurysm during an abdominal ultrasound or computed tomography (CT) exam. The risk of rupture is thought to be highest when the diameter reaches 5 – 5.5 cm [153, 154]. However, AAAs have been known to rupture without a significantly increased diameter [155], while autopsy studies have suggested that AAAs greater than 5 cm in diameter correlates with only 40% chance of rupture [156]. This poses a serious dilemma for surgeons when the risk of rupture is higher than the risk of the procedure itself. In addition, only six countries in the world [157] have implemented a standard clinical screening procedure for AAAs, which are mostly discovered incidentally during routine physical or radiographic exams performed for unrelated reasons [3].

Clinical observations show that the formation, expansion, and rupture phases of an AAA (Figure 4.1) are each associated with changes in arterial stiffness, mainly driven by elastin and collagen degradation [3, 18, 158]. Changes in the composition and structure of the arterial wall will alter its mechanics. During the early stages of AAA formation, elastin begins to depredate while collagen production increases [26], raising the collagen-to-elastin ratio of the aorta and increasing its stiffness. Subsequent collagen degradation causes the aneurysm to expand slowly. As collagen degradation accelerates in the later stages of AAA expansion, the remodeling ability of the AAA is undermined, leading to rapid expansion and potential rupture. Thus, elastin degradation is the key step in the formation of AAAs, whereas collagen degradation is ultimately required for rupture [3].

The Moens-Korteweg equation does not apply in aneurysmal cases because the equation is based on the assumption that the vessel has a uniform radius. However, the biomechanical and geometric changes associated with an AAA will undoubtedly alter the pulse wave propagation behavior. Due to its ability to directly visualize and spatio-temporally map the pulse wave, PWI can potentially serve as a valuable clinical tool for noninvasive characterization of AAAs *in vivo*.

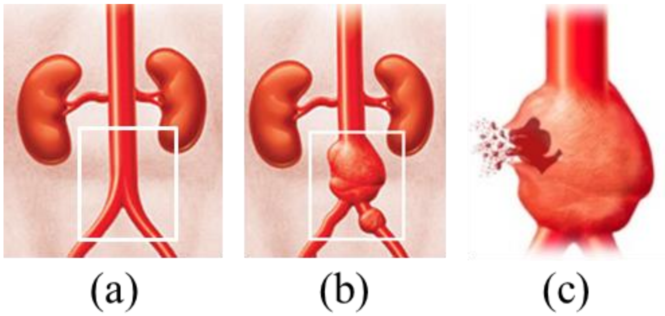

Figure 4.1: (a) A normal aorta is generally cylindrical in geometry and exhibits a collagen-to-elastin ratio of ~ 1.58 [26]. The majority of AAAs occur at the infrarenal abdominal aorta (i.e. the segment below the renal artery branches) indicated by the white square. (b) During the early stages of AAA formation, elastin depredates while collagen production increases. Subsequent collagen degradation then causes the aneurysm to expand slowly. (c) Rapid AAA expansion may occur as a result of the collagen degradation. When the stress on the aortic wall exceeds its strength, AAA rupture may occur.

4.2 Study Design

4.2.1 Patient recruitment and exclusion criterion

In vivo imaging studies approved by the Institutional Review Boards of St. Luke's-Roosevelt Hospital Center and Columbia University were conducted on patients who had been diagnosed with hypertension (systolic blood pressure ≥ 140 mmHg recorded 0-2 days prior to imaging) and/or untreated AAAs. Patients who were on anti-hypertension medication at the time but had a previous history of hypertension were also regarded as hypertensive subjects. Out of the 29 total hypertensive and 11 total AAA patients imaged, 11 hypertensives and 6 AAAs were excluded due to poor B-mode image quality. The remaining hypertensive subjects (10 F, 8 M) had an average age of 65.4 ± 18.3 years. The remaining AAA subjects (3 F, 2 M) had an average age of 71.6 ± 11.8 years and AAA diameters of 3.9, 4.1, 4.6, 6.0, and 6.1 cm). In addition, 15 healthy volunteers (mean age 32.5 years ± 10.2) were imaged as a control group.

4.2.2 Data acquisition

The targeted imaging region was the infrarenal abdominal aorta, which is where nearly 90% of aortic aneurysms occur [3]. Ultrasound RF signals were acquired from each patient in the supine position using a Sonix RP system (Ultrasonix Medical Corporation, Burnaby, Canada) with a 3.3 MHz curvilinear transducer in the long-axis orientation. RF signals were collected in 2.5-second acquisitions and digitized at 20 MHz to ensure capture of at least one full cardiac cycle per acquisition. For each subject, 5-8 acquisitions were performed so that the PWV measurements could be averaged over multiple cardiac cycles. To minimize rigid motion, the subjects were requested to perform breath-holding for the duration of each acquisition.

The imaging depth was set at the minimum depth required to visualize both the anterior and posterior aortic walls. Since an increase in depth leads to a decrease in frame rate, the scan line density sand/or the ultrasonic image plane size was reduced in subjects with deeper aortas in order to ensure a high frame rate. The image plane size was also reduced for subjects in which abdominal gas or artifacts obstructed the full view of the aorta. Consequently, the imaging depth varied from 7-15 cm, the scan line quantity varied from 16-32, and the image plane size varied from 60-100% of the full field of view. This resulted in frame rates between 242 and 462 Hz. Based on Equation 3.1 from the previous chapter, the imaging parameters used in this study yielded maximum measurable PWVs of ~ 21.26 – 28.08 m/s.

4.2.3 Data processing

The inter-frame axial displacements were estimated offline using a fast normalized 1D cross-correlation method on the RF signals [137] with a 3.5-mm window size and 80% overlap. Both the anterior and posterior walls were manually segmented in the first frame of each acquisition sequence and updated automatically in subsequent frames based on the inter-frame displacements. The normalized displacements were color-coded and overlaid onto the corresponding 2D B-Mode images reconstructed from the RF signals. For visualization, the displacements in both the anterior and posterior aortic walls were shown, although the spatio-temporal map was generated using only the anterior wall displacements.

For PWV estimation, the 50% upstroke in each waveform was identified as the fiduciary point for waveform tracking as described in Section 3.2.2. Linear regression of the relationship between the 50% upstroke arrival time and the length of the anterior wall yielded the slope as the PWV and the r^2 as an approximate index of the wave propagation uniformity. If the PWV exceeded the maximum measurable PWV at the given frame rate and scan line density (PWV_{max} in Eqn. 3.1), the measurement was deemed unreliable. The PWV was corrected to compensate for the beam sweeping-induced time delays in the pulse wave arrival times as described in the Appendix.

4.3 Results

4.3.1 Qualitative results

Figure 4.2 shows consecutive PWI frames (B-Mode overlaid with pulse wave-induced wall displacements) illustrating the propagation of the pulse wave in one representative normal (4.2a), hypertensive (4.2b), and AAA (4.2c) subject. The arrival of the pulse wave induces an upward (i.e. towards the transducer) motion in the anterior wall, as indicated by the red overlay. The arrows indicate the apparent position of the 50% upstroke of the waveform as it propagates from proximal (closest to the heart) to distal (closest to the iliac bifurcation) across the imaged segment. In the normal aorta (4.2a), the wave propagation can be clearly visualized. In the hypertensive case (4.2b), the propagation of the wavefront is still apparent, however is marked by a deterioration of the wall motion at the proximal end of the imaged segment as the wave is still propagating. This is a phenomenon that was not observed in any of the normal cases, and may represent a relatively stiff region in the imaged segment and/or a peak narrowing of the waveforms at the proximal end. Wave propagation can also be visualized in the AAA case (4.2c), however the focal dilation of the wall rendered identification of the wavefront more difficult. Echogenic regions can be seen in the aneurysm sac, indicating potential intraluminal thrombi and/or atherosclerotic regions.

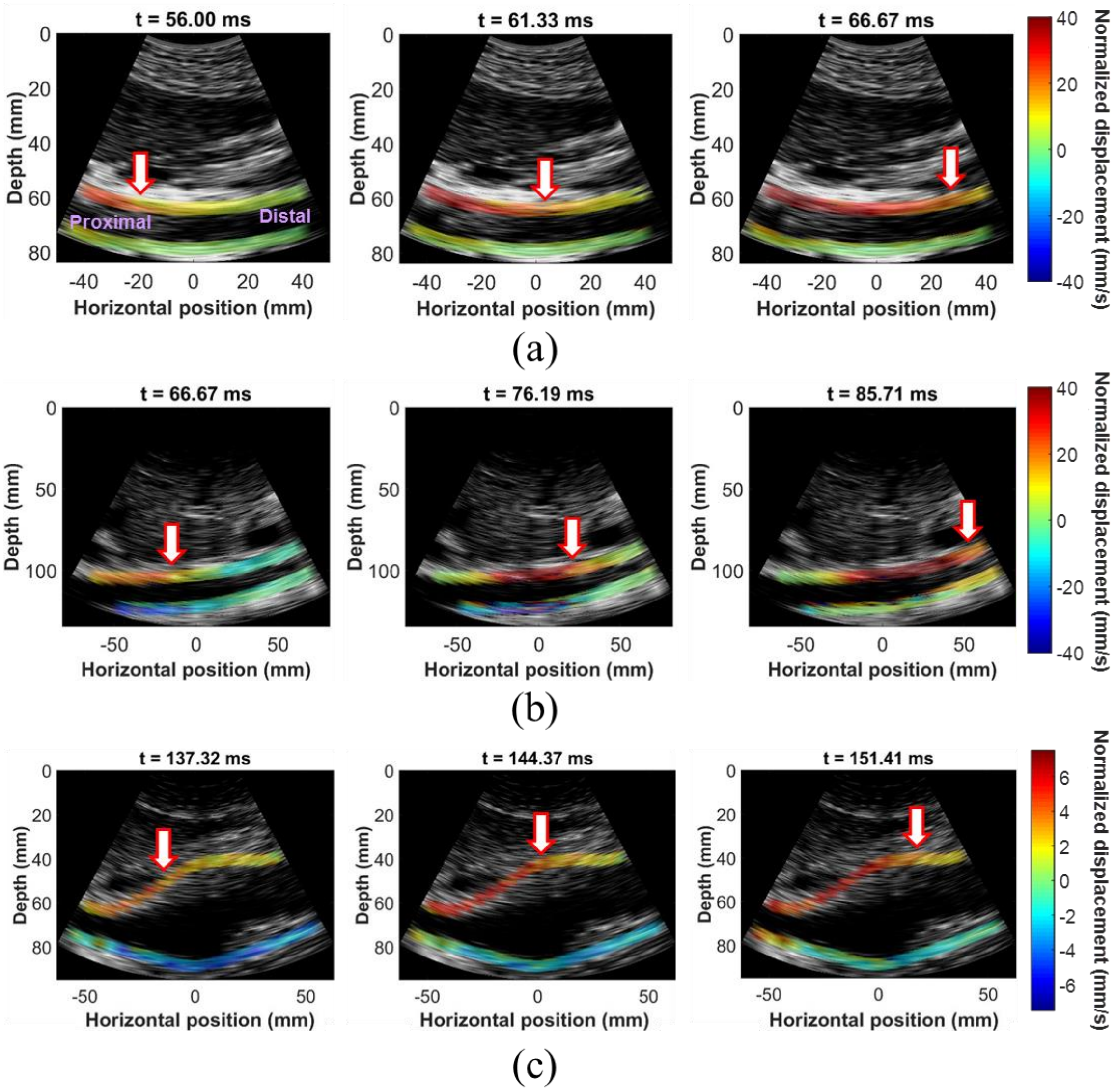
t = 56.00 ms
t = 61.33 ms
t = 66.67 ms
Depth (mm)
Horizontal position (mm)
Proximal
Distal
Normalized displacement (mm/s)
40
20
0
-20
-40
t = 66.67 ms
t = 76.19 ms
t = 85.71 ms
t = 137.32 ms
t = 144.37 ms
t = 151.41 ms
6
4
2
0
-2
-4
-6

(a)

(b)

(c)

Figure 4.2: Consecutive PWI frames (B-mode image overlaid with pulse wave-induced displacements) showing the propagation of the pulse wave along the anterior aortic wall in (a) a normal (23, M), (b) a hypertensive (42, F), and (c) a 6.0-cm diameter AAA (72, F) subject. The time stamp represents the time elapsed from the beginning of the PWI cine loop and is not intended to correlate with a particular point in the cardiac cycle. For the AAA case, the dynamic range of the normalized displacements was reduced for more clear visualization of the pulse wave propagation.

Figure 4.3 shows the spatio-temporal maps and waveform plots of the anterior aortic wall displacement in three normal subjects, ages (a, b) 23, (c, d) 31, and (e, f) 55. The subject presented in (a, b) is that same as that presented in 4.2a. Figure 4.4 shows the spatio-temporal maps and waveform plots of the anterior aortic wall displacement in three hypertensive subjects, ages (a, b) 42, (c, d) 77, and (e, f) 45. The subject presented in (a, b) is that same as that presented in 4.2b.

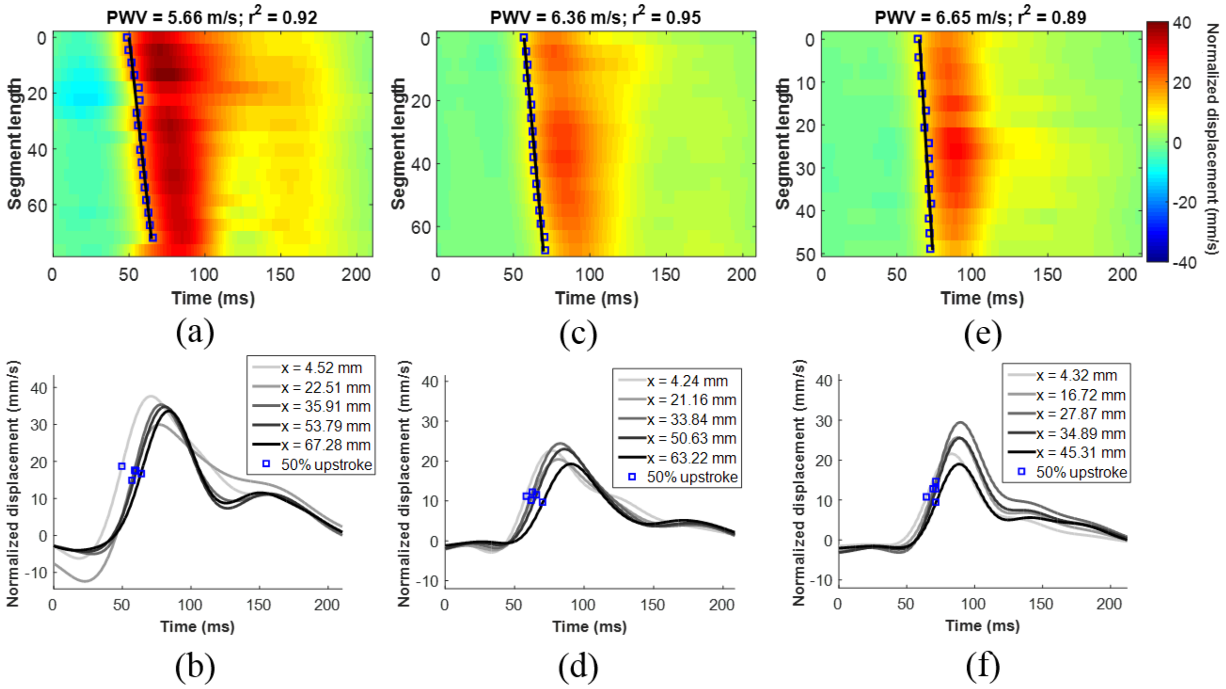

Figure 4.3: (a, c, e) Spatio-temporal maps of the anterior aortic wall displacement in three normal subjects, ages (a) 23, (c) 31, and (e) 55. (b), (d), and (f) show the displacement waveforms at five locations along the imaged segment corresponding to the spatio-temporal maps in (a), (c), and (e), respectively. The blue squares represent the 50% upstroke in each waveform as it propagates along the wall. The PWV and r^2 values were obtained from the linear regression of the spatio-temporal variation of the 50% upstroke, represented by the black line in (a), (c), and (e). (a) and (b) correspond to the same subject shown in 4.2a.

In all normal and hypertensive cases shown, the waveform propagated in a uniform fashion ($r^2 \geq 0.89$). However, the hypertensive waveforms appeared to be more variable over the cardiac cycle compared normals. For example, the waveform in the normal aortas shown in 4.3b, 4.3d, and 4.3f maintained similar amplitude and morphology throughout its propagation. In the hypertensive cases shown in Figures 4.4b and 4.4f, both the amplitude and morphology of the waveform at different positions along the imaged segment are noticeably variable. The deterioration of the wall motion at the proximal end in the hypertensive subject shown in Figure 4.2b is reflected in the corresponding spatio-temporal map (4.3a), where reduced displacement amplitudes can be seen near the top of the image where the pulse wave enters the field of view. In the hypertensive case shown in Figure 4.4 (c and d), the waveform widened around the peak and decreased significantly in amplitude compared to the normal and other hypertensive cases shown.

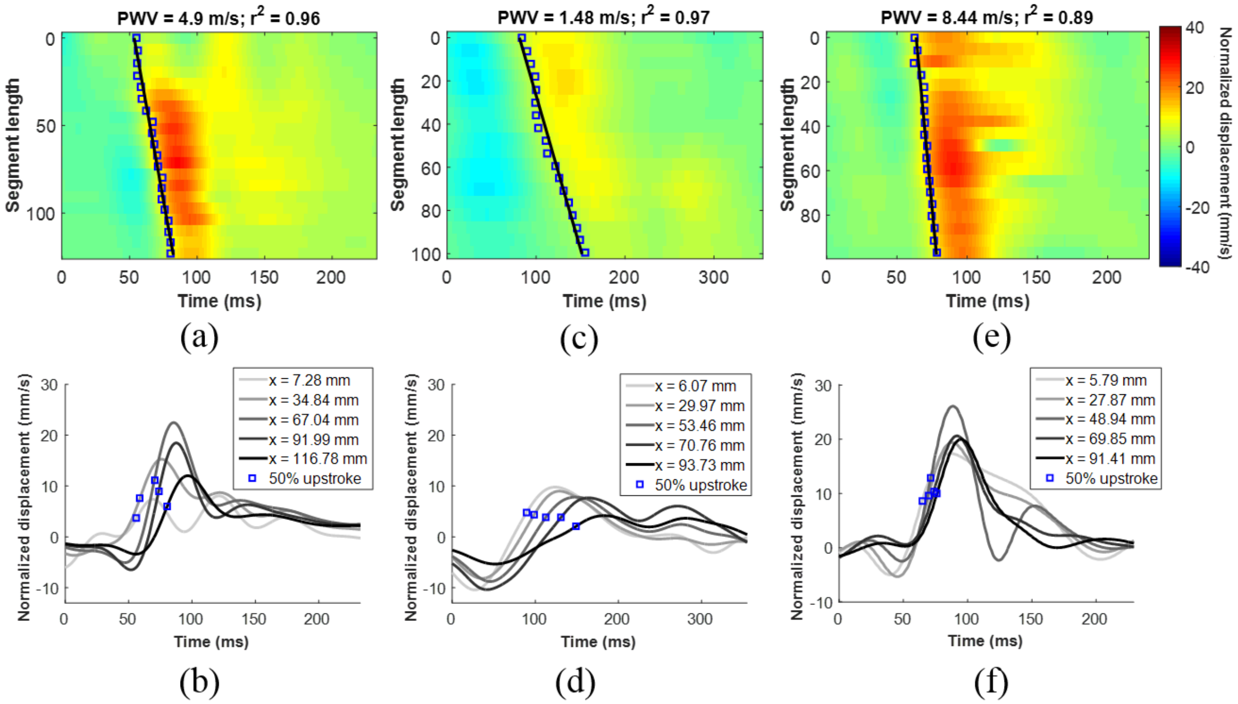

(a) (c) (e)

(b) (d) (f)

Figure 4.4: (a, c, e) Spatio-temporal maps of the anterior aortic wall displacement in three hypertensive subjects (a) 42, (c) 77, and (e) 45. (b), (d), and (f) show the displacement waveforms at five locations along the imaged segment corresponding to the spatio-temporal maps in (a), (c), and (e), respectively. The blue squares represent the 50% upstroke in each waveform as it propagates along the wall. The PWV and r^2

values were obtained from the linear regression of the spatio-temporal variation of the 50% upstroke, represented by the black line in (a), (c), and (e). (a) and (b) correspond to the same subject shown in 4.2b.

Figure 4.5 shows the spatio-temporal maps and waveform plots of the anterior aortic wall displacement in three AAA subjects, ages (a, b) 72 (6.0 cm AAA), (c, d) 80 (4.1 cm AA), and (e, f) 66 (4.6 cm AAA). The magenta lines on the spatio-temporal maps indicate the boundaries of the dilated aneurysmal segment as qualitatively approximated from the B-Mode images. The subject presented in (a, b) is that same as that presented in 4.2c. In (c) and (e), PWV estimation was performed using only the 50% upstroke markers exhibiting a linear trend.

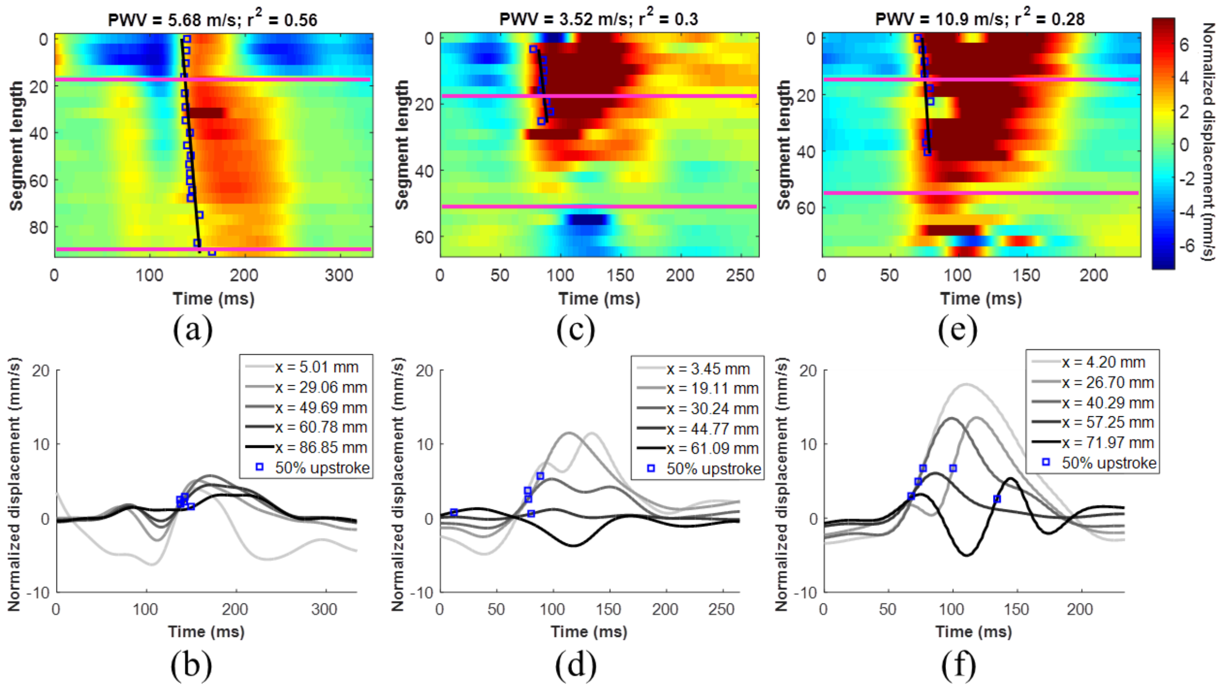

(a) (c) (e)

(b) (d) (f)

Figure 4.5: (a, c, e) Spatio-temporal maps of the anterior aortic wall displacement in three AAA subjects, aged (a) 72 (6.0 cm AAA), (c) 80 (4.1 cm AAA), and (e) 66 (4.6 cm AAA). (b), (d), and (f) show the displacement waveforms at five locations along the imaged segment corresponding to the spatio-temporal maps in (a), (c), and (e), respectively. The blue squares represent the 50% upstroke in each waveform as it propagates along the wall. The upstroke markers that were not part of a positive linear trend were manually

removed, and remaining makers were used for PWV and r^2 estimation via linear regression, represented by the black line in (a), (c), and (e). (a) and (b) correspond to the same subject shown in 4.2c. The pink lines in (a), (c), and (e) indicate the boundaries of the dilated aneurysmal segment as qualitatively approximated from the B-Mode images.

All three AAA cases shown exhibited highly non-uniform wave propagation ($r^2 < 0.6$) along with decreased wall displacement amplitudes either towards the distal end of the sac (4.5a and 4.5e) or in the middle (4.5c). Also, a downward motion (i.e. away from the transducer) in the aortic segment located immediately after the sac was observed in cases 4.5c and 4.5e, indicated by the blue region at the bottom of the spatio-temporal map. This phenomenon was observed in three out of the five total AAA cases. In order to further investigate this observation, one of the PWI frames from the time at which the downward motion occurred is shown in Figure 4.6 for cases 4.5c, 4.5e, and a third case (68, M, 3.9 cmm AAA). In all three cases, the aneurysmal segment appears to exhibit a “teetering” motion where the entire vessel (i.e. both the anterior and posterior walls) moves upwards at the proximal end (red arrow) and downward at the distal end (blue arrow) upon arrival of the pulse wave. This phenomenon was observed in the three AAAs where the diameter was less than 5.5 cm (4.1, 4.6, and 3.9 cm), but not in the AAAs whose diameters exceeded 5.5 cm (6.0 and 6.1 cm).

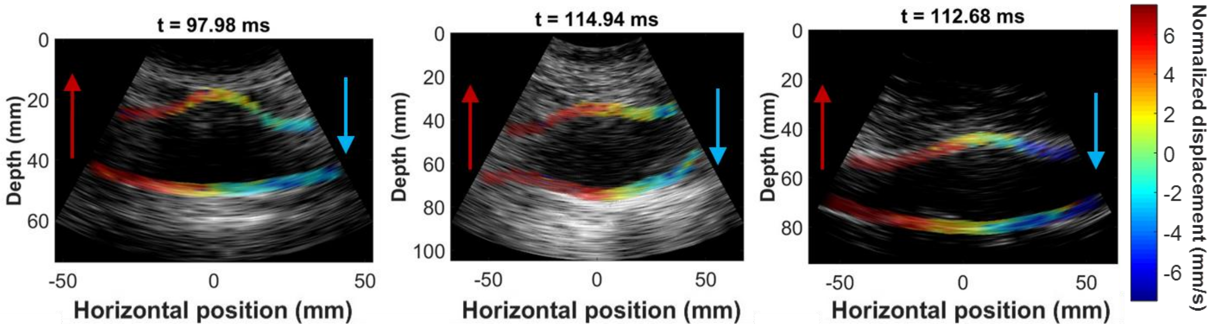

(a) (b) (c)

Figure 4.6: PWI frames showing the "teetering" phenomenon (i.e. upward motion at the proximal end and downward motion at the distal end, as indicated by the red and blue arrows, respectively) of the aneurysmal segment that was observed in three out of the five AAA cases. (a) and (b) correspond to the cases in 4.5c/d and 4.5e/f, while (c) represents a 68 y.o. male with a 3.9 cmm AAA. The time stamp represents the time elapsed from the beginning of the PWI cine loop and is not intended to correlate with a particular point in the cardiac cycle.

4.3.2 Quantitative results – PWV and r^2

Five hypertensive subjects exhibited a negative PWV and were excluded from the results presented in this study. Due to branching and vascular inhomogeneities, the waveform at each beam location is a combination of the incident wave originating from the heart and possibly multiple reflected waves originating from the downstream periphery [26, 29]. Observation of a negative PWV may likely have arisen from the inability to distinguish the forward wave from the reflected wave(s) due to insufficient frame rate and/or complex waveform mixing. The PWV measurements averaged over at least five cardiac cycles for each remaining subject are shown in Figure 4.7. The PWVs in the hypertensive and AAA subjects were more variable than those in the normal subjects as indicated by the error bars.

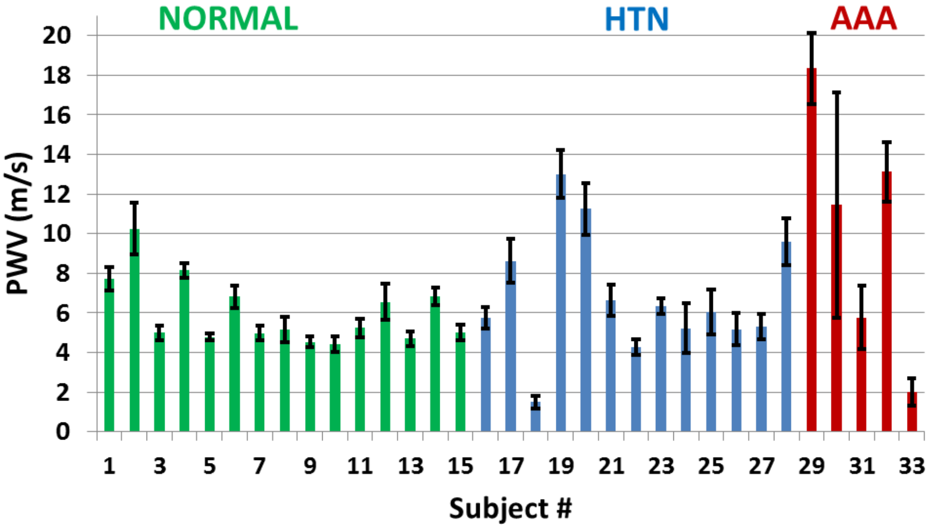

Figure 4.7: PWV measurements averaged over at least five cardiac cycles for each subject. Standard deviations are shown as black error bars.

The average PWV in all normal, hypertensive, and AAA subjects was 6.03 ± 1.68, 6.69 ± 2.80, and 10.54 ± 6.52 m/s, respectively (Figure 4.8a). There was no significant difference ($p = 0.15$ measured using a two-sample t-test) between the PWVs in the normal and hypertensive subjects. However, the PWVs in the AAA subjects were significantly higher ($p < 0.001$) compared to those in the other two groups. The average r^2 in all normal, hypertensive, and AAA subjects was 0.93 ± 0.05, 0.88 ± 0.11, and 0.46 ± 0.23, respectively (figure 7b). Although the r^2 of the normal and hypertensive aortas were not significantly different ($p = 0.04$), that of the AAA subjects was significantly lower ($p < 0.001$) than that of the other two subject groups.

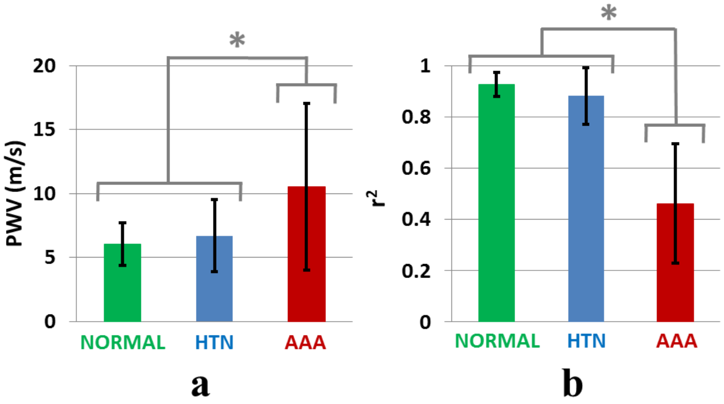

Figure 4.8: (a) PWV and (b) r^2 averaged over all subjects for each of the three subject groups. Standard deviations are shown as black error bars. The average PWV in all normal, hypertensive, and AAA subjects was 6.03 ± 1.68, 6.69 ± 2.80, and 10.54 ± 6.52 m/s, respectively. The average r^2 in all normal, hypertensive, and AAA subjects was 0.93 ± 0.05, 0.88 ± 0.11, and 0.46 ± 0.23, respectively. * denotes statistical significance with $p < 0.001$ measured using a two-sample t-test.

4.4 Discussion & Conclusions

This study demonstrated the capability of PWI to spatio-temporally map the propagation of the pulse wave as a wall velocity wave in the infrarenal abdominal aortas of normal, hypertensive, and aneurysmal human subjects. Compared to other imaging methods for estimating PWV based on MRI [82, 159, 160] and Doppler imaging [86, 161, 162], the high temporal resolution of PWI allows for the acquisition of multiple waveforms (i.e. equal to the beam density) along short aortic segments over a single cardiac cycle, thus providing many temporal and spatial samples for PWV estimation as well as fused functional and anatomical images at high frame rates showing simultaneously the vessel structure and wall motion (Figure 4.2).

It is worth noting that there existed an angle-dependence in the motion estimation arising from the use of a curvilinear probe and the fact that anatomically, the aorta may have been oriented such that the direction of wall motion was not exactly parallel to the ultrasound beams. This may have resulted in estimated axial displacements that were only an off-angle component of the true displacement magnitude. In this study, efforts to correct for the angle dependence were made by estimating the angle between the manually segmented aortic wall and the ultrasound beams, then scaling the displacement amplitudes by the cosine of the angle. However, since this study focused on measuring the pulse wave velocity, the arrival time of the waveform at each scan line position was of greater importance rather than the waveform magnitudes themselves. Since the same field of view was maintained for the duration of each acquisition, the direction of wall motion at each scan line location maintained the same angle with the beam. Thus, although the estimated axial displacements may have been smaller than the true displacements, the estimated displacement waveform at each beam location maintained the same morphology as the true displacement waveform. This would not have affected the waveform tracking, since the 50% upstroke was identified relative to the peak and the foot in each waveform.

In addition to pulse wave-induced radial expansion, the abdominal aorta also experiences longitudinal motion [163]. Since the pulse wave propagates by inducing radial displacements in the vessel wall, only the axial component of wall motion was estimated in this study while the longitudinal motion was neglected. Future studies will be aimed at using 2D motion estimation methods to estimate the lateral wall displacement for more complete wall motion analysis.

Qualitatively, the wave propagation in normal aortas was the most uniform, whereas the amplitude and morphology of the successive waveforms over the cardiac cycle appeared to be more variable in hypertensive aortas. In all AAA cases, the dilated vascular wall resulted in highly variable waveform morphologies, decreased wall motion within the aneurysm sac, and a “teetering” phenomenon characterized by upward motion of the entire vessel at the proximal end and downward motion at the distal end, masking the arterial dilation. This phenomenon was observed in the three smallest diameter aneurysms (3.9 cm, 4.1 cm, 4.6 cm), but not in the two larger AAAs (6.0 cm and 6.1 cm).

Quantitatively, the significantly higher [lower] PWV [r^2] estimates in the AAA subjects suggested greater aortic stiffness and less uniform pulse wave propagation compared to the normal and hypertensive subjects. However, the "teetering" phenomenon observed in three out of the five AAA cases may have masked the true pulse wave propagation. The waveforms that were tracked in these cases may have corresponded to the rigid motion instead of the wall displacements induced by the increased pressure and blood flow velocity associated with the pulse wave.

The *regional* aortic PWVs measured using PWI in the normal aortas were consistent with values found in literature obtained using MRI [82, 159, 160], which varied between 4 and 7 m/s. However, most clinical studies that have investigated the *in vivo* relationship between PWV and various pathologies such as hypertension have utilized some form of the foot-to-foot method [37, 40, 42, 164] and thus reported the *global* PWV, which may differ from the *regional* PWV at various sites in the arterial tree. Thus, there is a shortage of existing literature against which to compare the hypertensive and aneurysmal PWV measurements obtained in this study.

Aging and gender

In clinical studies, the principal factors modulating the PWV in the absence of disease are age, blood pressure, and to a lesser extent, gender [165]. In AAA cases, the risk of rupture is four times greater in women than in men [3]. In this study, the normal subjects were significantly younger than the pathological subjects ($p < 0.001$), but both genders were well-represented in all subject groups. However, since the subjects were categorized by pathology, the factors of aging and gender on the aortic properties were not reflected.

Hypertensive subjects

While previous longitudinal studies reported a positive correlation between the carotid-femoral (i.e. *global*) PWV and cardiovascular events in hypertensive patients [40-42, 164], the results from our study indicated that there was no significant difference in the *regional* aortic PWVs between normal and hypertensive subjects. Since aging and hypertension are both assumed to increase arterial stiffness and the hypertensive subjects in this study were significantly older than the normal controls, this raises the question of why the hypertensive subjects did not exhibit a significantly higher PWV. This could be attributed to a number of factors.

In vivo arteries exhibit tapering, branching, and geometrical non-uniformity throughout the arterial tree, resulting in multiple reflection sites [26, 29, 51] such as the iliac bifurcation, which is located immediately downstream from the infrarenal abdominal aorta. The merging of the forward wave and possibly multiple reflected waves at a given site [29] is a phenomenon that becomes augmented by aging and some pathologies [166]. Hence, the PWV measured using PWI was obtained by tracking the resultant of the forward and reflected waves, which travel in opposite directions. Thus, it is possible that the arterial stiffening that is presumed to occur due to aging and hypertension may have caused both the forward and reflected waves to travel faster, resulting in more frequent mixing an apparently slower forward wave. This may also contribute to the greater intra-subject variability in PWV and waveform morphology observed in the hypertensive group. On the other hand, the normal aortas in this study were much younger and less affected by reflections.

Two additional factors in the hypertensive subjects that were not extensively considered in this study were the effects of smoking and response to medication, both of which may affect vascular mechanical properties [167, 168]. Finally, nearly all hypertensive patients in this study had been diagnosed with at least one other pathology such as renal disease, heart disease, or diabetes. Not only can such diseases affect arterial elasticity, they also require the patient to take additional medications which may affect the arterial wall properties.

Considering all the factors indicated above, the complexity of the hypertensive subject group becomes apparent. Since it is virtually impossible to distinguish the individual effects of each confounding factor, the resultant pulse wave propagation patterns and measured PWVs represent the combined effect of each confounding factor on top of the hypertensive conditions

AAA subjects

In AAA cases, the effects of aging, wave reflection, medication, smoking, and confounding pathologies also apply. The problem is further complicated by the complex geometry of the aneurysmal aorta, which can lead to turbulent flow within and near the aneurysm [3]. The drastic variations in the morphology of the successive waveforms due to an aneurysm significantly limit the tracking of a consistent fiduciary point in each waveform, which may explain the high variability of the PWV estimations in AAA subjects. However, the significantly lower r^2 values found in the AAA subjects compared with normal and hypertensive subjects were consistent with previous *in vivo* PWI results on AAA murine models [119], which also showed a decreased r^2 in the presence of an aneurysm.

As previously stated, the presence of the dilated aneurysm sac invalidates the use of the Moens-Korteweg equation to derive the arterial Young's modulus from the PWV. In addition, the change in waveform morphology in AAA subjects may likely depend on augmented reflected waves, geometrical non-uniformity, and inhomogeneous wall mechanics. Thus, changes in waveform morphology and magnitude may not have necessarily been correlated with changes in vascular stiffness. However, due to the positive correlation between arterial stiffness and PWV, future studies will be aimed at incorporating the geometry of the aneurysm to supplement the measurement of PWV as a surrogate of arterial stiffness. The ability of PWI to obtain the actual morphologies of the wall motion waveforms across the aneurysmal segment enables more in-depth analysis of the arterial mechanical properties.

Conclusions

PWI is a promising technique that enables both visual and computational evaluation of the *regional* pulse wave propagation, which could aid in the early detection and characterization of many vascular diseases. The results from this feasibility study demonstrate the potential of PWI to differentiate between normal and pathological arteries through evaluating various features of the pulse wave over complete cardiac cycles. As the sample size increases in this ongoing clinical study, we anticipate the capabilities of PWI to further distinguish among pathological subjects with varying blood pressure, age, gender, and AAA diameter.

Chapter 5

Central pulse pressure measurement using Pulse Wave Ultrasound Manometry (PWUM)

5.1 Introduction

As described in previous sections, hypertension is a highly prevalent cardiovascular risk condition that may exist asymptomatically, causing damage to the heart and arteries. One of the primary reasons that hypertension remains poorly managed is that diagnosis and treatment monitoring are performed using the brachial cuff pressure, which is a peripheral measurement that does not reflect the central blood pressure (CBP) near the heart. Central (i.e. aortic and carotid) pressures are recognized as more pathophysiologically relevant than peripheral pressure for the pathogenesis of cardiovascular disease [54, 169-173]. The distending pressure in the large elastic arteries is a key determinant of the degenerative changes that characterize accelerated aging and hypertension [174]. By contrast, peripheral arteries such as the brachial and the radial arteries are less influenced by these changes [150]. Furthermore, it has been demonstrated that different anti-hypertensive pharmacological treatments may have different effects on the CBP reduction while maintaining similar brachial BP reduction [174, 175], thus supporting the need to account for CBP during hypertension treatment and monitoring. However, in clinical practice, the effect of anti-hypertensive drugs is commonly monitored using solely the brachial BP.

5.1.1 Clinical significance of central pulse pressure

Pulse pressure (PP), defined as the difference between the systolic and diastolic blood pressures (i.e. the pressure increase required to generate a pulse), has been recognized by several studies as a significant predictor of all-cause cardiovascular mortality and morbidity [27, 170, 176]. PP arises from the interaction between cardiac ejection (stroke volume) and the properties of the arterial circulation. An increased stiffness of the large arteries leads to an increase in PP due to a reduction in arterial compliance and increased speed of wave reflections [30]. Clinically, it has been shown that PWV is increased even before significant hypertension can be measured [177], targeting reductions in arterial stiffness as a possible therapeutic intervention.

5.1.2 Current measurement techniques

The PP in peripheral arteries is commonly assessed using cuff sphygmomanometry at the brachial site and applanation tonometry at the radial site [178]. However, the PP in large arteries such as the aorta remains challenging to measure clinically, as the only method to obtain a direct measurement of central PP is by way of a highly invasive arterial catheter. In many longitudinal clinical research studies involving large patient populations [170, 179-182], the aortic pressure waveform has been derived from the radial or carotid waveform using a generalized transfer function to describe the arterial properties between the ascending aorta and the peripheral recording site (Figure 5.1). However, a generalized transfer function assumes that properties of the arterial system between the two sites are the same in all subjects and under all conditions, which is not the case [66, 67]. Thus, indirect methods may not be used for evaluation on an individual case-by-case basis.

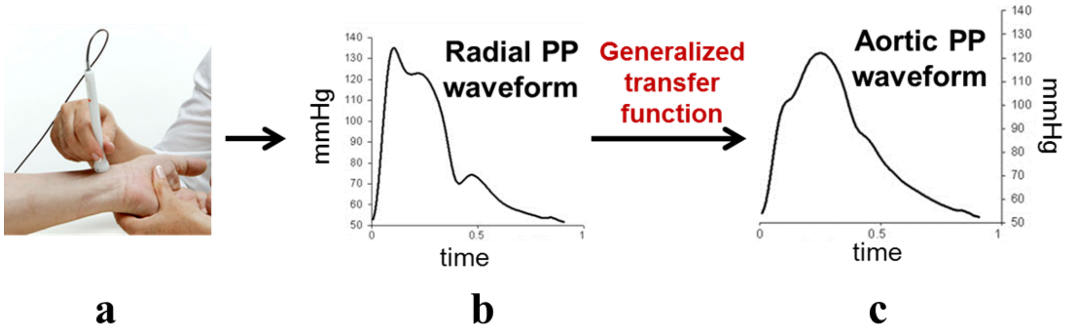

Figure 5.1: Estimation of the central aortic PP waveform using radial applanation tonometry. (a) A tonometer is placed on the surface of the wrist, above the radial artery. (b) The change in pressure is recorded over time to obtain the radial PP waveform. (c) A generalized transfer function is applied to derive the aortic PP waveform in which the reflected wave merges with the forward wave, creating an inflection point before the main peak. Source: Adapted from *Sphygmocor Info Sheet*.

5.1.3 PWUM methodology

PWI has led to the development to of Pulse Wave Ultrasound Manometry (PWUM) [183] as a noninvasive, easy-to-use central PP measurement technique based on the regional pulse wave propagation characteristics obtained using ultrasound elasticity imaging. PWUM can noninvasively provide direct measurement of the pulse pressure in the abdominal aorta, which cannot be done using any other noninvasive technology. A block diagram of the PWUM technique on a human aorta is shown in Figure 5.2. Aortic wall displacements and pulse wave velocity (PWV) are estimated using PWI, and the incremental distension curve is obtained by subtracting the posterior wall displacements from anterior wall displacements at the central scan line to avoid angle artifacts. The theoretical basis for PWUM is formed by combining the Laplace Law [29] and the Modified Moens-Korteweg Equation [26, 184, 185], thus relating an incremental change in fluid pressure (dP) to the PWV, incremental distension (dR), fluid density (ρ), Poisson's ratio (ν), and lumen radius (*R*). The underlying assumption is that the artery is cylindrical, and that the arterial wall behaves as a linear elastic solid. At this stage, such assumptions are inherent to the proposed method and limitations associated with them will be discussed.

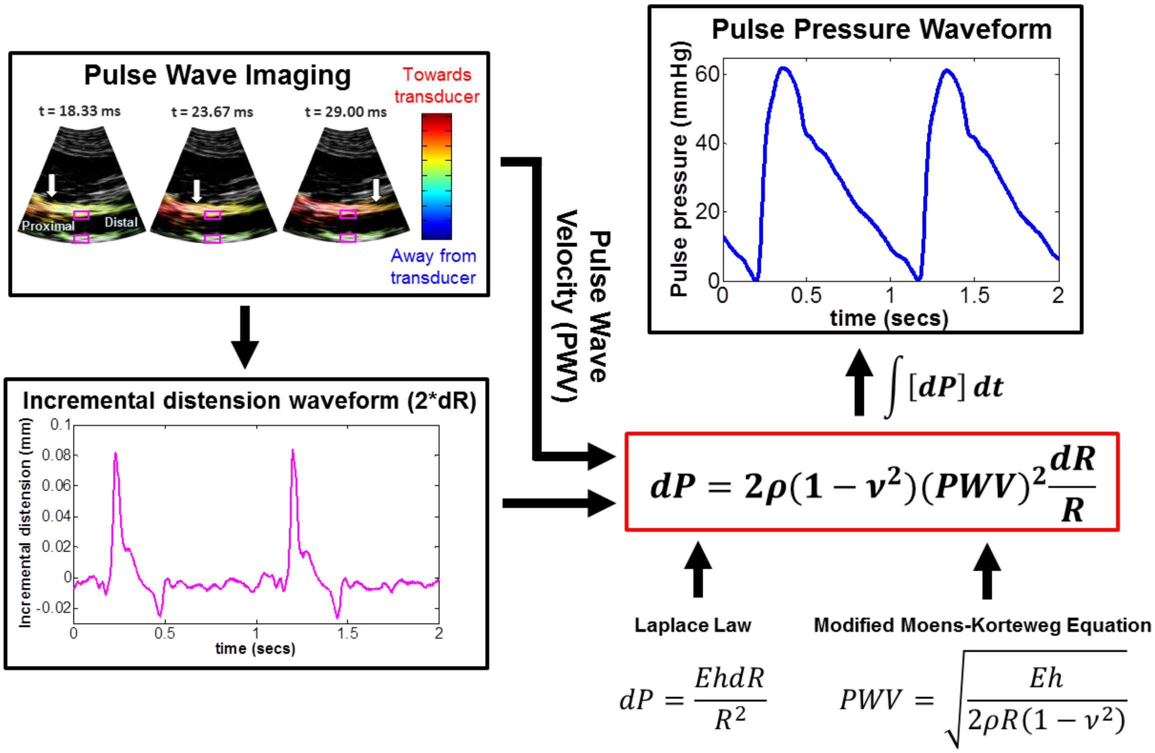

Pulse Wave Imaging
t = 18.33 ms
t = 23.67 ms
t = 29.00 ms
Proximal
Distal
Towards transducer
Away from transducer
Incremental distension waveform (2*dR)
Incremental distension (mm)
0.1
0.08
0.06
0.04
0.02
0
-0.02
0
0.5
1
1.5
2
time (secs)
Pulse Wave Velocity (PWV)
Pulse Pressure Waveform
Pulse pressure (mmHg)
60
40
20
0
0
0.5
1
1.5
2
time (secs)
$\int [dP]\, dt$
$dP = 2\rho(1-\nu^2)(PWV)^2\frac{dR}{R}$
Laplace Law
Modified Moens-Korteweg Equation
$dP = \frac{EhdR}{R^2}$
$PWV = \sqrt{\frac{Eh}{2\rho R(1-\nu^2)}}$

Figure 5.2: Block diagram of the Pulse Wave Ultrasound Manometry (PWUM) method on a human aorta *in vivo*. Pulse Wave Imaging (PWI) provides local PWV measurements by tracking the estimated aortic wall displacement waveform. The incremental distension waveform (pink) obtained at the central scan line (pink squares) was used along with the PWV to arrive at the pulse pressure waveform based on the Laplace law and the Moens-Korteweg equation.

The reproducibility of PWUM has been demonstrated by initial feasibility studies in healthy, normotensive human subjects (~11% average intra-subject variability). Bland-Altman analysis demonstrated excellent correlation (0.94 < r < 0.98) between the aortic PP waveforms obtained using PWUM and those obtained using a commercial applanation tonometry system

(SphygmoCor, Atcor Medical, Sydney, Australia) equipped with a generalized transfer function, however also revealed a significant bias of 4.7 mmHg. This abdominal aorta is generally straight and consists of no major branches aside from the renal arteries [26], making it the imaging site that most closely satisfies the assumptions of the Laplace law and the Moens-Korteweg equation.

The direct, noninvasive measurement of central PP using PWUM allows for routine screening of hypertension and monitoring of BP-lowering drugs based on the PP from multiple arterial sites. While PWUM has been tested in healthy, normotensive subjects [183], it has not yet been used to evaluate patients with elevated blood pressure. This study aims at providing a more complete assessment of PP throughout the arterial tree in order to assess the uniformity of PP elevation (i.e. whether increases in radial and brachial PP are correlated with increases in aortic PP) using direct methods. The PP at three arterial sites were directly measured using three different instruments – cuff sphygmomanometer for the left brachial artery, applanation tonometer for the left radial artery, and PWUM for the infrarenal abdominal aorta.

5.2 Methods and Study Design

5.2.1 Brachial sphygmomanometry

This study was approved by the Institutional Review Board (IRB) of Columbia University. Outpatients visiting the Dental Clinic at Columbia University Medical Center for routine dental exams were recruited. Each patient was instructed to lie in the supine position for the duration of the exam. Three brachial blood pressure measurements were performed on the left arm over a 15-minute period using a clinically recommended [186] automatic digital blood pressure monitor (HEM-705CP, Omron Corp., Kyoto, Japan). The first measurement was excluded, and the average of the latter two was used to classify each subject as pre-hypertensive or hypertensive based on the

American Heart Association (AHA) recommendation for blood pressure categorization (Table 5.1). Brachial PP was calculated as the difference between the systolic and diastolic pressures. Because blood pressure is known to fluctuate throughout the day [187], it was important to perform all measurements as concurrently as possible. In between each brachial cuff measurement, PWUM and radial applanation tonometry were performed to obtain the PP waveform in the aorta and left radial artery, respectively. Only the subjects who exhibited a clear, unobstructed acoustic window of an infrarenal abdominal aortic segment were included in this study. This resulted in N = 9 pre-hypertensive (5 M, 4 F, mean age 37.8 ± 8.4 y.o.) and N = 5 hypertensive (3 M, 2 F, mean age 54.2 ± 3.1 y.o.) subjects. N = 5 normal subjects (3 M, 2 F, mean age 27.2 ± 3.2 y.o.) were also recruited for comparison, yielding a total subject population of N = 19.

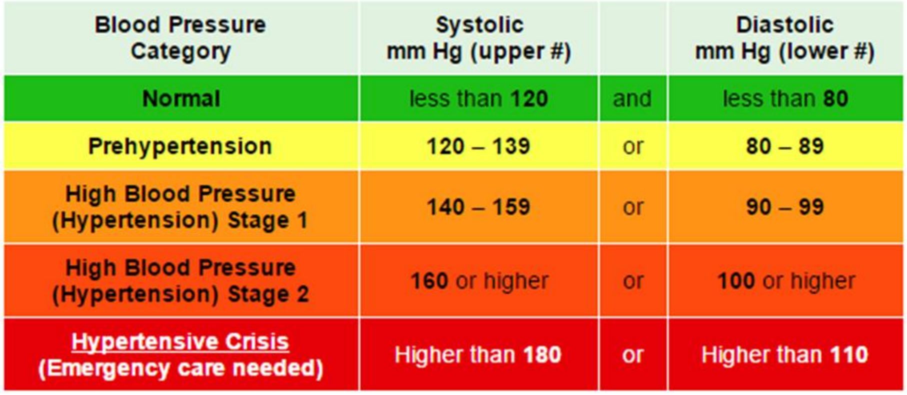

Blood Pressure Category	Systolic mm Hg (upper #)		Diastolic mm Hg (lower #)
Normal	less than **120**	and	less than **80**
Prehypertension	**120 – 139**	or	**80 – 89**
High Blood Pressure (Hypertension) Stage 1	**140 – 159**	or	**90 – 99**
High Blood Pressure (Hypertension) Stage 2	**160** or higher	or	**100** or higher
Hypertensive Crisis (Emergency care needed)	Higher than **180**	or	Higher than **110**

Table 5.1. Blood pressure categories defined by the American Heart Association. Source: *www.heart.org.*

5.2.2 PWUM

The infrarenal abdominal aorta of each subject was scanned in the longitudinal (i.e. long-axis) view using a SonixTOUCH system (Analogic Corp., Peabody, MA, USA) and a 3.3 MHz curvilinear array transducer. Because the pulse wave travels at a high velocity (~ 4-12 m/s in human abdominal aortas [120, 121]), a high frame rate was warranted to adequately track its propagation [188]. The imaging depth was adjusted to the minimum depth so as to visualize both the anterior and posterior aortic walls, and the lateral resolution was reduced to between 19 and 25 scan lines over the field of view. This resulted in imaging depths of 7-12 cm and frame rates of 222-351 Hz, which translated to maximum measurable PWVs [188] of ~ 14.9 – 23.3 m/s based on Eqn. 2.1 in Chapter 2. RF frames were acquired over 2-second intervals during which the subject was required to perform breath holding in order to minimize rigid motion. One additional RF frame was acquired at a high line density (180) to provide a reference frame for accurate manual segmentation of the aortic walls. All RF signals were digitized at a sampling frequency of 40 MHz, and 5-7 acquisitions were performed for each subject in order to average the measurements over multiple cardiac cycles.

The incremental (i.e. inter-frame) axial displacements were estimated offline using a 1-D normalized cross correlation-based motion estimation method [189] on the RF signals with a 1.5 mm window size and 95% overlap. Manual segmentation of the anterior wall was performed on the high line density reference frame, generating a wall trace that was mapped onto the first frame of the RF sequence and automatically updated based on the inter-frame displacements to track the wall throughout the sequence [110]. The displacements at each point along the dynamic trace were mapped over time, generating a 2-D image depicting the spatio-temporal variation of the pulse wave propagation. Waveform tracking was performed by automatically identifying the 50% upstroke [188] of each displacement waveform on the spatio-temporal map, and PWV was estimated via linear regression of the 50% upstroke markers. The incremental distension curve was obtained at the central scan line and inserted along with the PWV into the PWUM framework (Figure 5.2) to arrive at the aortic PP waveform.

5.2.3 Radial applanation tonometry

An applanation tonometry system was assembled and calibrated for the purpose of this study (Figure 5.3) by connecting a SPT-301 noninvasive pulse tonometer to the input channel of a PCU-2000 pressure control unit (Millar Instruments, Houston, TX, USA). The output channel of the control unit was connected to a USB digital I/O device (NI USB-6501, National Instruments Corp, Austin, TX, USA) for data acquisition. The I/O device was controlled by a MATLAB GUI (MathWorks, Natick, MA, USA) that displayed and saved the tonometer signal in real-time on the SonixTouch scanner. Once the pulse in the left radial artery was located by palpation, the tonometer was placed on the top of the artery to record 20 s of radial pressure waveforms.

For each subject, radial and aortic pulse pressures were calculated from their respective waveforms as the amplitude difference between the peak and the beginning of the upstroke (i.e. foot), and averaged over 5-10 cardiac cycles.

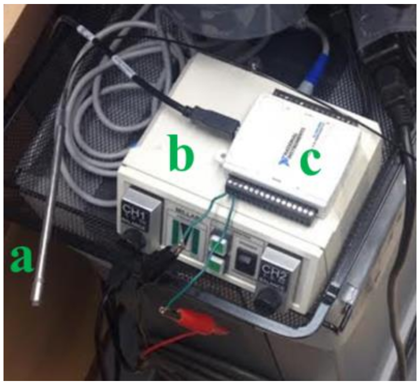

Figure 5.3: Custom applanation tonometry system consisting of (a) a noninvasive pulse tonometer (SPT-301, Millar Instruments, Houston, TX, USA), (b) an amplifier/pressure calibration unit (PCU-2000, Millar Instruments), and (c) a data acquisition device (NI USB-6501, National Instruments, Austin, TX, USA) attached to the back of the SonixTouch scanner (Analogic Corp., Peabody, MA, USA).

5.3 Results

5.3.1 Radial and aortic pulse pressure waveforms

Figure 5.4 shows the radial and aortic pulse pressure waveforms over one full cardiac cycle for (a) a normal subject (F, 23 y.o., brachial BP 113/70) in which radial PP > aortic PP, (b) a pre-hypertensive subject (M, 51 y.o., brachial BP 136/87) in which radial PP ≈ aortic PP, and (c) a hypertensive subject (M, 60 y.o., brachial BP 153/91) in which radial PP ≈ aortic PP. Note the difference in the amplitude scale of the waveforms, which were manually aligned by the foot (i.e. beginning of the upstroke). In each case, the times corresponding to the peak of the forward wave, reflected wave, and dicrotic notch in the radial PP waveform are indicated by blue lines and labels.

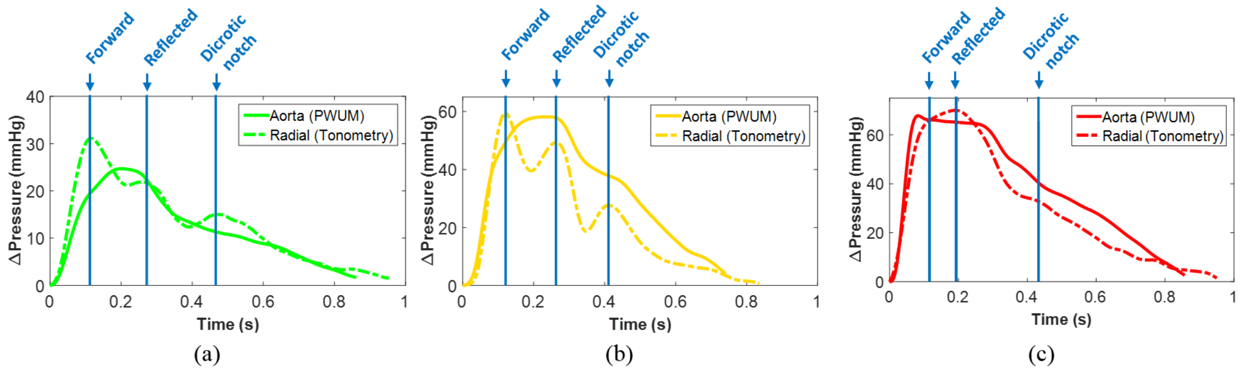

(a)

(b)

(c)

Figure 5.4: Representative radial and aortic pulse pressure waveforms, manually aligned by the foot of the wave, over a full cardiac cycle from (a) one normal subject (brachial BP 113/70), (b) one pre-hypertensive subject (brachial BP 136/87), and (c) one hypertensive subject (brachial BP 153/91). In each case, the times corresponding to the peak of the forward wave, reflected wave, and dicrotic notch in the radial PP waveform are indicated by blue lines and labels.

In the normal and pre-hypertensive cases, the peak of the radial forward wave correlates with an inflection point in the aortic waveform representing the beginning of the augmentation pressure, which is commonly observed in the aorta when the forward and reflected waves merge during late systole [33]. By contrast, the greater separation between the forward and reflected peaks at the radial site indicates that the reflected wave merges with the forward wave during diastole. Also, the amplitude of the radial reflected wave is greater in the pre-hypertensive case compared to the normal case.

The radial waveform in the hypertensive case closely resembles the aortic waveform in the normal and pre-hypertensive cases – the peak of the forward wave appears as an inflection point rather than a relative maximum, suggesting that the higher velocity of the radial reflected wave in the hypertensive case has caused it to merge with the forward wave in late systole [54]. In the aortic waveform, the inflection point corresponding to the radial forward peak is followed by a decrease in pressure rather than the increase seen in the normal and pre-hypertensive cases. This suggests that the reflected wave in the aorta of the hypertensive case may be merging with the forward wave in early diastole rather than late systole [33].

5.3.2 Quantitative results

PWI yielded aortic PWV measurements of 5.00 ± 0.59 m/s, 7.37 ± 1.50 m/s, and 11.69 ± 2.72 m/s in the normotensive, pre-hypertensive, and hypertensive subject groups, respectively. Since PWV is a regional functional index of arterial stiffness over a certain arterial length [190], the significantly higher PWV of the hypertensive group ($p < 0.01$ using two-way ANOVA) suggests that the aortas of the hypertensive subjects were stiffer (i.e. less compliant) than those of the normotensive and pre-hypertensive subjects.

The bar graphs in Figure 5.5 show the blood pressure measurements (brachial systolic, brachial diastolic, brachial PP, aortic PP measured by PWUM, and radial PP measured by applanation tonometry) averaged across each of the three subject groups. For each of the five pressure measurements, statistical significance among the subject groups was determined using two-way ANOVA (*** denotes $p < 0.001$, ** denotes $0.001 < p < 0.01$, and * denotes $0.01 < p < 0.05$). Bonferroni's multiple comparisons test revealed that a significantly higher PP in the hypertensive group was detected only at the aortic site by PWUM, whereas the radial and brachial PPs were not significantly different among the three subject groups.

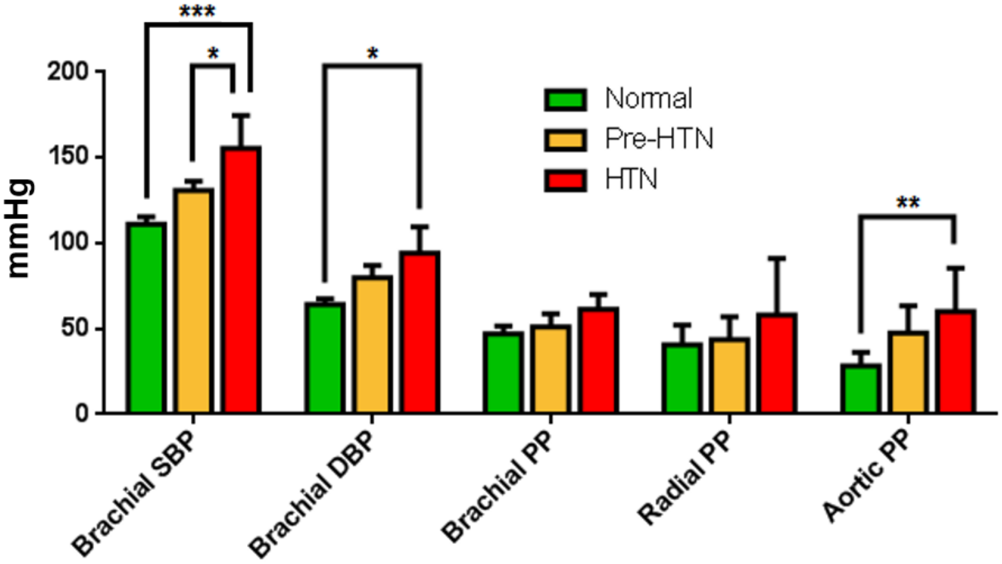

Figure 5.5: Summary of the average blood pressure measurements for each subject group (Pre-HTN = pre-hypertensive, HTN = hypertensive). For each of the five pressure measurements, statistical significances amongst the subject groups were determined using two-way ANOVA (*** denotes $p < 0.001$, ** denotes $0.001 < p < 0.01$, and * denotes $0.01 < p < 0.05$).

The aortic PP vs. (a) radial and (b) brachial PP for all subjects is shown in Figure 5.6. While no strong correlation was observed in normal and pre-hypertensive subjects, there was a relatively strong positive correlation between aortic PP and both radial and brachial PP in hypertensive subjects ($r^2 = 0.68$ and 0.86, respectively).

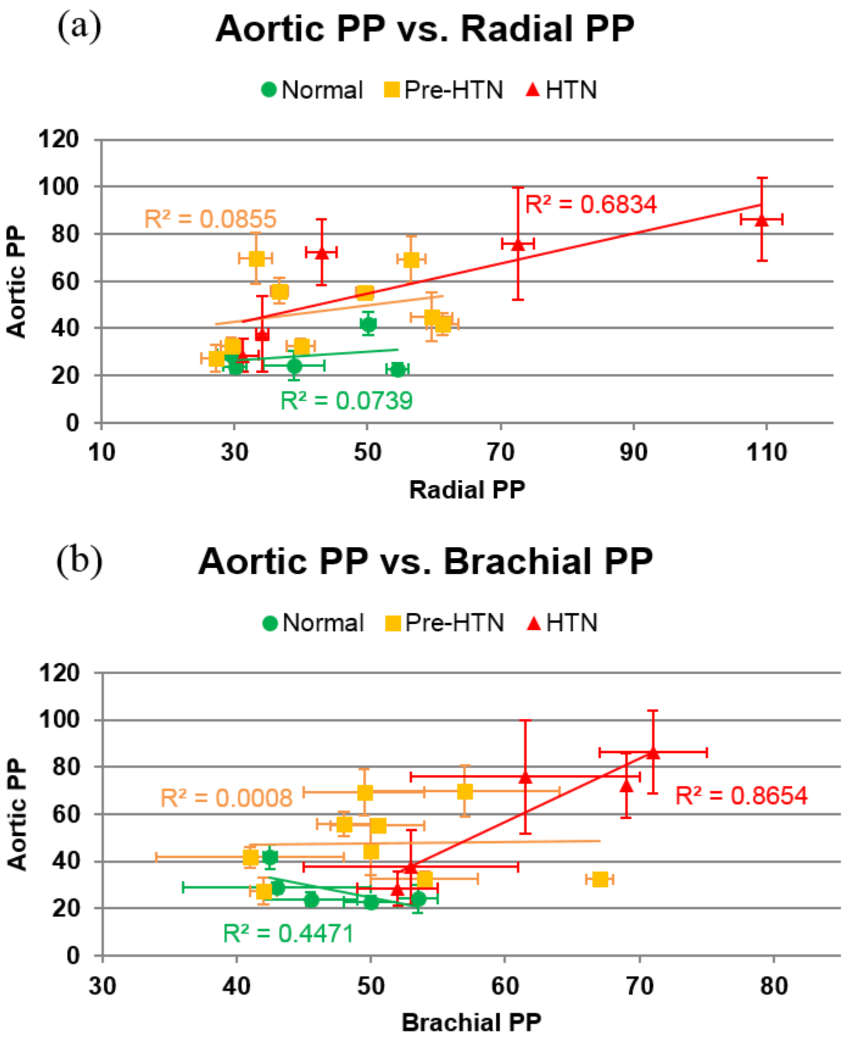

Figure 5.6: Aortic PP vs. (a) radial and (b) brachial PP for all subjects. In both plots, linear regression was performed on the data within each subject group. The greatest correlation between aortic PP and radial/brachial PP was observed in the hypertensive group.

5.4 Discussion and Conclusions

In this study, the aortic PP measured by PWUM was compared to the peripheral PPs measured using radial applanation tonometry and brachial cuff sphygmomanometry in order to evaluate the effects of varying pressure levels throughout the arterial tree. Significantly higher (p

< 0.01) PP in hypertensive subjects was detected at the aorta by PWUM but not in the case of the brachial and radial arteries (Figure 5.5). This supports the notion that changes in overall blood pressure may occur in the central arteries before they are apparent at peripheral sites [175, 191], further stressing the importance of routine CBP evaluation.

It is important to note that the while the subjects represented three distinct blood pressure levels, they also represented three distinct age groups. The pre-hypertensives were significantly older ($p < 0.05$) than the normals, and the hypertensives were significantly older ($p < 0.001$) than the pre-hypertensives. Thus, the effects of aging are also reflected in the PP variations at the three arterial sites. The metabolic and biochemical factors behind age-dependent arterial stiffening are well established [192]. Stiffening of the central arteries will result in changes in both the wave reflection patterns and arrival times of the reflected waves at the measurement site [51]. This can be either burdensome, if the reflected wave adds to the main systolic pressure peak, or beneficial, if the reflected wave arrives at late systole or early diastole [193]. If the reflected wave does not augment the main systolic pressure peak, an increase in PP will not be observed, which tends to be the case in younger, more elastic arteries exhibiting lower PWV and hence lower reflection amplitudes [51]. This phenomenon is evident from the results within the pre-hypertensive group in this study – the four subjects who exhibited aortic PP > 50 mmHg were significantly older (42.0 ± 5.7 y.o.) than the five subjects with aortic PP < 50 mmHg (33.4 ± 6.9 y.o.).

Figure 5.4 depicts the non-uniformity of the PP waveform at different arterial sites. The arrival of the reflected wave caused an amplification of the PP in the normal and pre-hypertensive aortas (5.4a and 5.4b, respectively) as well as in the hypertensive radial artery (5.4c), but not in the hypertensive aorta. This appears to contradict the notion that in older, hypertensive individuals, the reflected wave tends to arrive at the ascending aorta during early systole, resulting in an even greater increase in PP [33, 194]. However, the aforementioned studies have investigated central PP using either a generalized transfer function to derive the PP at the ascending aorta [78, 150], or cardiac catheterization at the aortic root [195]. Since this study represents the first non-invasive, direct measurements of PP in the abdominal aortas of pre-hypertensive and hypertensive subjects, it is possible that in some hypertensive cases (such as the one shown in 5.4c), the arrival of the reflected wave at the abdominal aorta may not always cause pressure amplification.

In the normal and pre-hypertensive groups, no strong correlation ($r^2 < 0.45$) was observed between the aortic and peripheral PPs, while in the hypertensive group, a relatively strong correlation was observed between aortic PP and both peripheral PPs ($r^{2 =}$ 0.68 for the radial, $r^2 =$ 0.87 for the brachial). A combination of prolonged peripheral hypertension and age-related arterial stiffening may have resulted in the positive relationship between radial, brachial, and aortic PP in the hypertensive group. However, it is worth noting that two of the hypertensive subjects exhibited PPs within the normal and pre-hypertensive range at all three arterial sites despite exhibiting systolic brachial pressures > 140 mmHg. This may be attributed to the increased diastolic brachial pressure in these subjects, which can serve as its own cardiovascular risk factor [182]. The lack of correlation between aortic and peripheral PPs in the normal and pre-hypertensive groups indicates that PP elevation throughout the arterial tree may not be uniform in relatively compliant arteries. As PP rises, the increased intraluminal pressure exerts a greater force on the wall, engaging more collagen fibers and causing a reduction in arterial compliance. However, arterial compliance is also dependent on vessel size, which may also have contributed to the non-uniformity of the PP measurements at the three different sites investigated in this study.

PWUM relies on fundamental physical assumptions that are inherent to the validity of the Laplace law and the Moens–Korteweg equation used in this study. These assumptions include a cylindrical geometry and the linear elasticity of the arterial wall. The linear elasticity assumption denotes that the distension and pressure waveforms have temporal variations that are in-phase. This is a commonly accepted hypothesis [196] relying on the fact that the nonlinear behavior of the arterial wall *in vitro* starts to prevail at higher deformation than the physiological one [197]. However, it is unclear how well this translates to human arteries *in vivo*, as the nonlinear behavior of the arterial wall may infer to a more complex relationship between distension and pressure [198, 199].

Conclusions

PWUM is a technique that can be used to measure the PP in any artery accessible by ultrasound (e.g. carotid, brachial, etc.). We have chosen the abdominal aorta for all PWUM studies to date due to its clinical significance and the fact that it is impossible to directly access with other noninvasive methods such as brachial sphymomanometry or applanation tonometry. Future studies are aimed at applying the PWUM method at other imaging sites such as the carotid and brachial arteries. Such information may aid in the routine assessment and monitoring of hypertension.

Chapter 6

Pulse Wave Imaging in Carotid Artery Stenosis Human Subjects

6.1 Introduction

Atherosclerosis is a chronic vascular disease characterized by compositional changes in the arterial walls that lead to the buildup of plaque, which consists of lipids, cholesterol, calcium, and other substances found in the blood [200, 201]. The luminal narrowing associated with plaque accumulation obstructs blood flow through the artery, reducing blood supply to certain organs. Plaques may rupture and cause major cardiovascular events such as myocardial infarction or ischemic stroke [202]. Carotid stenosis is a narrowing of the lumen in the carotid artery usually caused by atherosclerosis, occluding blood flow to the brain (Figure 6.1a). A stroke may occur if the plaque ruptures and forms a blood clot (i.e. cerebral thrombosis), which may detach and become lodged upstream in the smaller vessels of the brain (i.e. cerebral embolism). Over 15 million people suffer strokes each year worldwide, resulting in ~ 5 million deaths [203]. In the U.S., stroke affects approximately 795,000 people each year and is the third leading cause of death (over 140,000 annually). An estimated 15-20% of all ischemic strokes are attributed to carotid atherosclerosis [17]. In patients exhibiting severe carotid blockage, a surgical intervention such as a carotid endarterectomy (CEA, Figure 6.1b) or carotid stenting may be performed to reduce the risk of stroke. However, current clinical criterion for assessing the risk of stroke is based on limited information. As a result, nearly 80% of the ischemic strokes attributed to carotid atherosclerosis occur in asymptomatic patients without a history of stroke or transient ischemic attacks (i.e. "mini-strokes") [17].

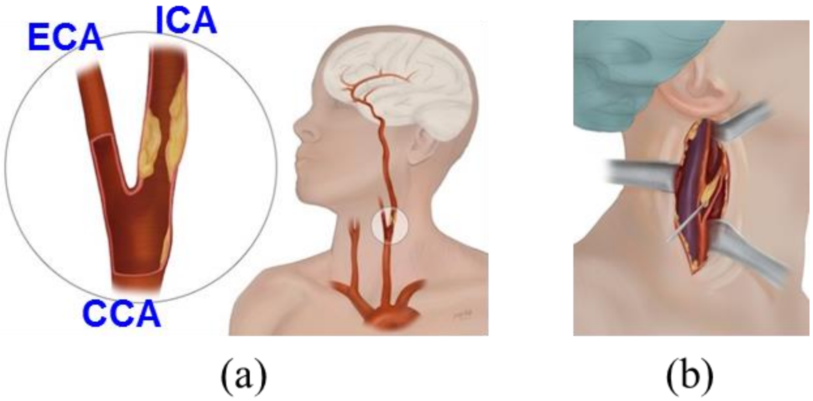

Figure 6.1: (a) Carotid artery anatomy and stenosis. The common carotid artery (CCA) bifurcates into the internal and external carotid arteries (ICA and ECA, respectively). Carotid artery stenosis is characterized by plaque buildup, typically around the carotid bifurcation. If a carotid plaque ruptures, it may cause a blood clot or travel upstream and get lodged in the small arteries in the brain, leading to a stroke. (b) In patients with severe blockage, a carotid endarterectomy may be performed to reduce the risk of stroke by surgically removing the plaque. Source: *Neurosurgeons of New Jersey*.

6.1.1 Clinical challenges in plaque detection and stroke prediction

Plaque formation and buildup may occur in the carotid arteries asymptomatically over time [204]. As a result, many cases of carotid stenosis are not discovered until the artery has been moderately to severely blocked [205]. Clinically, the risk of stroke associated with carotid atherosclerosis is assessed based on the reduction in the luminal diameter (i.e. percent stenosis), which has traditionally been measured using X-ray angiography, although less invasive methods such as duplex ultrasound, computed tomographic angiography (CTA), and/or magnetic resonance angiography (MRA) are preferred nowadays. The two largest randomized trials of carotid endarterectomy in newly symptomatic carotid stenosis are the North American Symptomatic

Endarterectomy Trial (NASCET) and the European Carotid Surgery Trial [206-208]. Both trials relied on conventional angiography to image the carotid arteries. The findings have supported intervention with CEA or stenting for symptomatic patients with severe degrees of stenosis (>70%) to reduce the risk of stroke. However, the measurement techniques used to derive percent stenosis initially differed between the trials, resulting in varying incidence of stroke and revascularization benefit due to a very different definition of 70% stenosis.

One of the most commonly used criterion for assessing the degree of stenosis using carotid duplex scanning was set forth by Taylor and Strandness from the University of Washington [209]. This is the same criterion used by the Department of Vascular Surgery at Columbia University Medical Center. Features of the spectral waveform of the blood flow such as peak systolic frequency, degree of spectral broadening, end diastolic velocity, and overall shape are used to classify the degree of stenosis into six categories – none, 1-15% diameter reduction (DR), 16-49% DR, 50-79% DR, 80-99% DR, and complete occlusion. Duplex ultrasound scanning presents several advantages over CTA and MRA such as low cost, non-ionizing radiation, speed, and portability.

Regardless of the diagnostic method, current clinical practice in North America for selecting patients for a CEA continues to rely upon the guidelines from NASCET, which are heavily based on symptomatology and the degree of stenosis [210]. However, the majority of ischemic stroke cases occur because emboli originating from a carotid plaque occlude an artery supplying the brain, not because of the luminal narrowing itself [211]. Thus, a significant diameter reduction may not always correlate with a high risk of stroke. In fact, histopathological studies have found that cerebrovascular events can also occur in patients with carotid plaques causing low-grade stenosis (<30%) and with no other identifiable cause for their stroke [212-214]. In addition, findings from NASCET also revealed that CEA in patients with symptomatic, moderate stenosis (50-69%) yielded only a mild reduction in the ipsilateral stroke rate compared to patients with the same degree of stenosis who were treated with medication [215]. For symptomatic patients with <70% stenosis and for asymptomatic patients, the degree of stenosis alone may not be a reliable measure of stroke risk [216]. Identification of patients with high-risk asymptomatic carotid plaques remains an elusive but essential step in stroke prevention.

6.1.2 Characteristics of vulnerable vs. stable plaques

There is an increasing consciousness that it is not the size of the plaque, but its composition and propensity of rupture that are related to stroke [217, 218]. Several recent investigations have demonstrated that the plaque structure and composition may represent a more direct biomarker for the development of cerebrovascular ischemic events rather than the degree of luminal stenosis [219, 220]. Thus, the early detection of carotid atherosclerotic disease and reliable identification of plaque features associated with an increased risk of rupture are crucial for stroke prevention. Atherosclerotic plaques can be broadly categorized into two types based on their highly complex composition and physical properties – vulnerable and stable [221]. Vulnerable plaques are characterized by a high propensity for rupture, while stable plaques tend to be stiffer and less prone to rupture.

Vulnerable plaques

Plaque biomarkers and features that may be indicative of a high-risk lesion for ischemic events include a disrupted luminal surface (e.g., fibrous cap rupture, ulcerations), lipid pools, intra-plaque hemorrhage, intra-plaque neovascularization, and the presence of macrophages and inflammatory cells [222-224]. The morphology of the luminal surface of carotid plaques can be classified as smooth, irregular, or ulcerated. The presence of frank ulcerations significantly increases the risk of cerebrovascular events as demonstrated in the NASCET study [208]. Unstable, vulnerable plaques are also characterized by a thin fibrous cap covering a large necrotic core containing macrophages and interstitial collagen [225]. After the fibrous cap rupture, the exposure of thrombogenic subendothelial plaque constituents to the luminal blood flow represents a critical event that eventually leads to thromboembolic complications. Intra-plaque hemorrhage is currently recognized as a high risk factor for plaque instability due to its role in plaque progression and destabilization [226]. Inflammation is another key process in plaque destabilization and the propensity of atherosclerotic lesions to cause clinical sequelae [227]. These findings have generated tremendous interest for the development of noninvasive methods that can reliably identify the morphologic features of ‘‘vulnerable plaques’’.

Stable plaques

The progression of atherosclerotic plaques is associated with structural changes. Stable plaques tend to be asymptomatic [204] and are characterized by an intact and thick fibrous cap consisting of smooth muscle cells in an extracellular matrix rich in type I and III collagen [221]. Calcification is common in late-stage atherosclerotic plaques and increases with age [228]. Apoptotic cells, the extracellular matrix, and necrotic core material may act as sites for the deposition of microscopic calcium granules, which can subsequently expand to form larger lumps and plates of calcium deposits [228]. The combination of calcium deposition and the collagen-rich matrix increase the stiffness of the plaque and contribute to its stability. Studies over the last decade have supported the view that calcification in atherosclerotic plaques is an active and presumably regulated process that exhibits similarities to new bone formation [229].

6.1.3 Imaging-based methods for plaque characterization

The development of noninvasive imaging methods for plaque characterization is aimed at detecting, quantifying, and assessing the plaque biomarkers and features that have been shown to correlate with plaque vulnerability and propensity for rupture. Noninvasive imaging methods to assess the correlation between plaque vulnerability and composition with risk of stroke have primarily been developed using MRI, CT, and ultrasound techniques. The widespread availability of multi-detector-row CT scanners has made CT angiography the most used noninvasive technique to assess carotid arteries after color-duplex ultrasound. The introduction of dual-energy CT allows for measurement of the attenuation value of a tissue at multiple energy levels.

Underhill et al [230] proposed a rapid risk stratification strategy using MRI known as the carotid atherosclerosis score (CAS), based on maximum wall thickness (WT) and the maximum lipid-rich necrotic core percentage (%LRNC). A cross-sectional study showed that the CAS was an accurate predictor for the presence of intra-plaque hemorrhage and fibrous cap rupture. In a prospective, longitudinal study, CAS was found to have a significant increasing relationship with incident disrupted luminal surface and plaque progression [216]. MRI has also been used for biological targeting of inflammation using antibody-conjugated superparamagnetic iron oxide (SPIO) particles as an MRI probe to assess inflammation in human atherosclerotic plaques [210].

Ultrasound methods include characterizing plaques based on their acoustic properties [231] and echogenicity [211]. Studies comparing plaque histology with ultrasonography have suggested that echolucent plaques have more lipid and hemorrhage and echogenic plaques more fibrous tissue [232]. A significant association between echolucent plaque and internal carotid artery occlusion has also been shown [211]. ARFI imaging has been used to assess arterial elasticity [233, 234] and characterize carotid plaques [117, 235, 236] by estimating the displacements induced at sequentially interrogated radiation force excitation locations. However, modeling studies have shown that ARFI displacements are susceptible to underestimation of up to ~ 50% of the true induced motion [237] due to lateral and elevational shearing that occurs within the region of excitation. The gradient of the acoustic radiation pulse-induced force causes non-uniform scatter movement under the tracking point spread function, resulting in shearing decorrelation and final displacement estimates that do not reflect the full extent of tissue motion. This underestimation was also observed in phantom studies, where the maximum underestimation error was found to be 35% [238]. Thus, ARFI imaging has generally been limited to qualitative and relative assessment of tissue elasticity.

6.2 Methods: Pulse Wave Imaging of stenotic carotid arteries

The majority of research on imaging-based methods to assess plaque properties focuses on identifying features from a single image rather than investigating the changes in vascular dynamics associated with different types of plaques. The ability of PWI to capture the arterial wall motion may offer new insights into how arterial function is affected by plaques of various composition, size, and location. The PWV in a stenotic carotid segment as well as the pulse wave-induced displacements themselves may be useful in detecting and characterizing plaque regions. Thus, the purpose of this study is to apply the PWI method in patients with carotid atherosclerosis and investigate the effects of stenosis on pulse wave behavior. Before describing the study design, several extensions of the PWI method for the imaging of stenotic carotid arteries will be introduced.

The feasibility of PWI in the carotid artery has been demonstrated in young, healthy subjects [118]. PWV measurements at a segment of the left CCA away from the bifurcation in 8 male volunteers ranged from 4.0 – 5.2 m/s. Similar values were reported in Chapter 3 of this dissertation, where the carotid arteries of young healthy subjects were scanned to determine the most reliable waveform tracking feature for PWI *in vivo*. In addition, the arterial wall displacements themselves have been used to derive the stress-strain relationship *in vivo*, demonstrating the complex mechanical interaction of the different wall constituents [130].

As discussed in Chapter 3, a tradeoff between temporal and spatial resolution exists in conventional ultrasound. In order to achieve the high frame rates necessary for reliable PWV estimation, the number of scan lines must be reduced to 24-48, resulting in beamwidths of ~ 0.79 - 1.58 mm using a linear array transducer. This level of resolution is sufficient for visualizing normal carotid arteries due to their simple geometry and the high-intensity echoes that reflect from the arterial walls. However, in stenotic arteries, high-resolution imaging is important for identification and segmentation of atherosclerotic regions as well as visual assessment of plaque features. Thus, rather than acquiring images using a fixed number of scan lines as in Chapters 4 and 5, the image acquisition sequence for PWI in carotid arteries was modified to acquire one high-resolution (256 scan lines) reference frame immediately preceding a 2-second RF acquisition using 32 scan lines. The reference frame was used for manual segmentation of the arterial walls and plaque regions, while motion estimation was performed using the lower line density RF frames from the second acquisition. Subsequent studies also employed plane wave imaging to achieve both a high temporal and spatial resolution, which will be described in Section 6.2.3.

6.2.1 Piece-wise PWI for regional PWV and modulus mapping

In Chapters 3-5, a single PWV was measured via linear regression across the entire imaged arterial segment. However, the presence of plaques may induce wave reflections and flow disturbances within the segment, changing the regional wave propagation behavior [239]. In order to investigate these changes, an increased resolution of the PWV estimation is required.

Piece-wise PWI entails sliding a fixed-length overlapping kernel along the spatio-temporal map and performing linear regression on only the waveform arrival times within the kernel, thus generating a series of PWV estimates along the imaged segment. Consider the normal carotid artery from a healthy 27-y.o. male in Figure 6.2. The pulse-wave induced wall displacements were estimated using 32-scan line RF data and linearly interpolated so they could be overlaid onto the B-mode image reconstructed from the 256-scan line reference frame (a-c). Manual segmentation and automated tracking of the inner and outer layers of both walls (blue lines in d) allow for measurement of the inner diameter and the anterior wall thickness over time. The regional PWV is estimated using linear regression on all the 50% upstroke markers from the spatio-temporal map (e), while piece-wise PWV estimation uses an overlapping kernel to generate multiple values along the imaged segment (f). In this study, the kernel length was fixed at 20% of the imaging width and shifted by one point at a time. The piece-wise PWV measurements can then be color-coded and overlaid onto the reference B-mode frame for visualization of the PWV at different points along the artery (g).

Although the PWV is known to correlate with arterial stiffness, direct indices of arterial stiffness (i.e. modulus or compliance) are also affected by geometrical parameters such as diameter and thickness [130, 240, 241], which were measured from the PWI images. The modified Moens-Korteweg equation [29, 184, 185] was used derive the modulus of the normal controls and each plaque region:

$$Modulus = \frac{D\rho\left(1-\nu^2\right)(PWV)^2}{h} \qquad [1]$$

where D is the diameter (measured at each scan line position), ν is the Poisson's ratio (~ 0.49999 for soft tissues), and ρ is the fluid density of blood (~1060 kg/m^3). The Bramwell-Hill model [241] proposed a series of substitutions relevant to the observable hemodynamic measures, and was used to derive the compliance of the normal controls and each plaque region:

$$Compliance = \frac{\pi\left(\frac{D}{2}\right)^2}{(\rho)(PWV)^2} \qquad [2]$$

Since the diameter (D) and thickness (h) are changing throughout the cardiac cycle [242], all modulus and compliance calculations in this study were performed using the maximum diameter and its associated thickness. This corresponds to the peak systole phase of the cardiac cycle and represents the maximally distended artery, which is physiologically relevant for cardiovascular function analysis [243, 244].

In the normal case shown, the PWV (6.2g) and modulus (6.2h) along the imaged segment remain within a narrow range of ~ 2-3 m/s and ~ 30-50 kPa, respectively. In atherosclerotic carotid arteries with altered wall dynamics, piece-wise PWV and modulus mapping may reveal more drastic variations in the arterial properties based on the wave propagation around and possibly through the plaque. In addition, PWI can also map the cumulative displacements within the anterior wall (i) by summing the inter-frame displacements at each pixel over the cardiac cycle. In the context of this chapter, the maximum cumulative displacement over the cardiac cycle (representing the point of maximum distension) will be assessed. Cumulative displacement estimation in stenotic carotid arteries will be further discussed in Section 6.2.3.

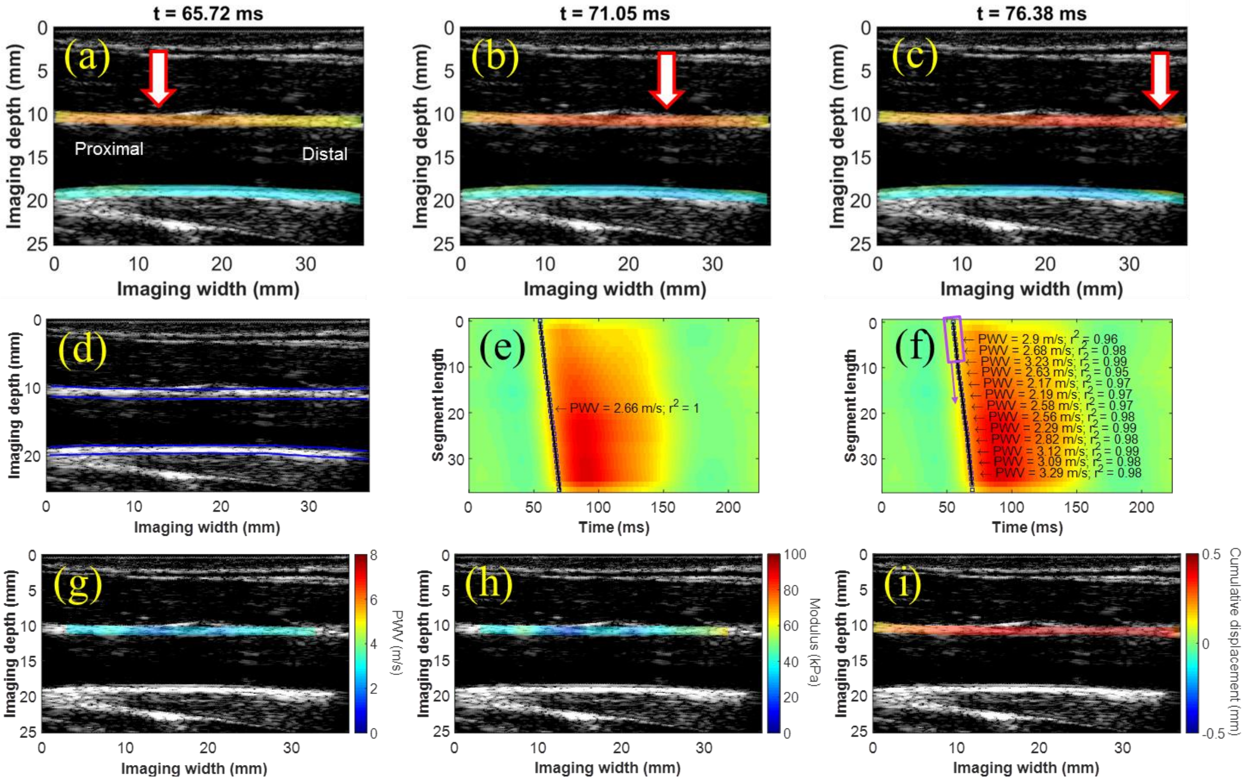
t = 65.72 ms
t = 71.05 ms
t = 76.38 ms
(a)
(b)
(c)
Proximal
Distal
Imaging depth (mm)
Imaging width (mm)
(d)
(e)
(f)
Segment length
Time (ms)
PWV = 2.66 m/s; $r^2 = 1$
PWV = 2.9 m/s; $r^2 = 0.96$
PWV = 2.68 m/s; $r^2 = 0.98$
PWV = 3.23 m/s; $r^2 = 0.99$
PWV = 2.63 m/s; $r^2 = 0.95$
PWV = 2.17 m/s; $r^2 = 0.97$
PWV = 2.19 m/s; $r^2 = 0.97$
PWV = 2.58 m/s; $r^2 = 0.97$
PWV = 2.56 m/s; $r^2 = 0.98$
PWV = 2.29 m/s; $r^2 = 0.99$
PWV = 2.82 m/s; $r^2 = 0.98$
PWV = 3.12 m/s; $r^2 = 0.99$
PWV = 3.09 m/s; $r^2 = 0.98$
PWV = 3.29 m/s; $r^2 = 0.98$
(g)
(h)
(i)
PWV (m/s)
Modulus (kPa)
Cumulative displacement (mm)

Figure 6.2: (a-c) Consecutive PWI frames showing pulse wave propagation along the anterior wall of a normal common carotid artery (M, 27 y.o.). (d) Manual segmentation and automated tracking of the inner and outer layers of the walls allow for measurement of the anterior wall thickness and inner diameter at each scan line position over time. Regional PWV estimation (e) generates a single PWV estimate across the imaged segment, while a piece-wise kernel outputs an array of PWV measurements that can be color-coded and overlaid onto the B-mode (g). (h) The incremental modulus along the artery can be derived based on the Modified Moens-Korteweg equation using the diameter, thickness, and PWV value at each scan line position. (i) The maximum cumulative displacement at each pixel in the anterior wall is computed by summing the inter-frame displacements from the beginning of the waveform upstroke (i.e. end diastole) to the point of maximum distension (i.e. peak systole), shown in Figure 6.3.

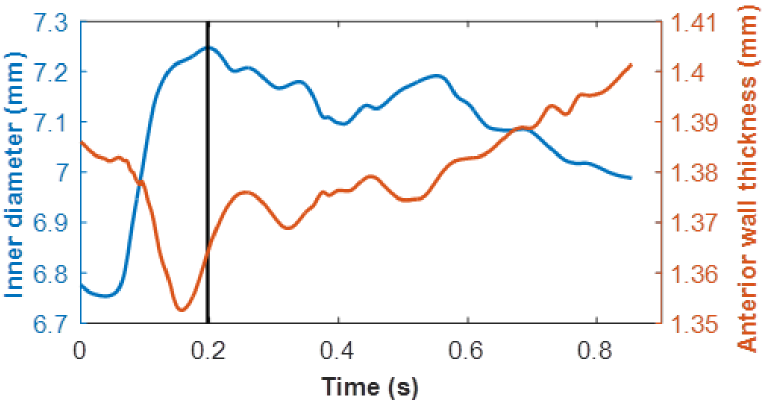

Figure 6.3: Diameter (blue curve) and anterior wall thickness (brown curve) variation over the cardiac cycle at the central scan line position in the normal carotid artery shown in Figure 6.2, obtained by tracking the inner and outer layers of the walls over time. As the artery dilates to accommodate the increase in blood volume during systole, the sudden rise in intra-luminal pressure causes the wall to compress, decreasing the wall thickness. All modulus calculations were performed using the maximum diameter and associated anterior wall thickness (black line), thus representing the stiffness of the maximally distended artery.

6.2.2 Intra-plaque PWV and modulus mapping using plane wave ultrasound

The methods for PWV and modulus mapping described in Section 6.2.1 were based on the spatio-temporal map obtained from a single trace through the artery wall. For the assessment of plaque composition, it may be useful to map the PWV and modulus at different depths within the plaque. This may potentially reveal information about intra-plaque properties such as calcified inclusions and/or lipid pools based on the hypothesis that the spatio-temporal map from different depths may be altered by the heterogeneity of certain plaque regions. However, the limited spatial resolution of the conventional ultrasound imaging sequences previously used for PWI may be insufficient to generate detailed maps of intra-plaque PWV and modulus.

Plane wave imaging, as described in Section 2.1.2, allows for the acquisition of an entire image frame from only one transmit event, which increases the frame rate at the expense of image quality due to the increased scattering of the reflected echoes. To overcome this limitation, several tilted plane waves at different transmission angles may be used and coherently compounded [92] to increase the image quality. Software-based beamforming techniques can then be used [132, 245] to reconstruct as many scan lines as desired.

In this chapter, the initial feasibility of PWV and modulus mapping in stenotic carotid arteries at a single depth through the plaque region(s) was demonstrated using conventional ultrasound imaging sequences on the SonixTouch scanner with 32 scan lines at imaging depths of 3-4 cm, resulting in frame rates of around 500 Hz. For intra-plaque PWV and modulus mapping, a Verasonics V1 or Vantage scanner (Verasonics, Inc., Kirkland, WA, USA) was used for plane wave image acquisition at the same depths. 0-5 compounding angles were employed, and an adapted delay-and-sum beamforming algorithm was used to reconstruct 128 scan lines [92], resulting in frame rates of 1600-2000 Hz. The inner and outer layers of the arterial walls were manually segmented in the first frame of the imaging sequence as in Figure 6.2d, thus accounting for the reduced diameter and increased thickness in plaque regions along the artery. Multiple wall traces (and hence spatio-temporal maps) were automatically generated in between the layers, and the piece-wise PWV and modulus measurements obtained from each spatio-temporal map were overlaid onto the B-mode reference frame, forming an image of the PWV and modulus at different depths within the plaque region(s).

6.2.3 Intra-plaque cumulative displacement and strain mapping

The maximum cumulative displacement can be computed within any user-defined region of interest (ROI) on the ultrasound image, such as a plaque or a segment of the normal carotid wall (Figure 6.2i). The same methods used for automated wall tracking based on the inter-frame displacements can be applied to track each pixel of the ROI in the axial direction across the entire sequence of images (Figure 6.4). By summing the inter-frame displacements to obtain the cumulative displacements within the ROI at peak systole, the stiffness contrast may be detected along the imaged segment. We expect stiff, calcified plaques to displace less than normal segments of the carotid artery as well as softer, lipid-rich plaques.

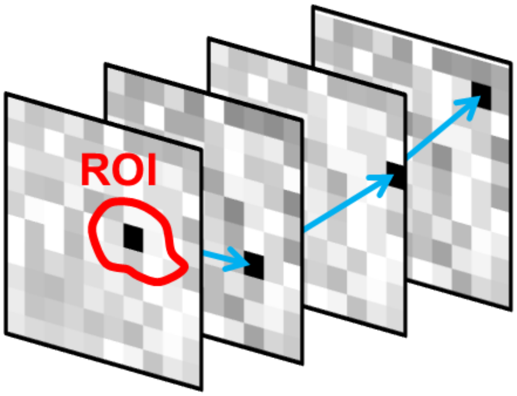

Figure 6.4: 1D cumulative displacement estimation is performed within a region of interest (ROI) by summing the inter-frame displacements that are used to track each pixel in the axial direction over time.

The cumulative displacements may not vary much within the plaque, which is a solid structure attached the pulsating wall. However, computing the spatial gradient of the cumulative displacement map to yield cumulative strains provides a new level of information regarding tissue elastic properties that is an active field of research in ultrasound imaging [246]. In the context of ultrasound elasticity imaging, strain represents the deformation of soft tissue in response to an external force [247], such as the intra-luminal pressure of a pulsating artery acting on the walls in the radial direction. When this force deforms a medium such as a heterogeneous plaque, stiffer [softer] regions in the medium are expected to experience a lower [higher] level of strain.

Strain estimation using ultrasound has exhibited great promise for clinical integration due to its non-invasiveness, low cost, and ease of use. 2D (i.e. both axial and lateral) strain estimation techniques have been developed by our lab for cardiac imaging applications such as myocardial elastography [109, 110, 248] and mapping of the electromechanical wave [249]. In a longitudinal view of the carotid artery, displacement primarily occurs in the axial direction. The 1D axial strain within a ROI can be obtained using a least-squares strain estimator [149] to compute the spatial gradient of the 1D cumulative displacements. Negative strains indicate tissue compression, while positive strains indicate tissue elongation. 1D ultrasound strain imaging has been attempted in carotid plaques [250], demonstrating both the feasibility and limitations of using peak systolic cumulative strains for plaque characterization.

One of the key considerations for robust strain estimation is the size of the strain kernel, which must be small enough to operate within the structure of interest, but large enough to ensure an adequate strain SNR [251]. This is why strain estimation in a thin structure such as the normal carotid artery wall typically yields extremely noisy results. However, the increased thickness in atherosclerotic regions allows for the use of larger strain kernels to achieve higher SNR. In this chapter, intra-plaque strains were computed using the least-squares strain estimator and a strain kernel that was half the mean thickness of the plaque region. The cumulative strain corresponding to the point of maximum cumulative displacement was obtained for each pixel in the plaque ROI. In this way, intra-plaque properties may also be investigated by estimating the deformation of plaque components induced by the arterial pulsation.

6.3 Methods: Study Design

6.3.1 *In vivo* study in carotid stenosis patients

All imaging procedures were approved by the Institutional Review Board of Columbia University Medical Center. N = 11 patients (9 M, 2 F, mean age 76.00 ± 8.51 y.o.) diagnosed with moderate (> 50%) to high-grade (> 80%) carotid stenosis were recruited from the outpatient clinics in the Departments of Vascular Surgery and Neurological Surgery. RF signals were acquired using conventional and/or plane wave ultrasound (as described in Section 6.2.2) at a carotid segment showing a clear atherosclerotic lesion on the B-mode image. In all patients, imaging was performed at either the carotid bifurcation or the CCA segment immediately below the bifurcation. All imaging views contained both a plaque region and a normal carotid segment. In cases where the pulse wave-induced displacement of a very stiff plaque could not be detected, the PWV through the plaque was estimated using the arrival times in the normal segments before and after the plaque.

The echogenicity and acoustic shadowing on the B-mode image serves as a crude criterion for identifying different types of plaques. In general, calcified plaques give the most intensive echoes and attenuate the ultrasound signal distal to the plaque, causing significant acoustic shadowing [252]. Lipid-laden plaques are frequently represented as echolucent lesions and may present an echogenic border at the lumen-intima interface corresponding to the fibrous cap [253]. A fibrous plaque may be depicted as a mixture of echolucent lipidic atheromas and highly echoreflective calcific lesions [253]. In each of the atherosclerotic carotid arteries imaged, the degree of calcification in the plaque region was graded based on visual assessment of the echogenicity and the severity of acoustic shadowing on the B-mode image. In patients for whom prior CTA scans were available, the image intensity of the plaque region(s) were also visually assessed for confirmation of the degree of calcification, since calcified plaques show up as regions of very high brightness on the CTA. However, beam-hardening and blooming artifacts have made it difficult to accurately assess the degree of luminal narrowing by CTA in the presence of heavily calcified plaques [254].

The right and left CCAs of N = 5 healthy subjects (3 M, 2 F, mean age 43.80 ± 7.17 y.o.) were also imaged as a control group, resulting in N = 10 normal arteries. Imaging was performed at the CCA segment immediately before the carotid bifurcation to be consistent with the scanning location in the stenosis patients.

6.3.2 Patients undergoing carotid endarterectomy (CEA)

Five (N = 5) of the patients exhibiting high-grade stenosis were scheduled to undergo a CEA, which presented a unique opportunity to correlate PWI findings with the disease state. In these patients, imaging was performed one hour to one week prior to the scheduled operation. Following surgery, the resected atherosclerotic tissue from the imaging location (either the common carotid or the bifurcation) was collected for gross examination and H&E staining using a standard protocol. The resected specimen was successfully retrieved from 4 of the CEA patients, 3 of which will be shown in the Results section.

6.3.3 Quantitative measurements

The methods for PWV, modulus, displacement, and strain mapping described in Sections 6.2.1 – 6.2.3 allow for several image-guided measurements to be obtained. The following parameters were measured:

- *Mean cumulative displacement (mm^2) and absolute value of the strain (%) in a region of the normal carotid wall*
- *PWV (m/s), diameter (mm), thickness (mm), and modulus (kPa) of a normal carotid segment*
- *Compliance of the normal wall (in the control group) and each plaque region (in the stenosis group)*
- *Percent stenosis (i.e. the greatest percent decrease in the inner diameter at the plaque region compared to the inner diameter of a normal wall segment)* - only measured in cases where imaging was performed in the CCA

- *Mean cumulative displacement and absolute value of the strain in the plaque ROI*
- *Percent change in cumulative displacement and absolute value of the strain between the plaque ROI and a region of the normal wall* – a negative value suggests that the plaque displaced less or experienced lower strain than the normal wall
- *PWV through the plaque region at a single depth*
- *Modulus through the plaque region at a single depth* - since the bifurcation presents a complex geometry that violates the straight, cylindrical vessel assumption of the Moens-Korteweg equation, quantitative modulus results will not be reported. However, modulus measurements were used in conjunction with piece-wise PWI for mapping of the modulus across stenosis arterial segments.

6.4 Results

6.4.1 PWV, modulus, and cumulative displacement maps

The PWI results from a CCA exhibiting 50-79% stenosis (F, 70 y.o.) are shown in Figure 6.5. The atherosclerotic region consists of overlapping bilateral lesions through which the pulse wave propagates (a-c). The large acoustic shadow (pink arrow in a) indicates that the plaque located on the far wall is highly calcified. Since PWI utilizes the anterior wall displacements for PWV estimation, the plaque attached to the near wall was defined as the ROI (red contour in d). The spatio-temporal map (e) was obtained from the trace at a single depth through the normal wall and the plaque region. In cases like these where the pulse wave-induced displacement in the plaque ROI (represented by the dashed lines in e) was absent, PWV estimation was performed using the 50% upstroke markers before and after the plaque. That is, even though the wave was not tracked through the plaque, the PWV could still be estimated. The PWV and r^2 across the entire imaged segment (e) were similar to those of the normal carotid in Figure 6.2e, while the piece-wise kernel (f) revealed the variations in PWV and r^2 along the segment. More specifically, regions of high PWV (~ 6 m/s) and modulus (~ 100 kPa), indicated by the red arrows in (g) and (h), were observed immediately preceding and following the plaque, while the plaque itself was depicted as a region of low PWV (1-2 m/s) and modulus (10-20 kPa). The cumulative displacement map revealed very low pulse wave-induced displacement within the plaque region and in the normal segment following it.

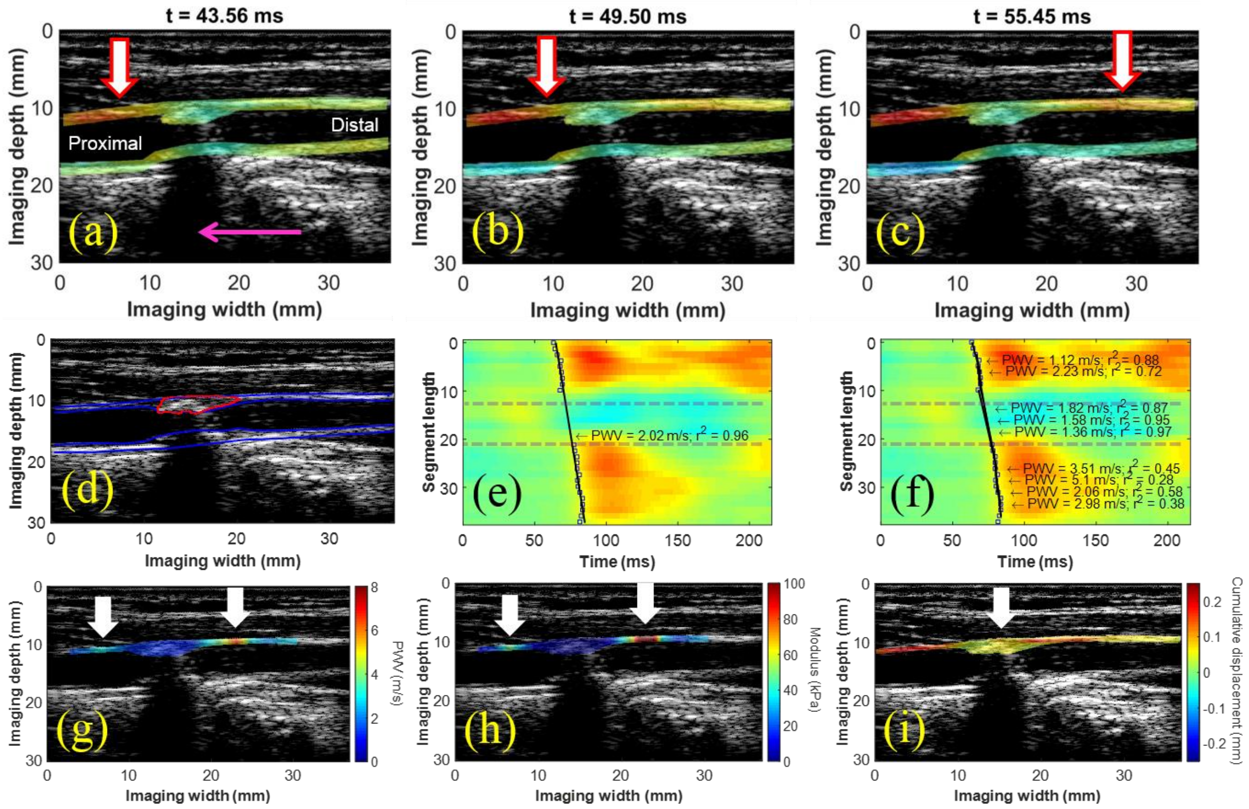

t = 43.56 ms
t = 49.50 ms
t = 55.45 ms
Proximal
Distal
(a)
(b)
(c)
(d)
(e)
(f)
(g)
(h)
(i)
Imaging depth (mm)
Imaging width (mm)
Segment length
Time (ms)
PWV = 2.02 m/s; r2 = 0.96
PWV = 1.12 m/s; r2 = 0.88
PWV = 2.23 m/s; r2 = 0.72
PWV = 1.82 m/s; r2 = 0.87
PWV = 1.58 m/s; r2 = 0.95
PWV = 1.36 m/s; r2 = 0.97
PWV = 3.51 m/s; r2 = 0.45
PWV = 5.1 m/s; r2 = 0.28
PWV = 2.06 m/s; r2 = 0.58
PWV = 2.98 m/s; r2 = 0.38
PWV (m/s)
Modulus (kPa)
Cumulative displacement (mm)

Figure 6.5: (a-c) Consecutive PWI frames showing pulse wave propagation along the anterior wall of a stenotic common carotid artery (F, 70 y.o.) exhibiting a bilateral plaque region. (d) Manual segmentation of the inner and outer layers of both walls (blue lines) accounted for the decrease in diameter and increase in thickness at the anterior wall plaque region, indicated by the red contour. (e) The spatio-temporal map from a single wall trace shows an absence of pulse wave-induced displacements in the plaque region

(dashed lines). Regional PWV estimation (e) yielded a PWV and r^2 similar to those in the normal case in Figure 6.2, while the piece-wise measurements (f) revealed regions of high PWV and modulus immediately preceding and following the plaque (white arrows in g and h, respectively). (i) Decreased pulse wave-induced displacement within the plaque region and in the normal segment following it were observed on the cumulative displacement map.

Figure 6.6 shows the variation in diameter and anterior wall thickness over the cardiac cycle for the patient in Figure 6.5. The curves in (a) are from a point in the normal wall preceding the plaque, and the curves in (b) are from a point within the plaque ROI. In the normal wall, the thickness decreases as the diameter increases, just like in the normal case shown in Figure 6.3, although the distension and rate of thickness decrease are both lower in the stenotic case, suggesting increased stiffness. The point of maximum distension (i.e. greatest diameter), indicated by the black line in (a) and (b), does not occur at the same point in the cardiac cycle for the normal wall and plaque region. This phenomenon will be further discussed in Section 6.5.

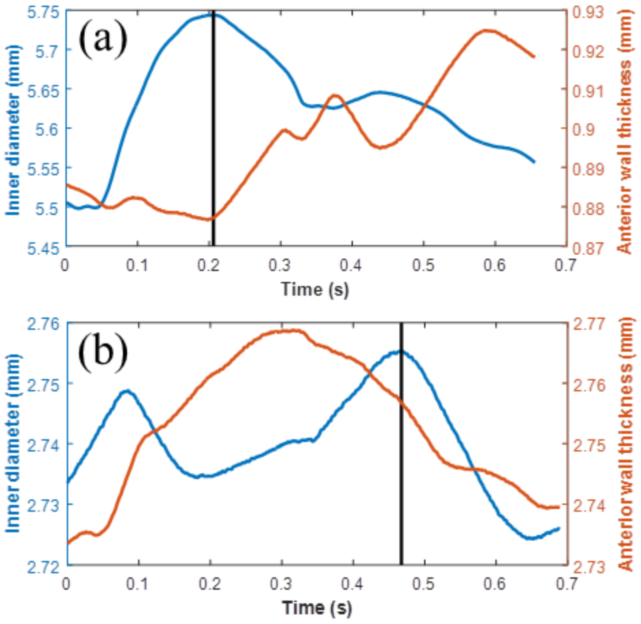

Figure 6.6: Diameter (blue curve) and anterior wall thickness (brown curve) variation over the cardiac cycle in the stenosis case from Figure 6.5 at (a) a point in the normal wall preceding the plaque, and (b) a point within the plaque. The black line indicates maximum distension (i.e. greatest diameter), which does not occur at the same point in the cardiac cycle for the normal wall and the stenotic region.

Figure 6.7 presents a case (F, 72 y.o.) in which plaques exist on both the anterior and posterior walls (white arrows in a). The plaque of interest (red contour) was chosen due to its location on the anterior wall and the presence of normal segments around it, allowing the PWV to be mapped through the plaque. Decreased cumulative displacements were observed in the plaques located on the anterior wall (white arrows in b). The piece-wise PWV map (c) shows a region where the PWV transitions from positive to negative as if two waves traveling in opposite directions is converging within the plaque (white arrow). This is an interesting phenomenon that was also observed in other cases and may serve as a biomarker for plaque characterization. Since the Moens-Korteweg equation relates the modulus to the square of the PWV, negative PWVs will still result in positive modulus values. The modulus map (d) indicates that the plaque is much softer than the normal segment following it.

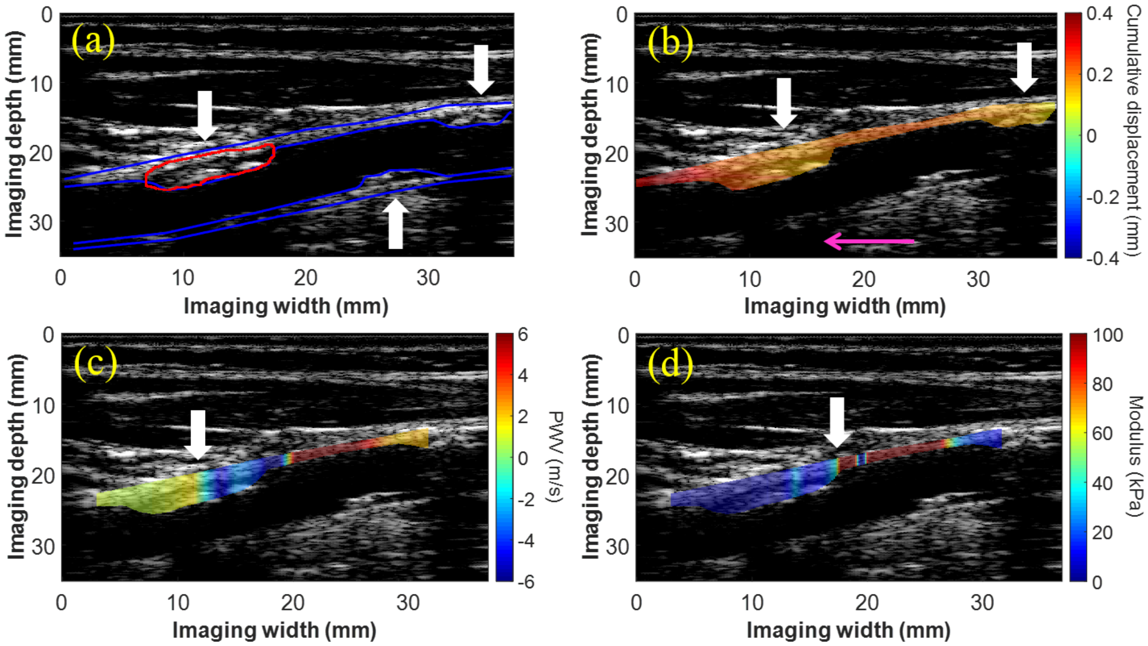
(a)
Imaging depth (mm)
0
10
20
30
Imaging width (mm)
0
10
20
30
(b)
Imaging depth (mm)
Imaging width (mm)
0.4
0.2
0
-0.2
-0.4
Cumulative displacement (mm)
(c)
Imaging depth (mm)
Imaging width (mm)
6
4
2
0
-2
-4
-6
PWV (m/s)
(d)
Imaging depth (mm)
Imaging width (mm)
100
80
60
40
20
0
Modulus (kPa)

Figure 6.7: (a) B-Mode from the right CCA of a 72-y.o. female (50-79% stenosis) containing atherosclerotic lesions on both the anterior and posterior walls (white arrows). (b) Decreased cumulative displacement was observed in the anterior wall plaques (white arrows). The presence of the acoustic shadow (pink arrow) obstructing a portion of the posterior wall suggests that the plaque directly above is moderately calcified. (c) The PWV map reveals a region where the wave appears to converge inside the plaque. (d) The modulus map shows a transition from soft to stiff between the plaque and the normal segment (white arrow).

The bilateral plaque case in Figure 6.8 (M, 76 y.o., 50-79% stenosis) was imaged using a conventional imaging sequence (32 scan lines, 505 FPS) and a plane wave sequence (no compounding, 128 scan lines, 2000 FPS) 6 months later. The B-mode is very similar to the case in Figure 6.6, showing an acoustic shadow (pink arrow) beneath the posterior wall plaque, whose appearance resembles that of a calcified fibrous cap. Both displacement maps (b and f) reveal decreased displacement in the plaque region (red contours in a and e). Similar to the case in Figure

6.7, both PWV maps (c and g) contain a point where the wave appears to converge (white arrow), however this occurs before the plaque for the conventional sequence and after the plaque for the plane wave sequence. Since the two PWV maps were generated using two different systems 6 months apart, this may be attributed to a variety of factors that will be discussed in Section 6.5. The difference in point of convergence does not change the modulus maps (d and h), as both depict the plaque as much softer than the normal wall preceding it.

Figure 6.9 shows the same set of results (B-mode, displacement map, PWV map, and modulus map) for a stenotic CCA (M, 56 y.o.) where conventional (b) and plane wave imaging with no compounding (c) were performed on the same day. The CTA image from a prior exam was obtained for comparison (a). Two plaque regions (labeled 1 and 2 in a-c), both causing an acoustic shadow (pink arrows in c), were observed on the anterior wall. The plaque located closer to the bifurcation (#2) exhibited a larger shadow and shows up as a higher-intensity brightness region on the CTA, confirming the greater degree of calcification and stiffness that translated to lower displacement amplitude (white arrow in d and e). The PWV (f and g) and modulus maps (h and i) obtained using the two different systems were highly correlated, both showing a region of high PWV and modulus immediately preceding the plaque (white arrows).

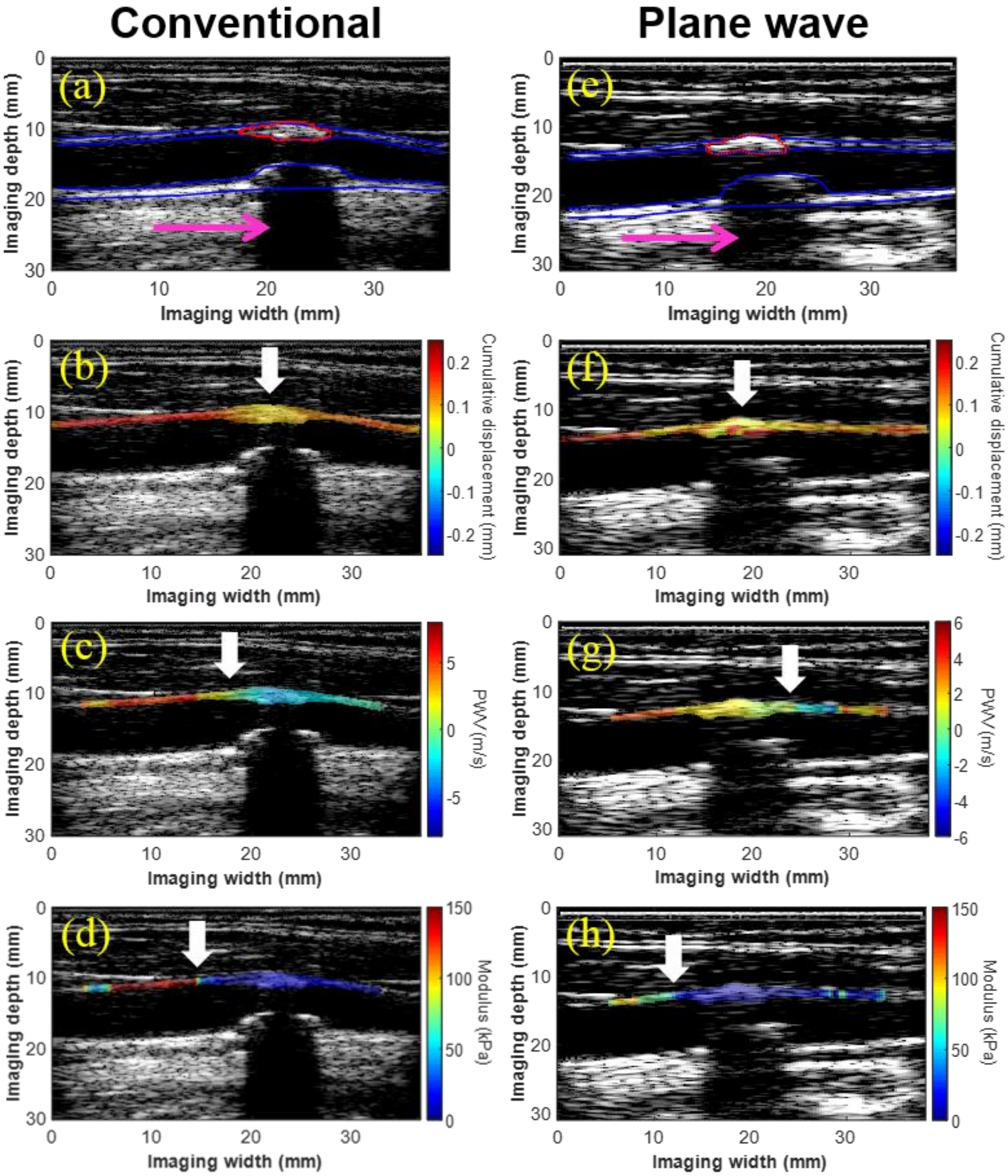
Conventional
Plane wave
(a)
(b)
(c)
(d)
(e)
(f)
(g)
(h)
Imaging depth (mm)
Imaging width (mm)
Cumulative displacement (mm)
PWV (m/s)
Modulus (kPa)

Figure 6.8: (a) B-mode image, (b) displacement map, (c) PWV map, and (d) modulus map from the right CCA of a 76-y.o. male obtained using a conventional ultrasound sequence. The pink arrow points to the acoustic shadow caused by the calcified posterior wall plaque, and the white arrows indicate regions of decreased displacement, pulse wave convergence, and a transition in modulus. The same location was scanned again during a 6-month follow up using a plane wave sequence (e-h), and similar results were observed.

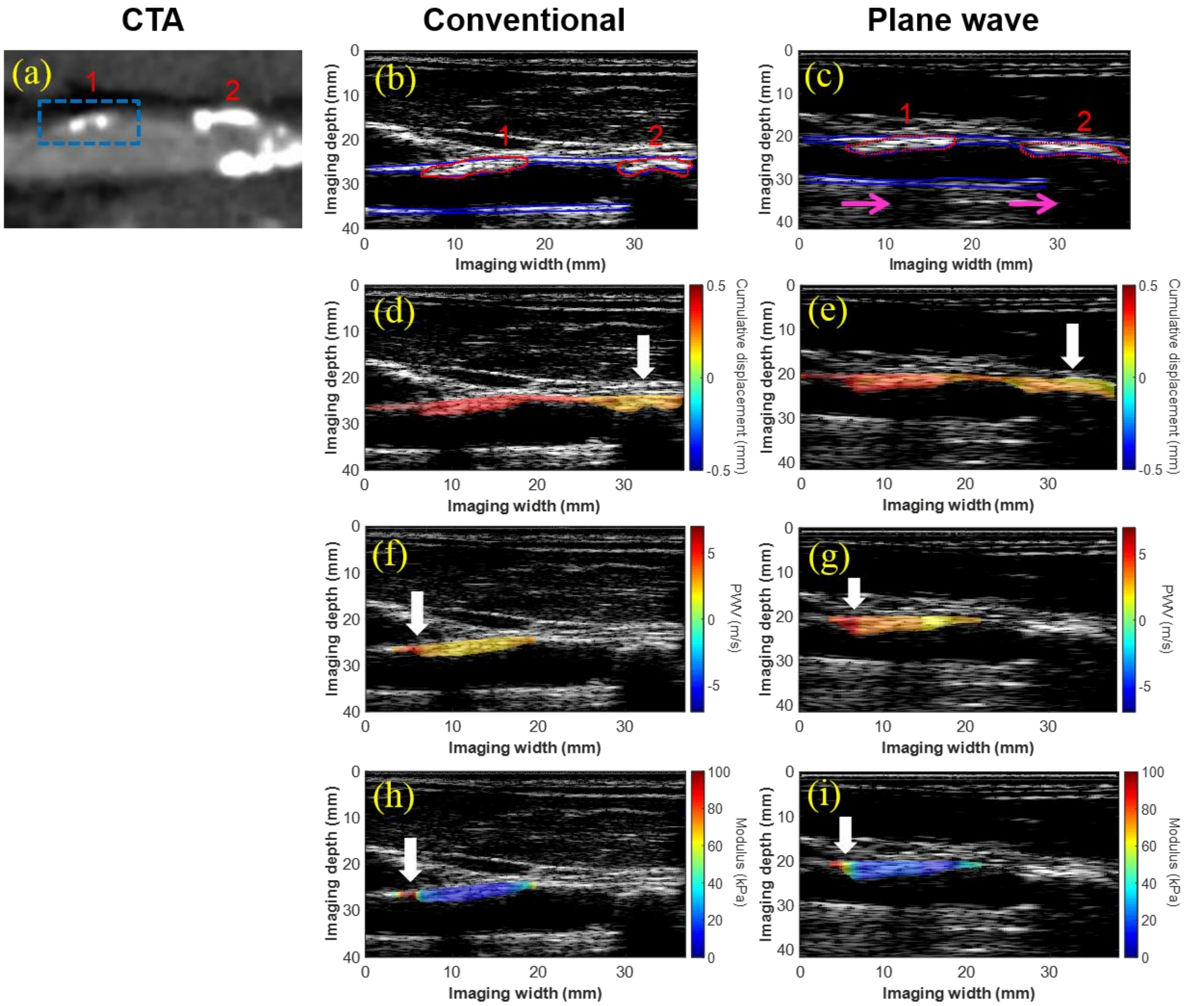
CTA
Conventional
Plane wave
(a)
1
2
(b)
(c)
(d)
(e)
(f)
(g)
(h)
(i)
Imaging depth (mm)
Imaging width (mm)
Cumulative displacement (mm)
PWV (m/s)
Modulus (kPa)
0
10
20
30
40
0.5
-0.5
5
-5
100
80
60
40
20

Figure 6.9: (a) CTA longitudinal cross-section of the right CCA in a 56-y.o. male taken 2 weeks prior to ultrasound imaging, which was performed using both a conventional sequence (b, d, f, h) and a plane wave sequence (c, e, g, i) on the same day. Two plaque regions on the anterior wall can be identified (labeled 1 and 2 in a-c), both causing acoustic shadows on the B-mode image (pink arrows in c). The displacement, PWV, and modulus maps (d-i) obtained using the two sequences provided very similar results. The white arrows indicate regions of decreased displacement, increased PWV, and increased modulus. The greater degree of calcification in plaque #2 is reflected by its larger acoustic shadow (c), higher brightness intensity on the CTA (a), and lower displacement (d, e). PWV and modulus maps were only computed for plaque #1 due to the lack of wave propagation through plaque #2.

6.4.2 Intra-plaque displacement, strain, PWV, and modulus maps

The intra-plaque mapping results for plaque #1 in the patient from Figure 6.9 are shown in Figure 6.10.

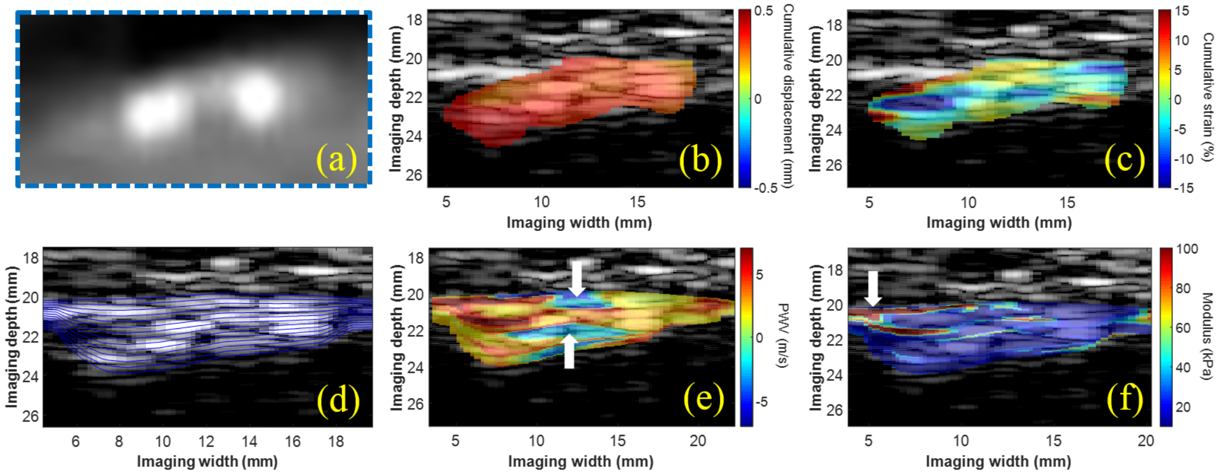
(a)
(b)
(c)
(d)
(e)
(f)
Imaging depth (mm)
Imaging width (mm)
18
20
22
24
26
5
10
15
20
6
8
10
12
14
16
18
Cumulative displacement (mm)
0.5
0
-0.5
Cumulative strain (%)
15
10
5
0
-5
-10
-15
PWV (m/s)
5
0
-5
Modulus (kPa)
100
80
60
40
20

Figure 6.10: (a) Enlarged view of plaque #1 from the CTA in Figure 6.9a. The intra-plaque cumulative displacements (b) appeared uniformly distributed within the plaque ROI, while regions of tissue compression (blue) and elongation (red) were observed on the cumulative strain map. (d) Multiple wall traces were generated for intra-plaque PWV and modulus mapping. The PWV map (e) shows regions of negative PWV (white arrows) in between regions of positive PWV that appear to correlate with the two calcified inclusions observed on the enlarged CTA image (a). The modulus map (f) appeared mostly uniform with a small region of increased modulus immediately before the plaque (white arrow).

The CTA and intra-plaque mapping results from the right CCA of a 79-y.o. male undergoing CEA are shown in Figure 6.11. Although the patient exhibited 80-99% stenosis at the bifurcation (indicated by the high-intensity brightness regions on the CTA), ultrasound imaging was performed to capture the plaques in the CCA (blue box in a) due to its simpler geometry. Two calcified inclusions were observed in this region (white arrows in a) and confirmed by H&E staining of the resected CCA segment (c, d).

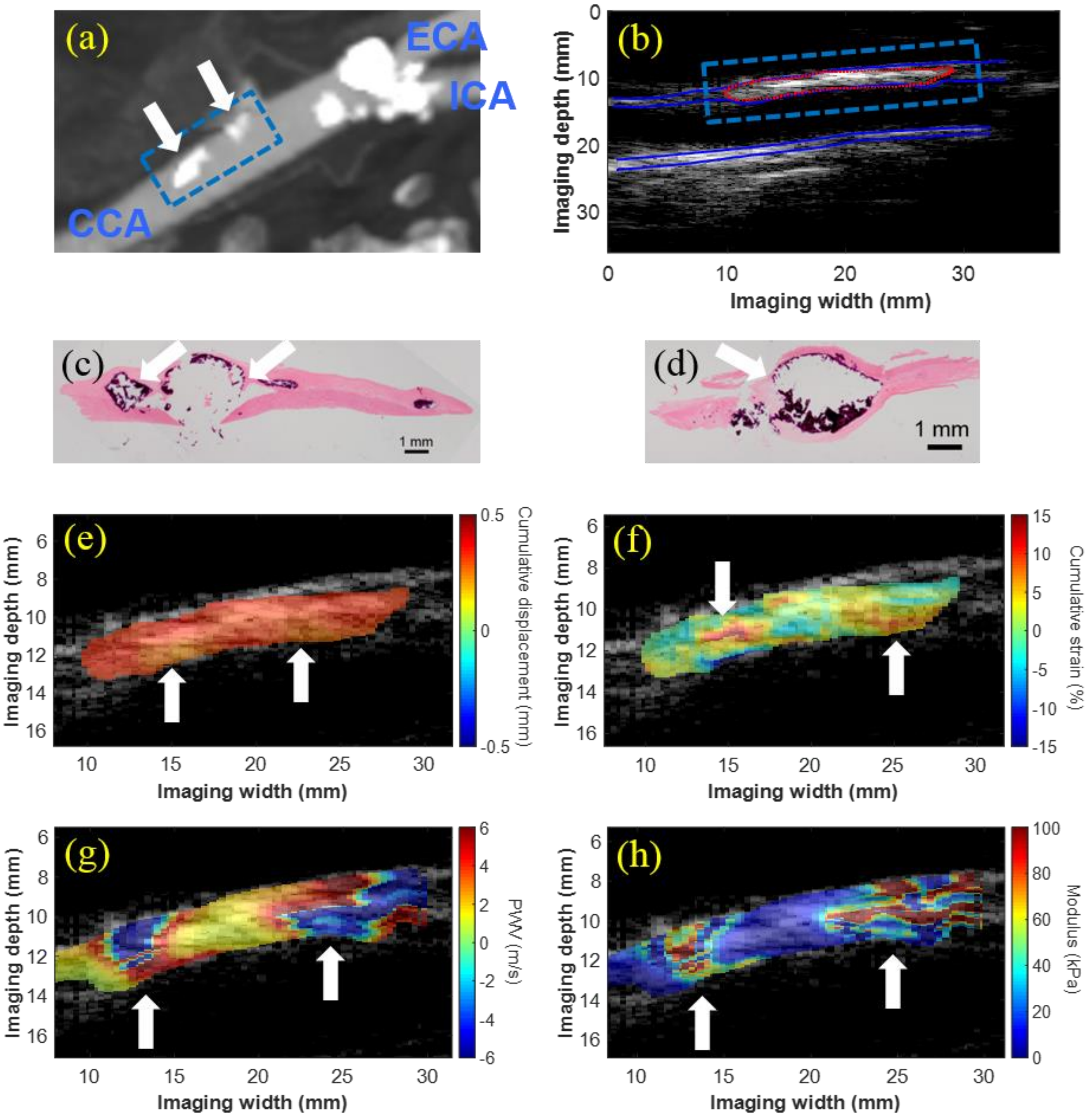
(a)
ECA
ICA
CCA
(b)
Imaging depth (mm)
0
10
20
30
Imaging width (mm)
0
10
20
30
(c)
1 mm
(d)
1 mm
(e)
Imaging depth (mm)
6
8
10
12
14
16
Imaging width (mm)
10
15
20
25
30
Cumulative displacement (mm)
0.5
0
-0.5
(f)
Imaging depth (mm)
Imaging width (mm)
Cumulative strain (%)
15
10
5
0
-5
-10
-15
(g)
Imaging depth (mm)
Imaging width (mm)
PWV (m/s)
6
4
2
0
-2
-4
-6
(h)
Imaging depth (mm)
Imaging width (mm)
Modulus (kPa)
100
80
60
40
20
0

Figure 6.11: The CTA (a) from a 79-y.o. male undergoing CEA showed severely-calcified, high-grade stenosis at the carotid bifurcation. However, PWI was performed in the CCA (blue dashed box), where two smaller calcified regions were observed (white arrows) and confirmed by H&E staining of the resected CCA segment (white arrows in c and d). The calcifications appear to correlate with regions of slightly lower intra-plaque displacement (white arrows in e) and elongation (white arrows in f). These same regions are depicted as areas of alternating positive and negative PWV (g) and increased modulus (h) throughout the depth of the plaque.

Figure 6.12 presents the CTA and intra-plaque mapping results from a case (M, 80.y.o.) exhibiting severely-calcified, high-grade stenosis at the bifurcation. Ultrasound imaging was performed on the right side using a plane wave sequence with 5 compounding angles at 1667 Hz. It is important to note that while the CTA (a) and gross pathology (c) both revealed nearly complete occlusion of the artery, only the highly calcified portion of the plaque on the near wall could be seen in the ultrasound image due to severe acoustic shadowing (pink arrow in b).

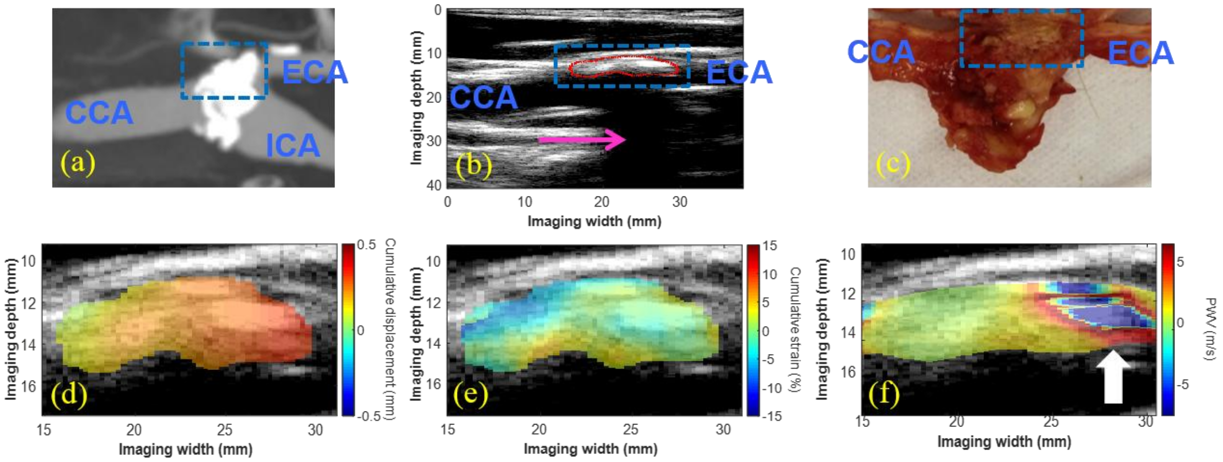

ECA
CCA
ICA
(a)
Imaging depth (mm)
0
10
20
30
40
CCA
ECA
(b)
0
10
20
30
Imaging width (mm)
CCA
ECA
(c)
Imaging depth (mm)
10
12
14
16
(d)
15
20
25
30
Imaging width (mm)
0.5
0
-0.5
Cumulative displacement (mm)
Imaging depth (mm)
10
12
14
16
(e)
15
20
25
30
Imaging width (mm)
15
10
5
0
-5
-10
-15
Cumulative strain (%)
Imaging depth (mm)
10
12
14
16
(f)
15
20
25
30
Imaging width (mm)
5
0
-5
PWV (m/s)

Figure 6.12: (a) CTA showing a severely-calcified, high-grade stenosis (80-99%) at the carotid bifurcation in an 80-y.o. male generating a severe acoustic shadow (pink arrow in b). A highly-calcified white nodule was identified on the gross pathology image (blue dashed box in c), correlating with the echoreflective region of the plaque on the B-mode (red contour in b). The intra-plaque displacement (d) and strain (e) maps revealed regions of varying displacement and strain amplitude, while the intra-plaque PWV map showed a region of alternating positive and negative PWVs throughout the depth of the plaque at the distal end (white arrow in f).

Figure 6.13 presents a case (M, 75 y.o.) in which the plaque possessed the acoustic properties of a lipid core – an echolucent center (red arrow in b) surrounded by an echogenic border indicative of the fibrous cap (white arrow). The resected specimen (c) revealed bilateral plaques at the proximal ICA. Examination by an expert pathologist identified that the plaque of interest in the near wall (blue dashed box) was oozing with fatty subintimal necrotic tissue in the form of a liquid-like substance. The white nodule in the far wall plaque (yellow arrow) represents a highly calcified lesion that likely caused the acoustic shadowing in (pink arrow in a). The intra-plaque cumulative strain map (e) indicated compression in the solid fibrous cap (white arrow) and elongation in the liquid-like fatty region (red arrow). The intra-plaque PWV map (f) revealed a transition from negative PWV to positive PWV in the direction of wave propagation at all depths of the plaque. This contrasted with the PWV maps of the calcified cases (Figures 6.10 – 6.12), in which alternating positive and negative PWV throughout the depth of the plaque appeared to correlate with the calcified region(s).

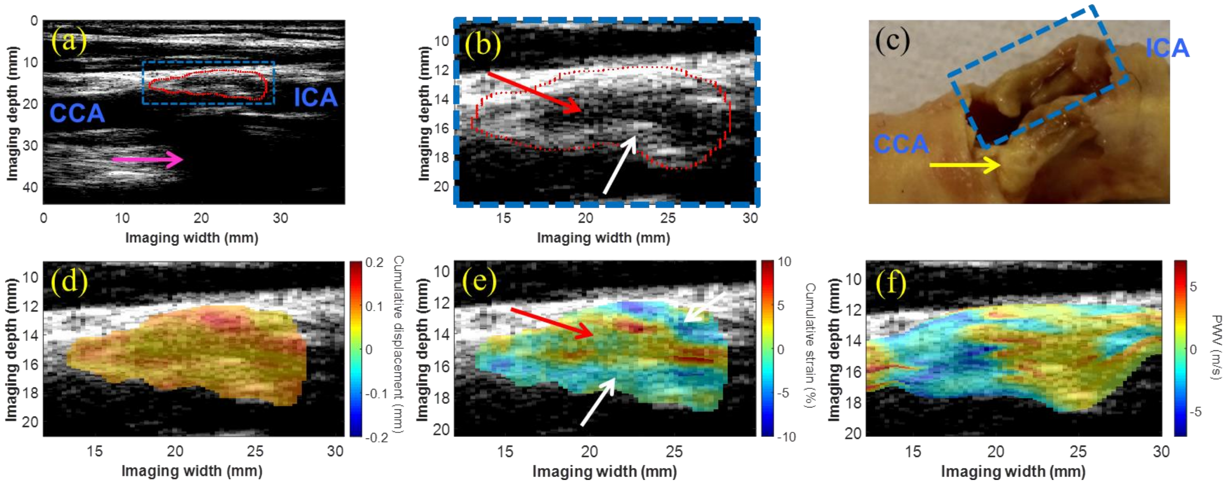

Figure 6.13: (a) The B-mode image of the carotid bifurcation in a 75-y.o. male shows the plaque (red contour) situated at the bifurcation and extending into the proximal ICA. Acoustic shadowing (pink arrow) is observed. (b) An enlarged image of the plaque ROI (blue box in a) shows an echolucent region (red arrow) surrounded by an echogenic border indicative of the fibrous cap (white arrow). (c) Gross pathology reveals bilateral plaques with liquid-like fatty substance oozing from the plaque of interest (blue dashed box). The white calcified nodule (yellow) in the far wall plaque is likely the main contributor to the acoustic shadowing observed in (a). The intra-plaque cumulative displacement map (d) is mostly uniform, while the

cumulative strain map (e) reveals compression in the solid fibrous cap (white arrow) and elongation in the liquid-like fatty region (red arrow). The intra-plaque PWV map (f) revealed a transition from negative PWV to positive PWV in the direction of wave propagation at all depths of the plaque.

6.4.3 Quantitative results

Figure 6.14 shows the cumulative displacement, cumulative strain, and PWV in both the normal wall (a, c, e) and the plaque region (b, d, f) for the each of the stenosis patients (P1 – P10) recruited in this study (RCA = right carotid artery, LCA = left carotid artery, Bif = plaque located at the bifurcation). Each bar was color-coded to reflect the degree of calcification in the plaque region as determined by visual assessment of the B-mode and CTA images (red = severely calcified, blue = moderately calcified, orange = lipid). Case P1 contained two plaque regions (Figure 6.9) that are labeled as P1-1 and P1-2 in (b) and (d). PWV was unable to be measured in the P1-2 plaque due to the lack of wave propagation and its location at the distal edge of the imaging plane. For comparison, the same measurements in the normal control group are also shown (a, c, e) as green bars. Compared to the normal wall, the displacement, strain, and PWV appeared to be lower in the plaque region for some cases and higher in other cases. These differences are quantified in Figure 6.15, which shows the percent change in cumulative displacement (a), cumulative strain (b), and PWV between the plaque region and a segment of the normal wall in each of the 10 patients. A negative percent change in cumulative displacement was observed in 8/11 plaque regions, while a negative percent change in cumulative strain was observed in 10/11 plaque regions. This suggests that the majority of the plaques were stiffer (i.e. displaced less or experienced lower strain amplitude) than the normal wall in the same subject. Elevated PWV may also be in an indicator of increased stiffness, however this was only observed in 4/10 plaque regions.

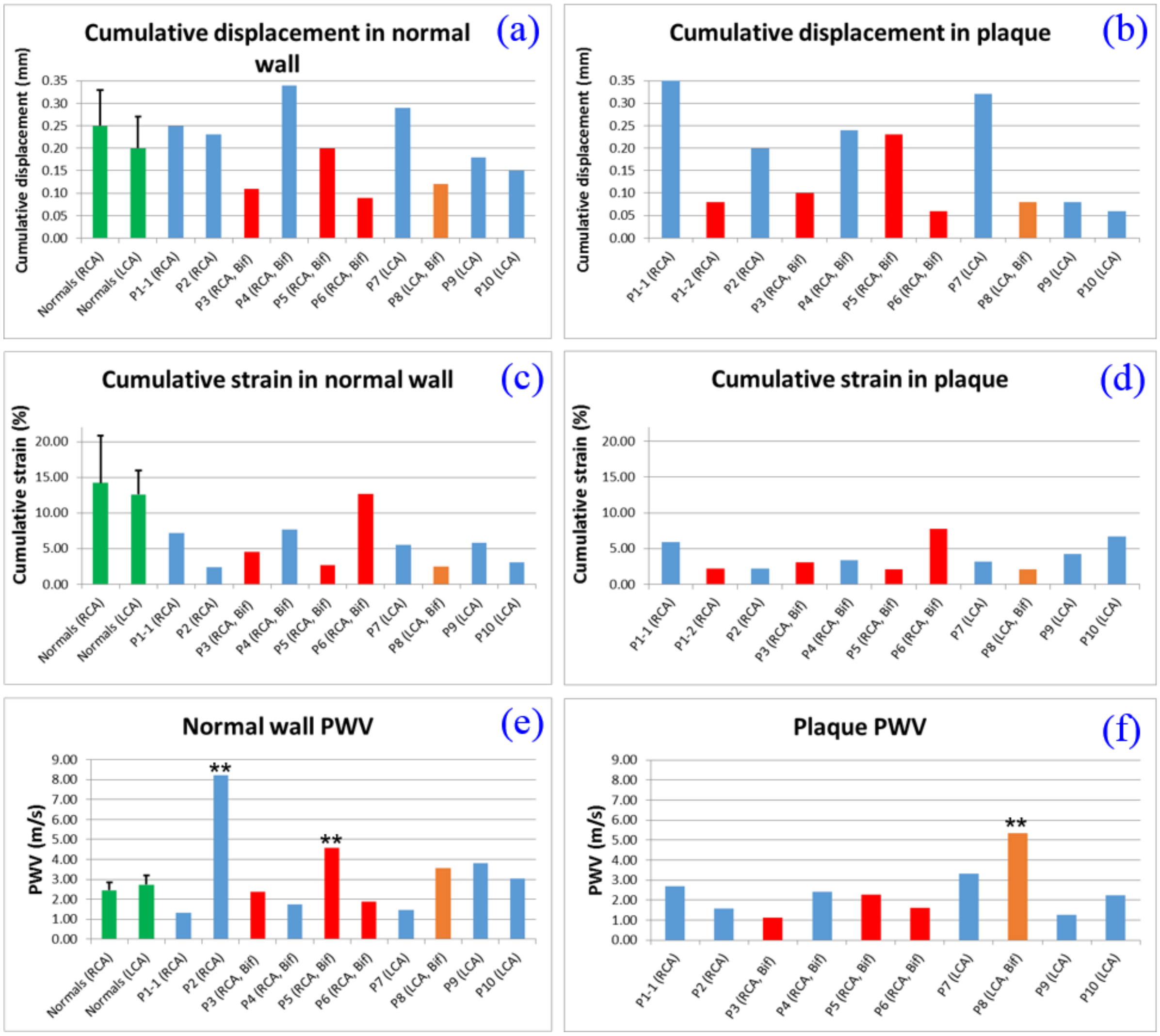

Figure 6.14: Cumulative displacement, cumulative strain, and PWV of both the normal wall (a, c, e) and the plaque region (b, d, f) for the each of the stenosis patients (P1 – P10). A red bar denotes a severely calcified plaque, while a blue bar denotes a moderately calcified plaque and the orange bar represents the lipid-filled case presented in Figure 6.13. The green bars denote the normal control group. In the label for each subject, RCA = right carotid artery, LCA = left carotid artery, and Bif = a plaque that was located at the bifurcation. ** denotes statistical significance with $p < 0.001$ compared to the normal controls.

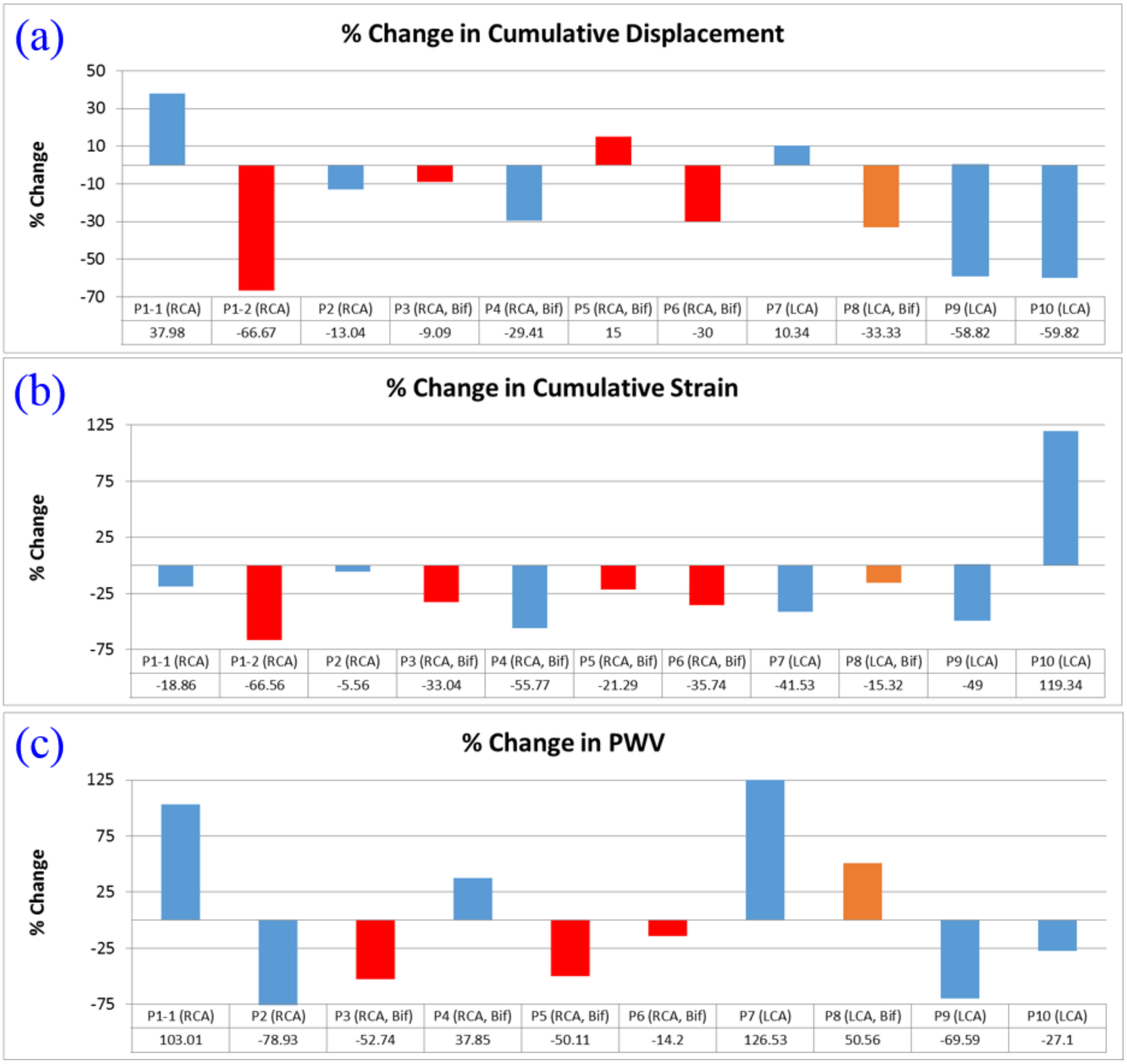

Figure 6.15: The percent change in (a) cumulative displacement, (b) cumulative strain, and (c) PWV of the plaque region compared to the normal wall in all 10 patients. A red bar denotes a severely calcified plaque, while a blue bar denotes a moderately calcified plaque and the orange bar represents the lipid case presented in Figure 6.13. In the label for each patient, RCA = right carotid artery, LCA = left carotid artery, and Bif = a plaque that was located at the bifurcation.

PWV, pulse wave-induced displacement and strain, and compliance for the three categories of plaque regions are summarized Figures 6.16-6.18 along with the same measurements for the 10 normal carotid arteries. There was no significant difference in PWV amongst the controls and each of the three categories of plaques (Figure 6.16). While there was no significant difference in displacement between the normal controls and the moderately calcified plaques, one-way ANOVA revealed that the non-calcified and severely calcified plaques exhibited significantly lower displacement ($p < 0.05$ and $p < 0.10$, respectively) compared to the normal controls (Fig. 6.17a). Cumulative strain was significantly lower ($p < 0.05$) in the plaque regions compared to the normal controls (Fig. 6.17b). Figure 6.18 shows that the plaque regions were found to be significantly less compliant than the normal carotid arteries using one-way ANOVA ($p < 0.05$), while the severely calcified plaques were significantly less compliant than the non-calcified/lipid and moderately calcified plaques ($p < 0.10$).

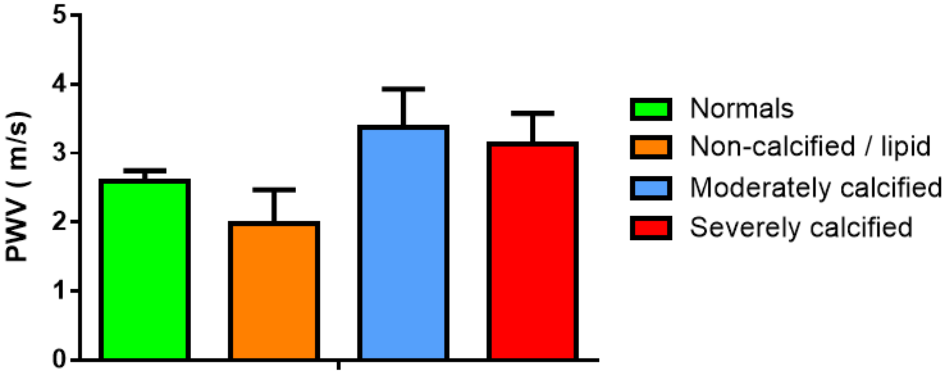

Figure 6.16: No significant difference in PWV was observed between the plaque cases (non-calcified/lipid, moderately calcified, and severely calcified) and the normal controls.

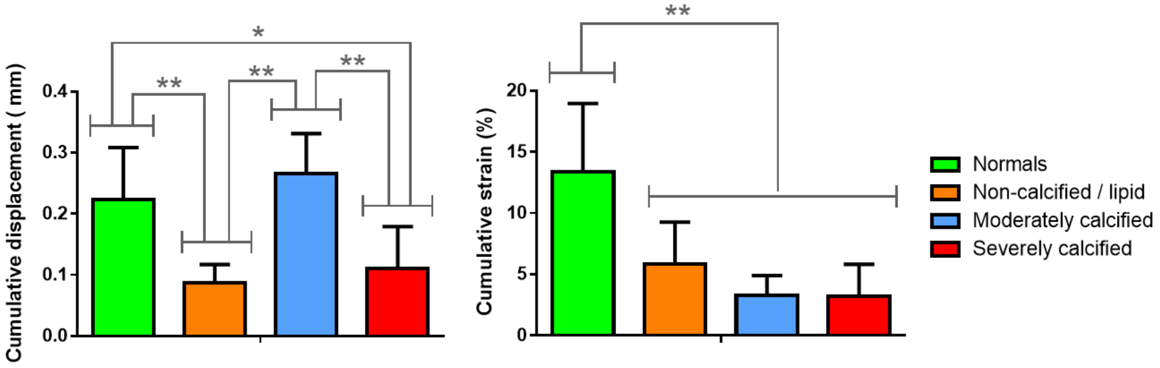

(a) (b)

Figure 6.17: (a) Cumulative displacement and (b) cumulative strain were computed within the normal carotid wall for the control group and within the plaque region(s) for each of the stenosis patients. * denotes statistical significance with $p < 0.10$, while ** denotes statistical significance with $p < 0.05$.

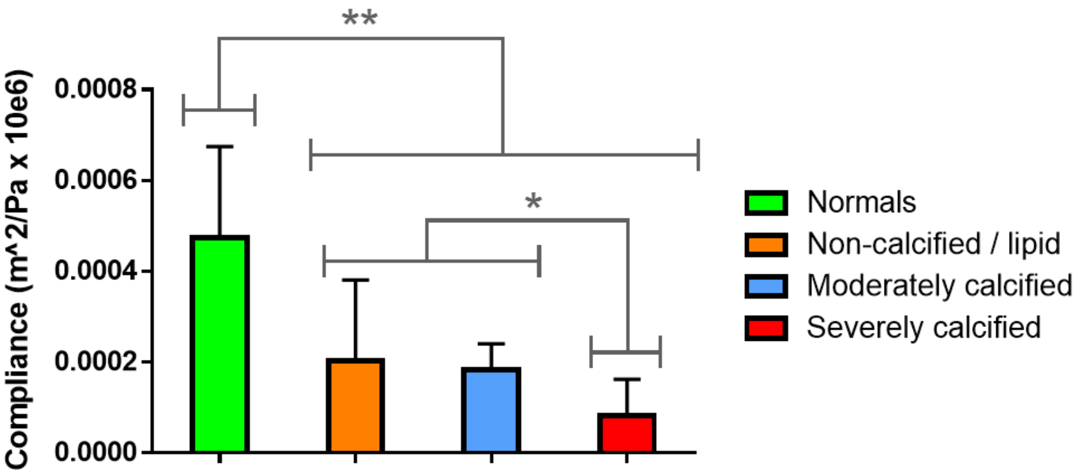

Figure 6.18: Compliance was computed based on the Bramwell-Hill model across the normal carotid segment for the control group and through the plaque region(s) for each of the stenosis patients. * denotes statistical significance with $p < 0.10$, while ** denotes statistical significance with $p < 0.05$.

6.5 Discussion and Conclusions

Noninvasive methods than can reveal new information regarding the composition and stability of carotid plaques may play a key role in plaque characterization and stroke prevention. In this study, the feasibility of PWI was evaluated in patients with moderate to severe carotid stenosis. In order to increase the resolution of the wave propagation analysis for the detection and characterization of regional lesions, piece-wise estimation of the PWV and modulus was introduced. Single-depth PWV and modulus maps were computed for four patients using the spatio-temporal map from one trace through both the normal wall and the plaque region. A conventional imaging sequence was used initially, and a plane wave sequence was also tested in two of the patients. The high spatial and temporal resolution achievable using plane wave architecture led to the development of intra-plaque PWV and modulus mapping, where multiple wall traces through the plaque were generated in order to investigate if and how the spatio-temporal maps at different depths were affected by inhomogeneities within the plaque. Intra-plaque results were shown for 3 patients undergoing CEA and compared to the CTA scan and/or resected plaque specimen from the same imaging location in order to validate plaque composition. Finally, cumulative displacement and cumulative strain maps were computed in all patients by summing the inter-frame displacements within the plaque ROI and computing the 1D spatial gradient. The change in cumulative displacement, cumulative strain, and PWV of the plaque compared to the normal wall was quantified in all patients.

Our initial hypothesis was that stiffer, calcified (i.e. stable) plaques will exhibit lower displacements, lower strain, and higher PWV than the normal wall compared to softer, lipid-filled (i.e. vulnerable) plaques. While this was true in two moderately calcified cases (i.e. P4 and P7 in Figure 6.14), the results were not as consistent in the other cases. For example, three of the severely calcified cases (P3, P5, and P6) exhibited lower cumulative strain but also lower PWV than the normal wall. Also, the lipid case (P8) was characterized by decreased displacement and strain as well as increased PWV, all signs of elevated stiffness. These observations may be explained by several physiological and imaging-related factors that must be taken into consideration when interpreting the measurements provided by PWI. Such factors will be discussed in this section, beginning with the turbulent flow arising from local geometric and mechanical changes of the artery in the presence of plaque [255].

One of the consistent observations from the single-depth PWV and modulus maps (Figures 6.5, 6.7-6.9) was that the PWV and modulus may appear higher around the plaque rather than within the plaque itself. For example, Figures 6.5g and 6.5h show regions of high PWV and modulus in the normal wall segments preceding and following the plaque, while the cases in Figures 6.7-6.9 also exhibited the highest PWV and modulus in a normal segment either preceding the plaque (6.8, 6.9) or following the plaque (6.7). We know that some degree of calcification was present in at least two of these cases (6.7 and 6.9) based on the acoustic shadowing underneath the plaque and the confirmation of calcified inclusions by the CTA in Figure 6.9a, so it is unlikely that the normal wall was actually stiffer than the plaque itself in these cases. The increased PWV and modulus in the normal wall next to the plaque may have been caused by turbulent flow and wave reflections.

In fluid mechanics, turbulence is characterized by a high Reynold’s number (i.e. > 4000), which is a dimensionless quantity that is used for the prediction of flow patterns in various situations [29]. While much of the hemodynamics in a healthy human body exhibits laminar flow (i.e. Reynolds number < 2100), turbulent flow is observed at some specific locations (such as the carotid bifurcation) and in the presence of atherosclerotic disease [256]. Simulations of stenosed carotid bifurcations using pulsatile inlet conditions have demonstrated the presence of vortices and oscillatory flow reversal distal to the region of stenosis [257]. Because blood is incompressible, blood flow in the arterial lumen must accompany regional wall motion during the cardiac cycle [258]. Thus, while wave propagation along the wall of a normal carotid artery is driven by laminar flow, the effects of turbulent flow in a stenotic artery may be manifested in its wall motion, particularly around stiff plaques exhibiting very little pulse wave-induced displacement.

In addition to causing turbulent flow conditions, the carotid bifurcation and regions of stenosis also serve as significant sources of wave reflection [259]. As stated in Chapter 1, the pulse waveform at any given site in the arterial tree is a combination of the forward wave and any reflected waves originating from further down the vasculature. These waves are propagating at speeds on the order of meters/second within a roughly 38-mm long segment of the stenotic carotid artery (i.e. equal to the width of the linear array transducer), generating multiple waves that may reflect and merge over the course of the cardiac cycle, particularly in cases such as Figures 6.7 and 6.9, where more than one plaque region was identified on the anterior wall. Thus, the composite pulse waveform at different scan line positions along a stenotic carotid artery may be influenced by different turbulent, reflective, and dispersive conditions, resulting in different wave speeds measured by PWI.

Turbulence, flow reversal, and reflected waves around the plaque may have also given rise to the negative PWVs that were observed in Figures 6.7c ad 6.8c. In these cases, the positive and negative PWVs converged at different points (within the plaque in 6.7c and before the plaque in 6.8c), suggesting that locations of wave convergence may provide clues regarding plaque properties. During a 6-month follow-up of the same patient in 6.8c using plane wave imaging, the point of convergence shifted from before the plaque (6.8c) to after the plaque (6.8g). This may be a result of the four-fold increase in both spatial and temporal resolution of the plane wave scanner, which provided the ability to capture more detailed wall motion dynamics and map the pulse wave propagation using four times as many scan lines.

Since blood flow imaging was not performed in this study, the fluid-solid interaction (FSI) between the blood and the wall could not be studied. The FSI is a crucial step in biomechanical modeling that couples computational fluid dynamics (CFD) with finite-element analysis (FEA) in tissues [260]. The mechanics of the fluid and structure systems are usually coupled at the interface by the kinematic and dynamic conditions, which define the velocity, pressure and/or other parameters of the fluid and structural nodes at the interface to be the same. In all four cases shown (Figures 6.5, 6.7-6.9), the increased PWV and modulus around the plaque is an observation that warrants further investigation through comparison with FSI simulations and phantom experiments. Most FSI studies of carotid arteries and stenosis have focused on wall shear stress, wall displacement, pressure, and flow velocity around the region of stenosis rather than wave propagation [261-263].

The disturbance in wall motion induced by turbulent flow and reflection within and around the stenotic region also presents the problem of varying waveform morphology. The fact that the composite pulse waveform at different scan line positions along a stenotic carotid artery may be influenced by turbulence, reflection, and dispersion means that the morphology of the waveform is changing as it propagates across a stenotic region. Based on the findings in Chapter 3, PWI has typically relied on tracking the 50% upstroke of each waveform in the spatio-temporal map. This makes sense under normal geometric conditions because wave reflections typically affect the back end (i.e. downstroke) and the peak of the forward wave [72]. However, the effects of complex wave interactions under stenotic conditions on PWV estimation using PWI requires further investigation. The 50% upstroke of the waveform in the normal wall may not represent the same point as the 50% upstroke of the waveform near or within a plaque region in the same field of view. Thus, the choice of tracking feature may affect the PWV estimation as well as the modulus calculation based on the Moens-Korteweg equation.

Moens-Korteweg assumptions

The Moens-Korteweg equation was established based on the assumptions of having an infinitely long, straight, isolated, and cylindrical vessel with elastic, isotropic, and homogenous walls, containing a homogenous, incompressible and nonviscous fluid [26, 29]. Several of these assumptions were compromised by carotid stenosis, which presents an artery that may not be straight or cylindrical, and certainly not infinitely long. Also, the wave speed (i.e. PWV) in the Moens-Korteweg equation represents the speed of the wave propagation with respect to the fluid, which may not be represented by the wave propagation in the wall under turbulent flow conditions. Piece-wise modulus mapping was implemented to mitigate the infinite length assumption by treating each piece-wise segment of the artery as its own section of an infinitely long tube consisting of a single PWV (i.e. that of the composite pulse waveform).

According to the Moens-Korteweg equation, the modulus is directly proportional to the diameter and the square of the PWV, and inversely proportional to the thickness. This means that stenotic regions, which are characterized by a reduction in diameter and an increase in thickness, will always be depicted as a region of lower modulus given a constant PWV. This may explain why the modulus of the plaque exhibited an inversely proportional relationship with the percentage of stenosis in the five cases where imaging was performed at the CCA (Figure 6.16d). The limitations of the Moens-Korteweg equation for stiffness mapping *in vivo* calls for the formulation of more realistic relationships between blood flow, pressure, and wall displacement.

Imaging location

The most common location for carotid plaque buildup is the bifurcation [264], which also serves as a significant reflection site for the arterial pulse wave. In cases where imaging was performed at the bifurcation, the wave propagation and induced displacements were the result of combined flow patterns caused by both the bifurcation and the plaque. This problem is further complicated by the observation that carotid bifurcation anatomy also exhibits major variation among individuals [265]. Computer simulation of local blood flow and vessel mechanics in a compliant carotid artery bifurcation model demonstrated strong secondary wall motion in the carotid sinus (i.e. the dilated area at the base of the ICA just superior to the bifurcation) [266]. Since all severely calcified cases (red bars in Figure 6.14) were imaged at the bifurcation, this may explain why the severely calcified cases did not exhibit noticeably lower displacement and strain than the moderately calcified and lipid cases.

Necrotic core within calcified area

The lipid case (P8 in Figure 6.14) was expected to experience higher displacement and strain compared to the moderately and severely calcified cases. However, this was not the case. One explanation may be that vulnerable and ruptured plaques have been known to hide in heavily calcified coronary arteries [267], and the same may be true for carotid arteries. Atherosclerotic calcification is recognized as a regulated process that occurs only when other aspects of atherosclerosis are also present [268], and increasing levels of calcification are believed to represent a transition into a more stable plaque – advanced atherosclerotic lesions may lead to calcification of the fibrous cap [269]. Comparison of the gross pathology for the lipid case presented in this study and other necrotic plaque cases in literature [270] revealed that our case consisted of a much thicker fibrous cap indicative of a stiffer, later-stage plaque.

When all the above factors are taken into account, the complexity of the arterial mechanics and dynamics in the presence of plaques becomes apparent. The effective characterization of plaques will likely rely on a combination of different imaging methods. In the presence of heavily calcified plaques, blooming artifacts on the CTA [271] and acoustic shadowing on the B-mode ultrasound image hinder the ability of both modalities to visualize the plaque. The high-intensity brightness on the CTA exaggerates the degree of stenosis, while the attenuation of the ultrasound signal by a calcification limits the view beneath the plaque. However, the use of multi-angle plane wave compounding may be able to enhance the signal underneath some heavily calcified plaques. Ultrasound is also advantageous for the imaging of lipid-rich plaques that may not show up well on CTA scans, which is clinically relevant due to the vulnerable nature of plaques high in lipid content.

Conclusions

The results from this pilot study demonstrated the potential of PWI to differentiate between plaques of varying stiffness, location, and composition based on the cumulative displacements, cumulative strains, PWV, and modulus. Phenomena such as pulse wave convergence, decreased strain, and alternating positive and negative PWVs within the plaque were observed and may serve as valuable information to compensate for the limitations of currently used methods for the assessment of stroke risk.

Chapter 7

Summary and Ongoing Work

7.1 Summary and Key Findings

In this dissertation, ultrasonic Pulse Wave Imaging (PWI) was developed as a novel, noninvasive method for visualizing and capturing arterial wall dynamics, which may provide new insights into the state and progression of vascular diseases such as abdominal aortic aneurysm (AAA), carotid stenosis, and hypertension. 1D cross-correlation-based speckle tracking of the ultrasound radiofrequency (RF) signals was used to spatio-temporally map the vessel wall displacements induced by the arterial pulse wave, facilitating the image-guided measurement of clinically relevant parameters such as the regional pulse wave velocity (PWV), wave propagation uniformity (r^2), pulse pressure (PP), and modulus.

A theoretical framework for assessing the tradeoff between the spatial and temporal resolution of PWI was established based on the upper limit of the PWV estimation. The performance of the PWI method using different image acquisition and signal processing parameters was assessed in canine aortas *ex vivo* and normal, healthy arteries *in vivo*. The results indicated that 24-48 ultrasound scan lines and a waveform upsampling factor > 2 should be used when imaging PWVs ~ 2.5 – 3.5 m/s with a conventional ultrasound scanner. In addition, the optimal pulse wave tracking feature for reliable PWV estimation was found to be the 50% upstroke of the incremental displacement waveform.

Three separate clinical studies were conducted on patients diagnosed with arterial disease to investigate the feasibility of PWI in pathological arteries. A pilot study in the abdominal aortas of patients with hypertension and AAA did not reveal a significant difference in regional PWV and r^2 between 13 normal subjects and 10 hypertensive subjects, which may have been attributed to confounding factors such as wave reflection, anti-hypertensive medication, and other diseases. However, the qualitative differences in the spatio-temporal maps between normal and hypertensive aortas may serve as biomarkers for disease. Significantly higher PWV and r^2 was measured in 5 aneurysmal aortas. In addition, a teetering motion was observed in all three aneurysms < 5 cm in diameter that was not present in the two aneurysms ~ 6 cm in diameter.

Pulse Wave Ultrasound Manometry (PWUM) was introduced as an extension of the PWI method for PP measurement in large central arteries. A feasibility study was conducted on normotensive, pre-hypertensive, and hypertensive patients to compare the aortic PP measured using PWUM with the brachial and radial PPs obtained using existing peripheral measurement instruments. A significantly higher PP in the hypertensive group was detected at the aortic site by PWUM, but not at the radial and brachial sites. No strong correlation between aortic PP and peripheral PP was observed in normal and pre-hypertensive subjects, while there was a relatively strong positive correlation between aortic PP and both radial and brachial PP in hypertensive subjects.

Finally, the potential of PWI to characterize atherosclerotic plaques was evaluated in patients with carotid artery stenosis. Piece-wise estimation of the PWV, diameter, and wall thickness was introduced for the detection and stiffness mapping of regional atherosclerotic lesions. Piece-wise PWV and modulus maps revealed that location(s) of wave convergence and variations in the cumulative pulse wave-induced displacement along a stenotic carotid artery may arise due to turbulent flow and wave reflections. These phenomenon may provide insights into the geometric and compositional properties of plaques. In patients undergoing carotid endarterectomy (CEA), piece-wise PWV and modulus mapping was also performed at multiple depths throughout a plaque region using plane wave ultrasound. The PWV and modulus through plaque regions as well as intra-plaque cumulative displacement and strain were quantified for the assessment of plaque stability based on its stiffness, with mixed results. In a CEA case exhibiting a lipid-filled plaque, the fibrous cap and fatty core could be delineated from the intra-plaque strain map, however the quantitative measurements from this case were also indicative of increased stiffness. Interpretation of the measurements provided by PWI in stenotic carotid arteries must take into consideration several physiological and imaging-related factors such as turbulent flow, wave reflection, imaging location, and the assumptions of the Moens-Korteweg equation.

7.2 Towards Clinical Implementation of PWI

Integration of PWI into clinical scanners requires several incremental improvements that we have implemented or are the in progress of implementing.

7.2.1 Improved B-Mode quality

Clinicians rely on high-quality B-Mode ultrasound images to identify structures of interest and perform initial assessment of the disease state. In order for PWI to be accepted as a clinical tool, high-quality B-Mode images must be provided along with accurate arterial displacement estimates at a high frame rates. Most medical ultrasound systems employ the standard Delay and Sum (DAS) beamforming method [92], which suffers from limited imaging resolution, particularly for plane wave systems. Although PWI using multi-angle plane wave transmissions allows for spatial compounding to improve image quality, many compounding angles (e.g. ~ 40) must be used to achieve a B-Mode contrast comparable to that obtained with multifocal transmit beamforming (i.e. conventional ultrasound), as see in Figure 7.1 [92].

To this end, we are implementing advanced beamforming algorithms such as the Delay Multiple and Sum (DMAS) method [272] that was previously introduced by Lim *et al* [273] for confocal microwave breast imaging and adapted for ultrasound by Matrone *et al*. The DMAS method has been show to increase B-Mode contrast and SNR, which will allow us to generate higher quality B-Mode images with fewer compounding angles so as to preserve the high frame rates (i.e. > 1000 Hz).

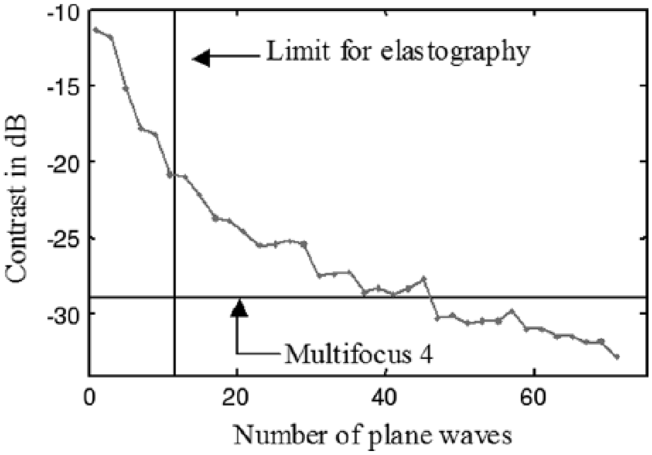

Figure 7.1. Contrast in the compound method versus number of plane waves. Source: Montaldo *et al* 2009).

7.2.2 Automated processing

A standardized clinical method should rely minimally on the operator to generate outputs. In its current state, PWI is based on manual segmentation of the artery walls and requires the user to identify linear trends in the waveform tracking points by eye. This may cause variations in PWV depending on which regions of the wall are segmented and which tracking points are used for PWV estimation.

In order to decrease the operator dependence of the PWI measurements, we have implemented semi-automated wall segmentation methods based on edge focusing [274, 275] and

Euclidean shortening flow [R13]. These algorithms have enabled us to identify the boundaries of the high-amplitude echoes corresponding to the arterial wall interfaces based on a user-defined region of interest (Figure 7.2). Ongoing research is aimed at completely automating this process by applying optical flow and region-growing methods, thus standardizing the wall segmentation step of the PWI processing chain.

We have also made progress in automated wave speed estimation by framing the regression step as a shortest path problem and implementing graph theory techniques to detect the most linear segments on the spatio-temporal map [276].

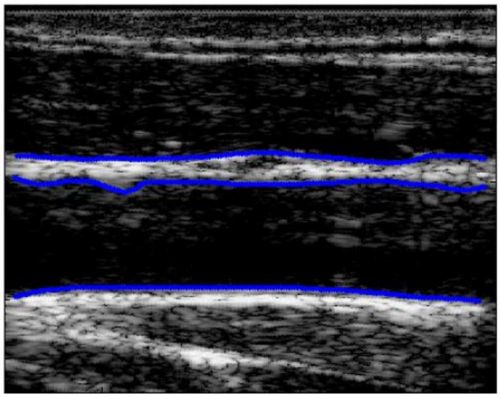

Figure 7.2: A normal carotid artery segmented using semi-automated methods.

7.2.3 Real-time PWI

Real-time PWI would provide clinicians with immediate results without the lag time required to process and interpret the images, which is one of the primary motivations for conducting ultrasound exams. Due to the massive amounts of imaging data that are acquired and saved during plane wave ultrasound, the beamforming and motion estimation steps can be very computationally intensive, thus limiting the frame rate of real-time PWI.

Our group had previously implemented a GPU-based sparse matrix beamforming method that resulted in a 100-fold increase in the speed of real-time displacement streaming [277]. We plan to integrate these methods into the PWI framework on the Verasonics Vantage system, enabling real-time visualization of arterial wall displacement. Combined with the automated processing steps outlined in Part 2, our system would be able to provide immediate feedback on arterial elasticity and wall dynamics during routine vascular ultrasound screening exams.

7.3 Unsupervised Machine Learning of PWI Parameters

One of the major challenges of introducing new physiological measurement methods into the clinic is the lack of prior data correlating the new parameters to outcomes. In order to attract clinical interest in the PWI method, we must demonstrate that the image-guided measurements provided by PWI have potential in classifying disease states and predicting outcomes. In addition to PWV and r^2, PWI has the ability to reveal a wealth of information about arterial wall dynamics and wave propagation that have not previously been studied in detail, including features like waveform morphology, peak displacement amplitudes, and frequency content. Unsupervised machine learning techniques such as principal component analysis (PCA) and cluster analysis provide efficient methods for detecting patterns in the feature set and assessing the separation among different subject groups based on the PWI measurements.

This section describes a framework for pulse wave feature extraction using PWI and unsupervised machine learning of the feature set. The ultimate goal is to establish connections between the most relevant pulse wave features and various disease states by answering the question “To what extent can PWI differentiate among different types of arteries based on only the pulse wave measurements it provides?” Preliminary results using a data set of healthy aortas and carotid arteries are presented in Section 7.3.4.

7.3.1 Machine learning for clinical data analysis and medical diagnosis

Machine learning techniques have made their way into the healthcare field for the analysis of clinical data and the detection and diagnosis of disease. In fact, some of the earliest machine learning algorithms were designed to analyze medical data sets [278] with the goal of improving diagnostic accuracy based on laboratory tests, device measurements, and/or patient symptoms [279-283]. The application of statistical and machine learning algorithms to patient data such as EMR (electronic medical records) and medical images is a promising and rapidly growing field that involves building powerful predictive tools for forecasting patient outcomes and performing automated diagnosis [284-286].

Machine learning can be broadly categorized into supervised and unsupervised techniques [287]. In general, supervised learning involves training the computer to associate features in a data set with known outcomes (i.e. truth labels), then applying those associations on unseen data in order to predict new outcomes. In the context of medicine, classification tasks such as identifying a subtype of lung cancer from DNA methylation markers [288] are often executed using supervised learning methods such as Bayesian statistics, linear and logistic regression, support vector machines, and neural networks [278]. Unsupervised machine learning is the process of finding patterns and relationships in a data set with no prior knowledge of its truth labels [289, 290]. Unsupervised learning techniques seek to organize a set of data into groups, or clusters, with similar features. Such methods are useful for exploratory purposes when the amount of data is large and it becomes very difficult to manually find relationships amongst the features.

Machine learning is also playing an essential role in the medical imaging field [291]. Active research areas include voxel analysis of fMRI data to delineate subgroups of neurodegenerative disease patients [292, 293], texture analysis to differentiate benign from malignant tumors [294], and pixel-based learning for lesion detection/classification [295]. In a similar fashion, the arterial pulse wave features that can be directly measured using PWI may serve as biomarkers for cardiovascular health. Due to the multiple clinical studies that have demonstrated a correlation between pulse wave features (i.e. velocity, morphology, amplitude, etc.), arterial function, and cardiovascular health [54, 71, 296-300], our goal is to establish a framework to organize different types of subjects into distinct clusters based on their PWI measurements.

7.3.2 Proposed methods: Pulse wave feature extraction

The first step is to define the set of features to be measured using PWI. Since the pulse wave-induced displacement waveform can be captured in both walls at multiple locations (i.e. scan line positions) along an arterial segment, features can be defined in the time, frequency, and spatio-temporal domains.

Time domain features

Figure 7.3 shows the anterior (i.e. near) and posterior (i.e. far) wall displacement waveforms from the central scan line of a normal human carotid artery over one cardiac cycle. Until now, the posterior wall displacement waveform has been largely ignored due to the lack of a forward propagating wave in some cases. However, a delay in the absolute value of the maximum displacement between the anterior and posterior walls has also been observed in the majority of normal cases (7.3a). Generally, the anterior wall reaches its maximum upstroke earlier than the posterior wall reaches its maximum downstroke. Features describing the waveform morphology include the time-to-peak (b), peak width (c), and peak displacement amplitude. Other time domain features of the pulse wave include the root mean square, band power, and maximum distension (introduced in Chapter 6 for plaque characterization in the carotid artery).

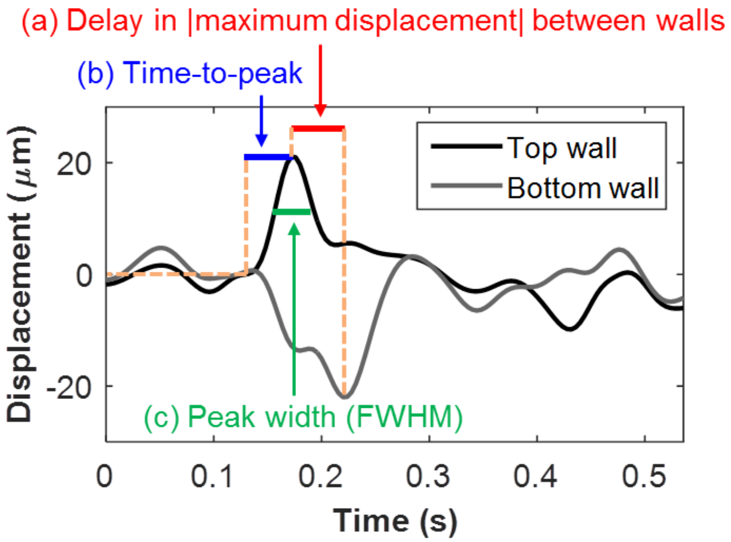

Figure 7.3: Time-domain features of the displacement waveforms include (a) the delay in the absolute value of the maximum displacement between the anterior (top) and posterior (bottom) walls, (b) the time lapsed for the waveform to reach its peak displacement value starting from its zero-crossing point, and (c) the peak width, which is defined as the full-width half-maximum.

Frequency domain features

The power spectra of the anterior wall displacement waveform over two cardiac cycles in shown in Figure 7.4. The highest power frequency component (a) is generally the heart rate, which may not be a good differentiator among subject groups. However, the second and third highest power frequency components (b, c) may correspond to high-amplitude wave reflections, which play an important role in cardiovascular disease [73].

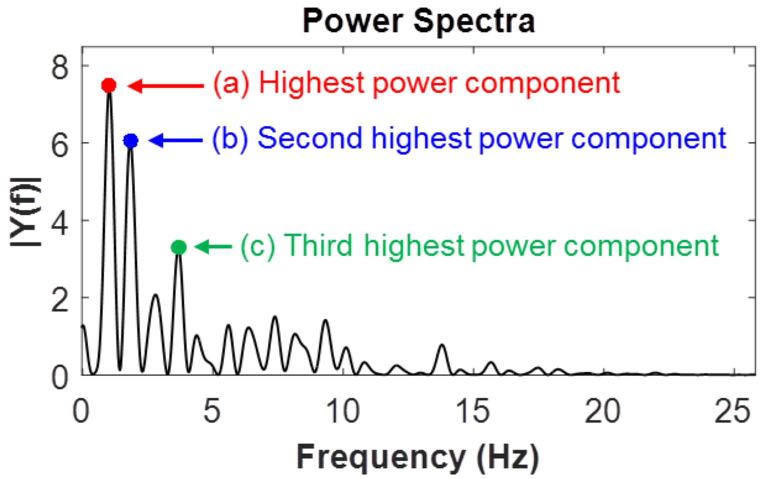

Figure 7.4: Frequency-domain features include the frequency and power of the (a) first, (b) second, and (c) third highest-amplitude frequency components obtained using a Fast Fourier Transform.

Spatio-temporal domain features

The PWV is considered a spatio-temporal feature because a single time point in the waveform is tracked over multiple scan lines. Similarly, the previously defined time and frequency domain features can be measured at all scan line positions. In Chapter 4, visual observation suggested that the morphology of the waveform was more variable along the imaged segment in hypertensive subjects compared to normal subjects. Thus, the variability of the time domain features may help differentiate normal from pathological arteries. By averaging the value of each time domain feature across all scan line positions, the variability can be defined as the ratio between the standard deviation and the mean. For preliminary testing, 30 features of the pulse wave were extracted.

7.3.3 Proposed methods: Unsupervised learning

Given the full set of pulse wave features for a large number of subjects, unsupervised learning provides a means of organizing the subjects into similar clusters based on the features accounting for the greatest variance in the data set [301, 302]. This approach emulates real world clinical diagnosis, where the patient's medical condition is unknown, and PWI is used to assess the probability that the patient belongs in a particular disease (or non-disease) group. The unsupervised learning methods used in this study include principal components analysis (PCA) and *k*-means clustering.

PCA

PCA is a commonly used dimensionality reduction technique that maps the original data onto a new coordinate system (i.e. the principal components space) and highlights the features responsible for the greatest variance in the original data. The 30 pulse wave features provide a 30-dimensional data set. Given a 2-D matrix in which each row represents a subject and each column represents a pulse wave feature, the covariance matrix is 30x30 matrix in which each element represents the covariance between two features X and Y, expressed as follows:

$$cov(X,Y) = \frac{\sum_{i-1}^{n}(X_i - \bar{X})(Y_i - \bar{Y})}{n-1}, \qquad [7.1]$$

where n is the number of subjects. The covariance matrix contains all the possible covariance values between the different dimensions (i.e. pulse wave features). That is, the first row represents the covariance between the first feature and all 30 features (including itself), the second row represents the covariance between the second feature and all 30 features, and so on. Thus, the covariance matrix is symmetric with its diagonal equal to the variance of each of the features (i.e. the covariance with itself).

PCA computes the eigenvalues and eigenvectors of the covariance matrix. This is the key step in dimension reduction – since all the eigenvectors of a matrix are orthogonal, PCA expresses the original data in terms of orthogonal eigenvectors. The eigenvalues are computed by solving the expression

$$\boldsymbol{A} - \lambda \boldsymbol{I} = 0, \qquad [7.2]$$

where $\boldsymbol{A}$ represents the covariance matrix, λ represents the eigenvalues, and $\boldsymbol{I}$ represents the identity matrix. For the 30x30 covariance matrix, we obtain 30 eigenvalues. The corresponding eigenvectors $\boldsymbol{e}_1, \boldsymbol{e}_2, \ldots, \boldsymbol{e}_{30}$ are obtained by solving the expression

$$\left(\boldsymbol{A} - \lambda_j \boldsymbol{I}\right)\boldsymbol{e}_j = 0 \qquad [7.3]$$

For high-dimensional data (e.g. a covariance matrix larger than 3x3), Eqns. 7.2 and 7.3 can be solved using complex iterative methods that are beyond the scope of this dissertation. In this study, PCA was executed using high-level mathematical solver functions in MATLAB.

Once the eigenvalues and eigenvectors have been obtained, the principal components of the data can be derived. In fact, the eigenvector corresponding to the largest eigenvalue is known as the *first principal component* of the original data. This means that the data exhibits the greatest variance, and hence significance, when it is projected onto this eigenvector. PCA yields as many eigenvectors as number of features in the original data. Generally, the first two principal components contain the majority of the significance, while the rest of the principal components are not useful representations of the data. Thus, PCA is effectively transforming a multi-dimensional data set into two dimensions – its principal components. An illustration of the PCA transformation on 2D data is shown in Figure 7.5. The original data, plotted in terms of features x_1 and x_2, is mapped onto the PCA space in terms of its first two principal components ϕ_1 and ϕ_2.

ϕ_1 passes through the middle of the points similar to a line of best fit, indicating that x_1 and x_2 are related along this eigenvector.

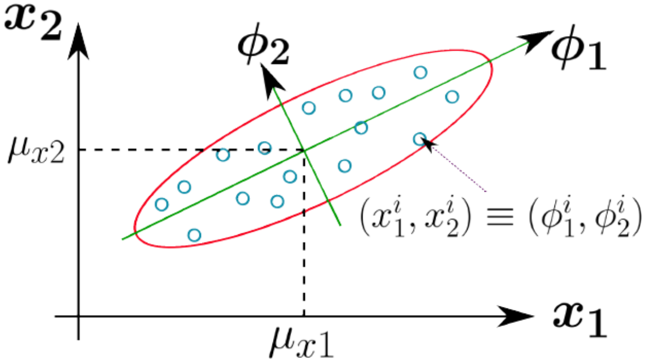

Figure 7.5: Illustration of the PCA transformation. The original data is plotted in terms of features x_1 and x_2. PCA computes the orthogonal eigenvectors ϕ_1 and ϕ_2 as the first and second principal components and maps the data onto the principal components coordinate system. Source: *Imperial College London, Department of Computing, Intelligent Data Analysis and Probabilistic Inference course, Lecture 15.*

k-means clustering

k-means is a standard clustering algorithm that partitions a data set into *k* clusters by initializing and iteratively updating the cluster centroids until the within-cluster sum of squares *J* is minimized. *J* is expressed as follows:

$$J = \sum_{j=1}^{k} \sum_{i=1}^{n} \left\| \boldsymbol{x}_i^{(j)} - \boldsymbol{c}_j \right\|^2, \qquad [7.4]$$

where *n* is the number of subjects, *c* represents the coordinates of the centroid of cluster *j*, and *x* represents the coordinates of a data point. Although the *k*-means algorithm can be extended to multiple dimensions, clustering will be performed in only two dimensions for the purposes of this dissertation. An illustration of the *k*-means clustering algorithm is described in Figure 7.6.

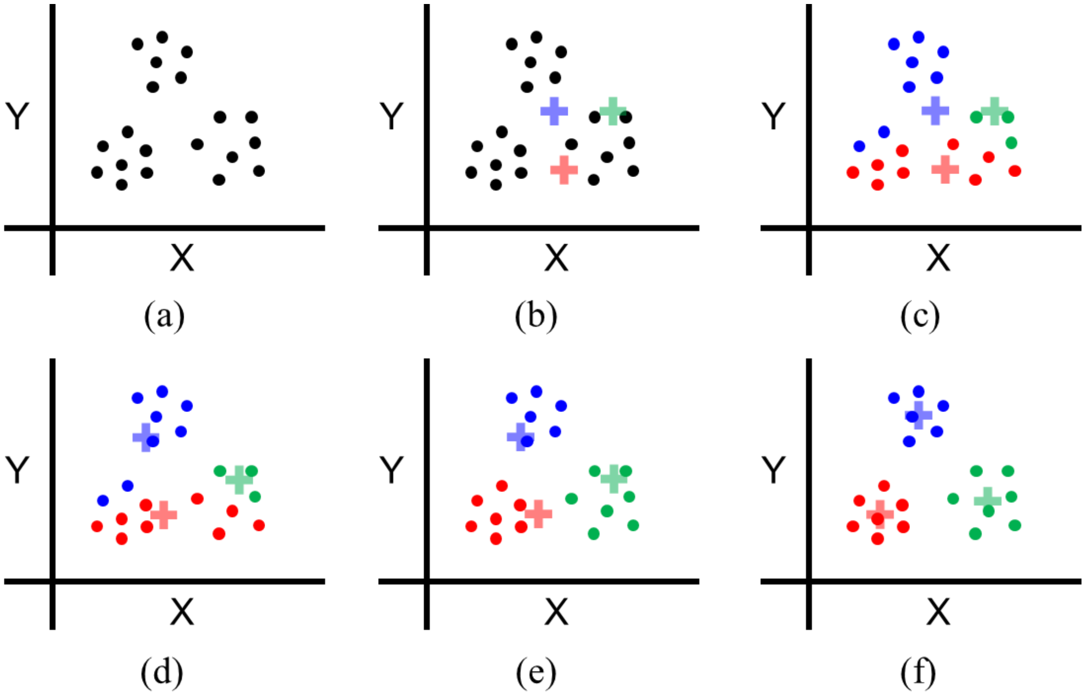

(a) (b) (c)

(d) (e) (f)

Figure 7.6: Illustration of the *k*-means clustering algorithm. (a) The 2D data is represented in terms of variables X and Y. In the context of PWI, X and Y can represent the first two principal components determined by PCA or any two pulse wave features (PWV, r^2, maximum displacement, peak width, etc.). Visual observation suggests that three distinct clusters exist. (b) Three cluster centroids (+'s) are randomly initialized in the X-Y space. (c) Each data point is assigned to a cluster based on the centroid it is closest to (i.e. minimum Euclidean distance). (d) New cluster centroids are computed using the newly assigned data points. (e) In the second iteration, the data points are re-assigned based on the newly computed cluster centroids. (f) After several iterations, the solution is achieved when no points are re-assigned (i.e. the within-cluster sum of squares is minimized).

For preliminary testing, PCA and *k*-means clustering were executed using the MATLAB functions *pca* and *kmeans*, respectively.

7.3.4 Preliminary results

The framework was tested using a data set containing the pulse wave features from the left common carotid arteries and abdominal aortas of 15 young, healthy subjects (10 M, 5 F, mean age 29.5 ± 5.0 years). Each feature was averaged over 5 cardiac cycles. The objective was to evaluate the performance of the unsupervised learning framework in differentiating between the carotid arteries and the aortas based on their pulse wave features.

PCA results are typically expressed using a bi-plot, which represents the multi-dimensional data in its 2-D principal components space. The bi-plot outputted by the *pca* function is shown in Figure 7.7, where each red point represents an artery (either carotid or aorta) and each pulse wave feature is represented by a loading vector (blue line). Each vector points in the direction of the principal component for which the variance is explained by that feature, and the magnitude of the vector indicates the extent to which that feature explains the variance.

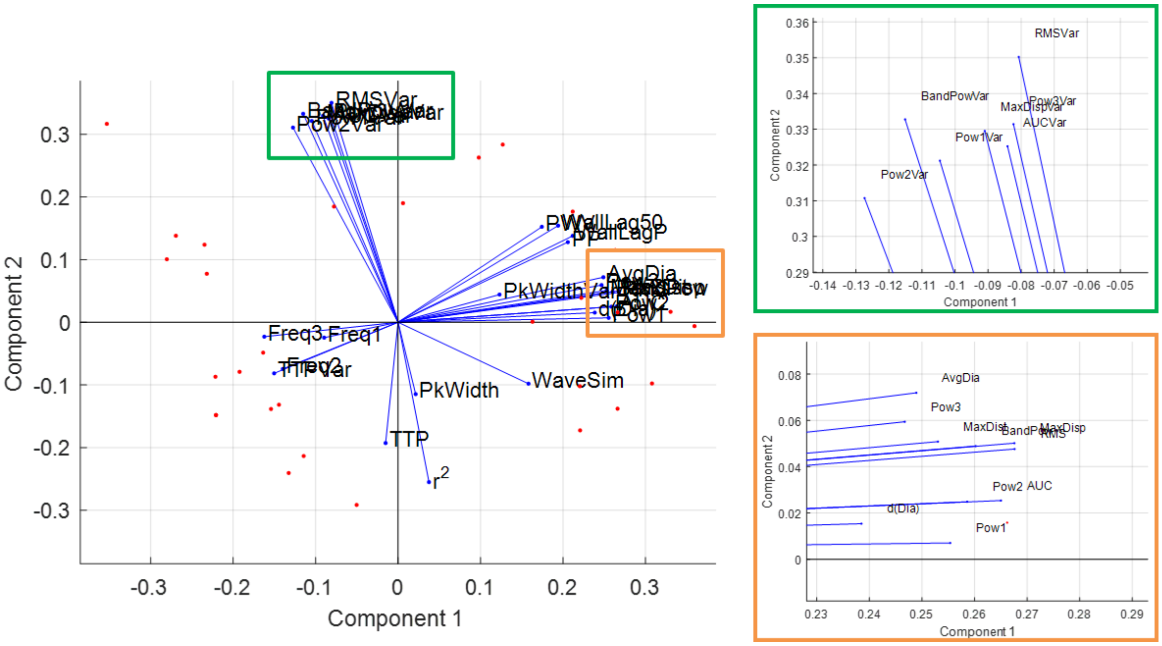

Figure 7.7: PCA bi-plot showing the principal component representation of the 30-dimensional data set containing the pulse wave features from the left carotid arteries and abdominal aortas of 15 healthy subjects.

Each red point represents either a carotid artery or an aorta, and each blue line represents the loading vector of one of the 30 pulse wave features. The orange box indicates a group of features exhibiting variance in the first (i.e. primary) principal component, while the green box indicates a group of features exhibiting variance in the second principal component.

Loading vectors of similar magnitude that point in the same direction represent highly correlated features, while vectors pointing in different directions represent highly uncorrelated features. For example, the green [orange] box in Figure 7.7 indicates a group of features that explain variance well in the second [first] principal component, but not the first [second]. If we take two features from the orange box, the root mean square (abbreviated RMS) and the maximum distension (abbreviated MaxDist), and plot them against each other (Figure 7.8a), we can observe the high degree of correlation. That is, higher RMS typically means greater maximum distension, which make sense because RMS is calculated based on the pulse wave amplitude, which also determines the amount of maximum distension. Conversely, plotting a feature from the orange box (RMS) against a feature from the green box (variability of the RMS, abbreviated RMSVar) yields no apparent correlation (Figure 7.8b).

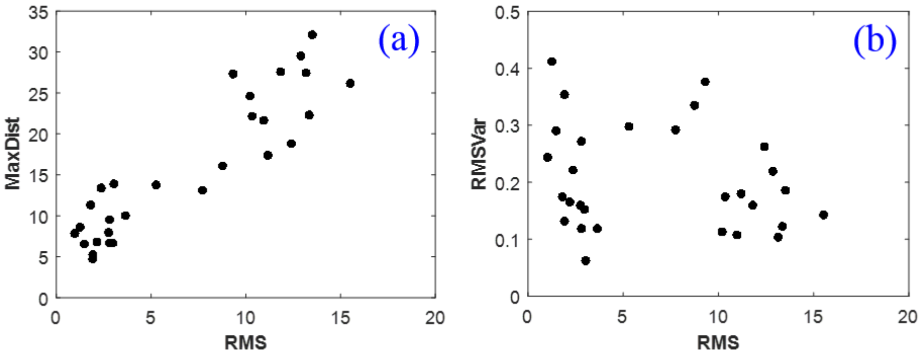

Figure 7.8: (a) Two highly correlated variables – maximum distension (MaxDist) and root-mean-square (RMS) vs. (b) two non-correlated variables – root mean square (RMS) and root mean square variability (RMSVar).

Figure 7.9 shows the *k*-means clustering results in both the principal components space and the 2D space represented by two correlated features – the PWV and the lag in peak displacement between the anterior and posterior walls (abbreviated WallLagP). In both cases, two clusters were specified for the *k*-means algorithm. In the principal components space (a), cluster 1 (red) contained 14 data points that were all carotid arteries, while cluster 2 (blue) contained 16 data points – 15 aortas and the remaining carotid artery. Thus, 29/30 (96.67%) arteries were correctly associated. In the WallLagP vs. PWV space, 15 out of 19 data points in cluster 1 (red) were carotid arteries and the remaining 4 were aortas, while all 11 data points in cluster 2 (blue) were aortas.

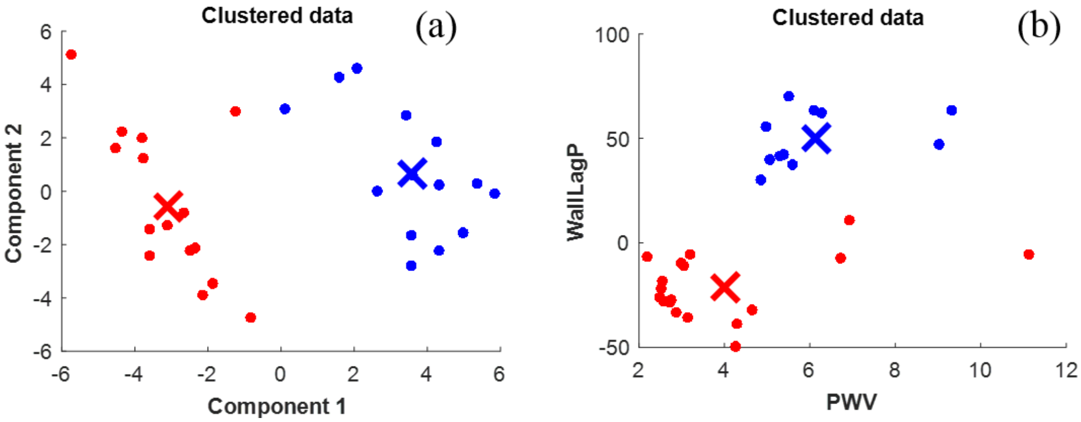

Figure 7.9: *k*-means clustering in (a) the principal components domain and (b) the 2D domain represented by the PWV (in m/s) and the lag in peak displacement between the anterior and posterior walls (WallLagP, in ms). Each data point represents a subject, and the X's represent cluster centroids.

These preliminary results demonstrate the feasibility of a pulse wave feature extraction and unsupervised machine learning framework to differentiate between two types of arteries based on solely the pulse wave features. The same principals can be applied in large groups of patients to correlate pulse wave features with various disease states.

Bibliography

1. Avolio, A.P., *Multi-branched model of the human arterial system.* Med Biol Eng Comput, 1980. **18**(6): p. 709-18.
2. McAllister, H.A., Jr., *An overview of human arterial pathology.* Toxicol Pathol, 1989. **17**(1 Pt 2): p. 219-31.
3. Kleinstreuer, C., Z. Li, and M.A. Farber, *Fluid-structure interaction analyses of stented abdominal aortic aneurysms.* Annu Rev Biomed Eng, 2007. **9**: p. 169-204.
4. Conen, D., et al., *Hypertension is an independent risk factor for contrast nephropathy after percutaneous coronary intervention.* Int J Cardiol, 2006. **110**(2): p. 237-41.
5. Puchmayer, V., et al., *[Hypertension as a risk factor for the development of obstructive peripheral artery disease]*. Vnitr Lek, 1980. **26**(7): p. 684-90.
6. Houston, M.C., *Hypertension and coronary heart disease risk factor management.* Aust Fam Physician, 1994. **23**(2): p. 243-5, 248-51.
7. Epstein, M., *Hypertension as a risk factor for progression of chronic renal disease.* Blood Press Suppl, 1994. **1**: p. 23-8.
8. Shimamoto, K., *[Hypertension as a risk factor for arteriosclerosis--a lesson from recent, large-scale clinical tests]*. Nihon Naika Gakkai Zasshi, 2005. **94**(3): p. 423-7.
9. Salky, N., *Hypertension as a risk factor for the development of coronary heart disease.* J Tenn Dent Assoc, 1978. **58**(1): p. 11-2.
10. Webster, J.R. and J.F. Marquardt, *Pulmonary embolism: silent killer of the elderly.* Geriatrics, 1974. **29**(7): p. 46-50.
11. Hedman, A.G., *Silent myocardial ischemia: pathophysiology and perioperative management.* Adv Pharmacol, 1994. **31**: p. 75-87.

12. Rapport, R.S., *Hypertension. Silent killer.* N J Med, 1999. **96**(3): p. 41-3.

13. Shah, S.N., V. Shah, and K. Chandrasekran, *Coronary artery disease in women: a silent killer.* J Okla State Med Assoc, 1999. **92**(6): p. 267-72.

14. Gordon, P.A. and B. Toursarkissian, *Treatment of abdominal aortic aneurysms: the role of endovascular repair.* AORN J, 2014. **100**(3): p. 241-59.

15. Mack, M. and A. Gopal, *Epidemiology, traditional and novel risk factors in coronary artery disease.* Cardiol Clin, 2014. **32**(3): p. 323-32.

16. Taylor, D.C. and D.E. Strandness, Jr., *Carotid artery duplex scanning.* J Clin Ultrasound, 1987. **15**(9): p. 635-44.

17. Taussky, P., R.A. Hanel, and F.B. Meyer, *Clinical considerations in the management of asymptomatic carotid artery stenosis.* Neurosurg Focus, 2011. **31**(6): p. E7.

18. Vorp, D.A., M.L. Raghavan, and M.W. Webster, *Mechanical wall stress in abdominal aortic aneurysm: influence of diameter and asymmetry.* J Vasc Surg, 1998. **27**(4): p. 632-9.

19. Vorp, D.A., *Biomechanics of abdominal aortic aneurysm.* J Biomech, 2007. **40**(9): p. 1887-902.

20. Nordon, I.M., et al., *Pathophysiology and epidemiology of abdominal aortic aneurysms.* Nat Rev Cardiol, 2011. **8**(2): p. 92-102.

21. Wang, T.J. and R.S. Vasan, *Epidemiology of uncontrolled hypertension in the United States.* Circulation, 2005. **112**(11): p. 1651-62.

22. Padwal, R., S.E. Straus, and F.A. McAlister, *Evidence based management of hypertension. Cardiovascular risk factors and their effects on the decision to treat hypertension: evidence based review.* BMJ, 2001. **322**(7292): p. 977-80.

23. Drazner, M.H., *The progression of hypertensive heart disease.* Circulation, 2011. **123**(3): p. 327-34.

24. Gates, P.E. and D.R. Seals, *Decline in large elastic artery compliance with age: a therapeutic target for habitual exercise.* Br J Sports Med, 2006. **40**(11): p. 897-9.

25. Wagenseil, J.E. and R.P. Mecham, *Elastin in large artery stiffness and hypertension.* J Cardiovasc Transl Res, 2012. **5**(3): p. 264-73.

26. Nichols, W.W., M.F. O'Rourke, and D.A.B.f.i.a. McDonald, *McDonald's Blood flow in arteries : theoretic, experimental and clinical principles*. 5th ed. ed. 2005, London: Hodder Arnold.

27. Dart, A.M. and B.A. Kingwell, *Pulse pressure--a review of mechanisms and clinical relevance.* J Am Coll Cardiol, 2001. **37**(4): p. 975-84.

28. Bambi, G., et al., *A novel ultrasound instrument for investigation of arterial mechanics.* Ultrasonics, 2004. **42**(1-9): p. 731-7.

29. Fung, Y.C. and Y.C.B. Fung, *Biomechanics : circulation*. 2nd ed. ed. 1997, New York ; London: Springer.

30. Greenwald, S.E., *Ageing of the conduit arteries.* J Pathol, 2007. **211**(2): p. 157-72.

31. Faury, G., et al., *Relation between outer and luminal diameter in cannulated arteries.* Am J Physiol, 1999. **277**(5 Pt 2): p. H1745-53.

32. Renna, N.F., N. de Las Heras, and R.M. Miatello, *Pathophysiology of vascular remodeling in hypertension.* Int J Hypertens, 2013. **2013**: p. 808353.

33. Shirwany, N.A. and M.H. Zou, *Arterial stiffness: a brief review.* Acta Pharmacol Sin, 2010. **31**(10): p. 1267-76.

34. Naghavi, M., et al., *From vulnerable plaque to vulnerable patient--Part III: Executive summary of the Screening for Heart Attack Prevention and Education (SHAPE) Task Force report.* Am J Cardiol, 2006. **98**(2A): p. 2H-15H.

35. Zieman, S.J., V. Melenovsky, and D.A. Kass, *Mechanisms, pathophysiology, and therapy of arterial stiffness.* Arterioscler Thromb Vasc Biol, 2005. **25**(5): p. 932-43.

36. Holzapfel, G.A. and H.W. Weizsacker, *Biomechanical behavior of the arterial wall and its numerical characterization.* Comput Biol Med, 1998. **28**(4): p. 377-92.

37. Sutton-Tyrrell, K., et al., *Elevated aortic pulse wave velocity, a marker of arterial stiffness, predicts cardiovascular events in well-functioning older adults.* Circulation, 2005. **111**(25): p. 3384-90.

38. Blacher, J., et al., *Impact of aortic stiffness on survival in end-stage renal disease.* Circulation, 1999. **99**(18): p. 2434-9.

39. Blacher, J., et al., *Carotid arterial stiffness as a predictor of cardiovascular and all-cause mortality in end-stage renal disease.* Hypertension, 1998. **32**(3): p. 570-4.

40. Laurent, S., et al., *Aortic stiffness is an independent predictor of all-cause and cardiovascular mortality in hypertensive patients.* Hypertension, 2001. **37**(5): p. 1236-41.

41. Boutouyrie, P., et al., *Aortic stiffness is an independent predictor of primary coronary events in hypertensive patients: a longitudinal study.* Hypertension, 2002. **39**(1): p. 10-5.

42. Laurent, S., et al., *Aortic stiffness is an independent predictor of fatal stroke in essential hypertension.* Stroke, 2003. **34**(5): p. 1203-6.

43. Beattie, D., et al., *Mechanical analysis of heterogeneous, atherosclerotic human aorta.* J Biomech Eng, 1998. **120**(5): p. 602-7.

44. Markussis, V., et al., *Abnormal carotid arterial wall dynamics in symptom-free hypopituitary adults.* Eur J Endocrinol, 1997. **136**(2): p. 157-64.

45. Christen, A.I., et al., *Arterial wall structure and dynamics in type 2 diabetes mellitus methodological aspects and pathophysiological findings.* Curr Diabetes Rev, 2010. **6**(6): p. 367-77.

46. Buchner, T., J. Pietkun, and P. Kuklik, *Complex activity patterns in arterial wall: results from a model of calcium dynamics.* Comput Biol Med, 2012. **42**(3): p. 267-75.

47. O'Rourke, M.F., A. Pauca, and X.J. Jiang, *Pulse wave analysis.* Br J Clin Pharmacol, 2001. **51**(6): p. 507-22.

48. Benthin, M., et al., *Calculation of pulse-wave velocity using cross correlation--effects of reflexes in the arterial tree.* Ultrasound Med Biol, 1991. **17**(5): p. 461-9.

49. Avicenna and O.C.t. Gruner, *A treatise on the Canon of medicine of Avicenna : incorporating a translation of the first book*. 1973: [New York : AMS Press, 1973].

50. McMullen, E.T., *Anatomy of a physiological discovery: William Harvey and the circulation of the blood.* J R Soc Med, 1995. **88**(9): p. 491-8.

51. Bleasdale, R.A., K.H. Parker, and C.J. Jones, *Chasing the wave. Unfashionable but important new concepts in arterial wave travel.* Am J Physiol Heart Circ Physiol, 2003. **284**(6): p. H1879-85.

52. Caro, C.G., *The mechanics of the circulation*. 1978, Oxford: Oxford University Press.

53. Mahomed, F.A., *The physiology and clinical use of the sphygmograph.* Med Times Gazette, 1872. **1**(62).

54. Wilkinson, I.B., et al., *Pulse-wave analysis: clinical evaluation of a noninvasive, widely applicable method for assessing endothelial function.* Arterioscler Thromb Vasc Biol, 2002. **22**(1): p. 147-52.

55. Gibbons, G.H. and V.J. Dzau, *The emerging concept of vascular remodeling.* N Engl J Med, 1994. **330**(20): p. 1431-8.

56. McVeigh, G.E., *Pulse waveform analysis and arterial wall properties.* Hypertension, 2003. **41**(5): p. 1010-1.

57. O'Rourke, M.F. and W.W. Nichols, *Potential for use of pulse wave analysis in determining the interaction between sildenafil and glyceryl trinitrate.* Clin Cardiol, 2002. **25**(6): p. 295-9.

58. Abdelhamid, M.F., *Commentary: Effect of graft fabric on pulse wave velocity following endovascular aneurysm repair.* J Endovasc Ther, 2014. **21**(6): p. 859-60.

59. Naka, K.K., et al., *Flow-mediated changes in pulse wave velocity: a new clinical measure of endothelial function.* Eur Heart J, 2006. **27**(3): p. 302-9.

60. Alastruey, J., et al., *Pulse wave propagation in a model human arterial network: Assessment of 1-D visco-elastic simulations against in vitro measurements.* J Biomech, 2011. **44**(12): p. 2250-8.

61. Gidlung, A.S. and I.G. Porje, *Studies of the arterial pulse wave.* Acta Radiol, 1948. **29**(6): p. 509-15.

62. Feinberg, A.W., *Studies of the arterial pulse wave.* Circulation, 1958. **18**(6): p. 1125-30.

63. Delcker, A., H.C. Diener, and H. Wilhelm, *Influence of vascular risk factors for atherosclerotic carotid artery plaque progression.* Stroke, 1995. **26**(11): p. 2016-22.

64. Cameron, J. and A. Dart, *Pulse wave velocity as a marker of vascular disease.* Lancet, 1996. **348**(9041): p. 1586-7.

65. Lehmann, E.D., *Clinical value of aortic pulse-wave velocity measurement.* Lancet, 1999. **354**(9178): p. 528-9.

66. Davies, J.I. and A.D. Struthers, *Pulse wave analysis and pulse wave velocity: a critical review of their strengths and weaknesses.* J Hypertens, 2003. **21**(3): p. 463-72.

67. Hirata, K., M. Kawakami, and M.F. O'Rourke, *Pulse wave analysis and pulse wave velocity: a review of blood pressure interpretation 100 years after Korotkov.* Circ J, 2006. **70**(10): p. 1231-9.

68. Willum-Hansen, T., et al., *Prognostic value of aortic pulse wave velocity as index of arterial stiffness in the general population.* Circulation, 2006. **113**(5): p. 664-70.

69. Ben-Shlomo, Y., et al., *Aortic pulse wave velocity improves cardiovascular event prediction: an individual participant meta-analysis of prospective observational data from 17,635 subjects.* J Am Coll Cardiol, 2013. **63**(7): p. 636-46.

70. Ku, D.N., et al., *Pulsatile flow and atherosclerosis in the human carotid bifurcation. Positive correlation between plaque location and low oscillating shear stress.* Arteriosclerosis, 1985. **5**(3): p. 293-302.

71. Weber, T., et al., *Arterial stiffness, wave reflections, and the risk of coronary artery disease.* Circulation, 2004. **109**(2): p. 184-9.

72. Nichols, W.W., et al., *Effects of arterial stiffness, pulse wave velocity, and wave reflections on the central aortic pressure waveform.* J Clin Hypertens (Greenwich), 2008. **10**(4): p. 295-303.

73. Laskey, W.K. and W.G. Kussmaul, *Arterial wave reflection in heart failure.* Circulation, 1987. **75**(4): p. 711-22.

74. Bleasdale, R.A., et al., *Wave intensity analysis from the common carotid artery: a new noninvasive index of cerebral vasomotor tone.* Heart Vessels, 2003. **18**(4): p. 202-6.

75. Heffernan, K.S., et al., *Influence of arterial wave reflection on carotid blood pressure and intima-media thickness in older endurance trained men and women with pre-hypertension.* Clin Physiol Funct Imaging, 2009. **29**(3): p. 193-200.

76. Hughes, A.D., J.E. Davies, and K.H. Parker, *The importance of wave reflection: A comparison of wave intensity analysis and separation of pressure into forward and backward components.* Conf Proc IEEE Eng Med Biol Soc, 2013. **2013**: p. 229-32.

77. Ghasemzadeh, N. and A.M. Zafari, *A brief journey into the history of the arterial pulse.* Cardiol Res Pract, 2011. **2011**: p. 164832.

78. Kang, J.H., et al., *A comparison between central blood pressure values obtained by the Gaon system and the SphygmoCor system.* Hypertens Res, 2012. **35**(3): p. 329-33.

79. Vermeersch, S.J., et al., *Age and gender related patterns in carotid-femoral PWV and carotid and femoral stiffness in a large healthy, middle-aged population.* J Hypertens, 2008. **26**(7): p. 1411-9.

80. Millasseau, S.C., et al., *Evaluation of carotid-femoral pulse wave velocity: influence of timing algorithm and heart rate.* Hypertension, 2005. **45**(2): p. 222-6.

81. Mookerjee, A., A.M. Al-Jumaily, and A. Lowe, *Arterial pulse wave velocity measurement: different techniques, similar results--implications for medical devices.* Biomech Model Mechanobiol, 2010. **9**(6): p. 773-81.

82. Macgowan, C.K., R.M. Henkelman, and M.L. Wood, *Pulse-wave velocity measured in one heartbeat using MR tagging.* Magn Reson Med, 2002. **48**(1): p. 115-21.

83. Ibrahim el, S.H., et al., *Measuring aortic pulse wave velocity using high-field cardiovascular magnetic resonance: comparison of techniques.* J Cardiovasc Magn Reson, 2010. **12**: p. 26.

84. Calabia, J., et al., *Doppler ultrasound in the measurement of pulse wave velocity: agreement with the Complior method.* Cardiovasc Ultrasound, 2011. **9**: p. 13.

85. Meinders, J.M., et al., *Assessment of local pulse wave velocity in arteries using 2D distension waveforms.* Ultrason Imaging, 2001. **23**(4): p. 199-215.

86. Eriksson, A., et al., *Arterial pulse wave velocity with tissue Doppler imaging.* Ultrasound Med Biol, 2002. **28**(5): p. 571-80.

87. Hedrick, W.R., D.L. Hykes, and D.E. Starchman, *Ultrasound physics and instrumentation*. 4th ed. ed. 2005, St. Louis, Mo.: Elsevier Mosby.

88. Christensen, D.A., *Ultrasonic bioinstrumentation*. 1988: Wiley.

89. Tanter, M. and M. Fink, *Ultrafast imaging in biomedical ultrasound.* IEEE Trans Ultrason Ferroelectr Freq Control, 2014. **61**(1): p. 102-19.

90. Jensen, J.A., et al., *Ultrasound research scanner for real-time synthetic aperture data acquisition.* IEEE Trans Ultrason Ferroelectr Freq Control, 2005. **52**(5): p. 881-91.

91. Udesen, J., et al., *High frame-rate blood vector velocity imaging using plane waves: simulations and preliminary experiments.* IEEE Trans Ultrason Ferroelectr Freq Control, 2008. **55**(8): p. 1729-43.

92. Montaldo, G., et al., *Coherent plane-wave compounding for very high frame rate ultrasonography and transient elastography.* IEEE Trans Ultrason Ferroelectr Freq Control, 2009. **56**(3): p. 489-506.

93. Gennisson, J.L., et al., *Ultrasound elastography: principles and techniques.* Diagn Interv Imaging, 2013. **94**(5): p. 487-95.

94. Gao, L., et al., *Imaging of the elastic properties of tissue--a review.* Ultrasound Med Biol, 1996. **22**(8): p. 959-77.

95. Ophir, J., et al., *Elastography: a quantitative method for imaging the elasticity of biological tissues.* Ultrason Imaging, 1991. **13**(2): p. 111-34.

96. Parker, K.J., et al., *Vibration sonoelastography and the detectability of lesions.* Ultrasound Med Biol, 1998. **24**(9): p. 1437-47.

97. D'Hooge, J., et al., *Echocardiographic strain and strain-rate imaging: a new tool to study regional myocardial function.* IEEE Trans Med Imaging, 2002. **21**(9): p. 1022-30.

98. Mai, J.J. and M.F. Insana, *Strain imaging of internal deformation.* Ultrasound Med Biol, 2002. **28**(11-12): p. 1475-84.

99. Wilson, L.S. and D.E. Robinson, *Ultrasonic measurement of small displacements and deformations of tissue.* Ultrason Imaging, 1982. **4**(1): p. 71-82.

100. Dickinson, R.J. and C.R. Hill, *Measurement of soft tissue motion using correlation between A-scans.* Ultrasound Med Biol, 1982. **8**(3): p. 263-71.

101. de Korte, C.L. and A.F. van der Steen, *Intravascular ultrasound elastography: an overview*. Ultrasonics, 2002. **40**(1-8): p. 859-65.

102. Doherty, J.R., et al., *Acoustic radiation force elasticity imaging in diagnostic ultrasound.* IEEE Trans Ultrason Ferroelectr Freq Control, 2013. **60**(4): p. 685-701.

103. Sebag, F., et al., *Shear wave elastography: a new ultrasound imaging mode for the differential diagnosis of benign and malignant thyroid nodules.* J Clin Endocrinol Metab, 2010. **95**(12): p. 5281-8.

104. Bercoff, J., M. Tanter, and M. Fink, *Supersonic shear imaging: a new technique for soft tissue elasticity mapping.* IEEE Trans Ultrason Ferroelectr Freq Control, 2004. **51**(4): p. 396-409.

105. Sorace, A.G., et al., *Ultrasound measurement of brachial artery elasticity prior to hemodialysis access placement: a pilot study.* J Ultrasound Med, 2012. **31**(10): p. 1581-8.

106. Zhang, P., et al., *Effect of smoking on common carotid artery wall elasticity evaluated by echo tracking technique.* Ultrasound Med Biol, 2014. **40**(3): p. 643-9.

107. Kremer, F., et al., *2D myocardial strain assessment in the mouse: a comparison between a synthetic lateral phase approach and block-matching using computer simulation.* Ultrasonics, 2012. **52**(7): p. 936-42.

108. Li, Y., et al., *Quantification and MRI validation of regional contractile dysfunction in mice post myocardial infarction using high resolution ultrasound.* Ultrasound Med Biol, 2007. **33**(6): p. 894-904.

109. Konofagou, E.E., J. D'Hooge, and J. Ophir, *Myocardial elastography--a feasibility study in vivo.* Ultrasound Med Biol, 2002. **28**(4): p. 475-82.

110. Lee, W.N., et al., *Theoretical quality assessment of myocardial elastography with in vivo validation.* IEEE Trans Ultrason Ferroelectr Freq Control, 2007. **54**(11): p. 2233-45.

111. Sutherland, G.R., et al., *Strain and strain rate imaging: a new clinical approach to quantifying regional myocardial function.* J Am Soc Echocardiogr, 2004. **17**(7): p. 788-802.

112. Chen, X., et al., *3-D correlation-based speckle tracking.* Ultrason Imaging, 2005. **27**(1): p. 21-36.

113. Dewall, R.J., *Ultrasound elastography: principles, techniques, and clinical applications.* Crit Rev Biomed Eng, 2013. **41**(1): p. 1-19.

114. Favreau, J.T., et al., *Murine ultrasound imaging for circumferential strain analyses in the angiotensin II abdominal aortic aneurysm model.* J Vasc Surg, 2012. **56**(2): p. 462-9.

115. Taniguchi, R., et al., *Strain analysis of wall motion in abdominal aortic aneurysms.* Ann Vasc Dis, 2014. **7**(4): p. 393-8.

116. Park, D.W., et al., *Arterial elasticity imaging: comparison of finite-element analysis models with high-resolution ultrasound speckle tracking.* Cardiovasc Ultrasound, 2010. **8**: p. 22.

117. Allen, J.D., et al., *The development and potential of acoustic radiation force impulse (ARFI) imaging for carotid artery plaque characterization.* Vasc Med, 2011. **16**(4): p. 302-11.

118. Luo, J., R.X. Li, and E.E. Konofagou, *Pulse wave imaging of the human carotid artery: an in vivo feasibility study.* IEEE Trans Ultrason Ferroelectr Freq Control, 2012. **59**(1): p. 174-81.

119. Luo, J., et al., *Pulse wave imaging of normal and aneurysmal abdominal aortas in vivo.* IEEE Trans Med Imaging, 2009. **28**(4): p. 477-86.

120. Li, R.X., et al., *Pulse wave imaging in normal, hypertensive and aneurysmal human aortas in vivo: a feasibility study.* Phys Med Biol, 2013. **58**(13): p. 4549-62.

121. Vappou, J., J. Luo, and E.E. Konofagou, *Pulse wave imaging for noninvasive and quantitative measurement of arterial stiffness in vivo.* Am J Hypertens, 2010. **23**(4): p. 393-8.

122. Fujikura, K., et al., *A novel noninvasive technique for pulse-wave imaging and characterization of clinically-significant vascular mechanical properties in vivo.* Ultrason Imaging, 2007. **29**(3): p. 137-54.

123. Shahmirzadi, D., et al., *Mapping the longitudinal wall stiffness heterogeneities within intact canine aortas using Pulse Wave Imaging (PWI) ex vivo.* J Biomech, 2013. **46**(11): p. 1866-74.

124. Vappou, J., et al., *Aortic Pulse Wave Velocity Measured by Pulse Wave Imaging (Pwi): A Comparison with Applanation Tonometry.* Artery Res, 2011. **5**(2): p. 65-71.

125. Nandlall, S.D., et al., *Monitoring and staging abdominal aortic aneurysm disease with pulse wave imaging.* Ultrasound Med Biol, 2014. **40**(10): p. 2404-14.

126. Goergen, C.J., et al., *Increased anterior abdominal aortic wall motion: possible role in aneurysm pathogenesis and design of endovascular devices.* J Endovasc Ther, 2007. **14**(4): p. 574-84.

127. O'Rourke, M.F. and A. Adji, *Noninvasive generation of aortic pressure from radial pressure waveform by applanation tonometry, brachial cuff calibration, and generalized transfer function.* Am J Hypertens, 2014. **27**(2): p. 143-5.

128. Cheng, H.M., et al., *Measurement accuracy of non-invasively obtained central blood pressure by applanation tonometry: a systematic review and meta-analysis.* Int J Cardiol, 2013. **167**(5): p. 1867-76.

129. Nielsen, B.L., et al., *Carotid-femoral pulse wave velocity.* J Am Geriatr Soc, 1968. **16**(6): p. 658-65.

130. Khamdaeng, T., et al., *Arterial stiffness identification of the human carotid artery using the stress-strain relationship in vivo.* Ultrasonics, 2012. **52**(3): p. 402-11.

131. Hermeling, E., et al., *Measurement of local pulse wave velocity: effects of signal processing on precision.* Ultrasound Med Biol, 2007. **33**(5): p. 774-81.

132. Kruizinga, P., et al., *Plane-wave ultrasound beamforming using a nonuniform fast Fourier transform.* IEEE Trans Ultrason Ferroelectr Freq Control, 2012. **59**(12): p. 2684-91.

133. Hansen, H.H., et al., *Ultrafast vascular strain compounding using plane wave transmission.* J Biomech, 2014. **47**(4): p. 815-23.

134. Kruizinga, P., et al., *High-definition imaging of carotid artery wall dynamics.* Ultrasound Med Biol, 2014. **40**(10): p. 2392-403.

135. Couade, M., et al., *Ultrafast imaging of the arterial pulse wave.* IRBM, 2011. **32**(2): p. 106-108.

136. Hasegawa, H., K. Hongo, and H. Kanai, *Measurement of regional pulse wave velocity using very high frame rate ultrasound.* J Med Ultrasonics, 2013. **40**(2): p. 91-98.

137. Luo, J. and E. Konofagou, *A fast normalized cross-correlation calculation method for motion estimation.* IEEE Trans Ultrason Ferroelectr Freq Control, 2010. **57**(6): p. 1347-57.

138. Babin, D., et al., *Robust segmentation methods with an application to aortic pulse wave velocity calculation.* Comput Med Imaging Graph, 2014. **38**(3): p. 179-89.

139. Borlotti, A., et al., *Noninvasive determination of local pulse wave velocity and wave intensity: changes with age and gender in the carotid and femoral arteries of healthy human.* J Appl Physiol (1985), 2012. **113**(5): p. 727-35.

140. Rezai, M.R., et al., *A magnetic resonance perspective of the pulse wave transit time by the Arteriograph device and potential for improving aortic length estimation for central pulse wave velocity.* Blood Press Monit, 2013. **18**(2): p. 111-8.

141. Vitarelli, A., et al., *Assessment of ascending aorta wall stiffness in hypertensive patients by tissue Doppler imaging and strain Doppler echocardiography.* Heart, 2010. **96**(18): p. 1469-74.

142. Voges, I., et al., *Normal values of aortic dimensions, distensibility, and pulse wave velocity in children and young adults: a cross-sectional study.* J Cardiovasc Magn Reson, 2012. **14**: p. 77.

143. Muller, J., et al., *Oscillometric carotid to femoral pulse wave velocity estimated with the Vicorder device.* J Clin Hypertens (Greenwich), 2013. **15**(3): p. 176-9.

144. Butlin, M., et al., *Carotid-femoral pulse wave velocity assessment using novel cuff-based techniques: comparison with tonometric measurement.* J Hypertens, 2013. **31**(11): p. 2237-43; discussion 2243.

145. Pierce, G.L., et al., *Aortic pulse wave velocity and reflecting distance estimation from peripheral waveforms in humans: detection of age- and exercise training-related differences.* Am J Physiol Heart Circ Physiol, 2013. **305**(1): p. H135-42.

146. Reusz, G.S., et al., *Reference values of pulse wave velocity in healthy children and teenagers.* Hypertension, 2010. **56**(2): p. 217-24.

147. Reusz, G.S., et al., *Reference values of aortic pulse wave velocity in a large healthy population aged between 3 and 18 years.* J Hypertens, 2013. **31**(2): p. 424-5.

148. Brand, M., et al., *A mismatch between aortic pulse pressure and pulse wave velocity predicts advanced peripheral arterial disease.* Eur J Vasc Endovasc Surg, 2013. **46**(3): p. 338-46.

149. Kallel, F. and J. Ophir, *A least-squares strain estimator for elastography.* Ultrason Imaging, 1997. **19**(3): p. 195-208.

150. Savage, M.T., et al., *Reproducibility of derived central arterial waveforms in patients with chronic renal failure.* Clin Sci (Lond), 2002. **103**(1): p. 59-65.

151. Wanhainen, A., *How to define an abdominal aortic aneurysm--influence on epidemiology and clinical practice.* Scand J Surg, 2008. **97**(2): p. 105-9; discussion 109.

152. Sidloff, D., et al., *Aneurysm global epidemiology study: public health measures can further reduce abdominal aortic aneurysm mortality.* Circulation, 2014. **129**(7): p. 747-53.

153. Ashton, H.A., et al., *The Multicentre Aneurysm Screening Study (MASS) into the effect of abdominal aortic aneurysm screening on mortality in men: a randomised controlled trial.* Lancet, 2002. **360**(9345): p. 1531-9.

154. Lederle, F.A., et al., *Rupture rate of large abdominal aortic aneurysms in patients refusing or unfit for elective repair.* JAMA, 2002. **287**(22): p. 2968-72.

155. Powell, J.T. and A.R. Brady, *Detection, management, and prospects for the medical treatment of small abdominal aortic aneurysms.* Arterioscler Thromb Vasc Biol, 2004. **24**(2): p. 241-5.

156. Darling, R.C., et al., *Autopsy study of unoperated abdominal aortic aneurysms. The case for early resection.* Circulation, 1977. **56**(3 Suppl): p. II161-4.

157. Stather, P.W., et al., *International Variations in AAA Screening.* European journal of vascular and endovascular surgery : the official journal of the European Society for Vascular Surgery, 2013. **45**(3): p. 231-4.

158. Raghavan, M.L., et al., *Wall stress distribution on three-dimensionally reconstructed models of human abdominal aortic aneurysm.* J Vasc Surg, 2000. **31**(4): p. 760-9.

159. Kraft, K.A., V.V. Itskovich, and D.Y. Fei, *Rapid measurement of aortic wave velocity: in vivo evaluation.* Magn Reson Med, 2001. **46**(1): p. 95-102.

160. Boese, J.M., et al., *Estimation of aortic compliance using magnetic resonance pulse wave velocity measurement.* Phys Med Biol, 2000. **45**(6): p. 1703-13.

161. Rabben, S.I., et al., *An ultrasound-based method for determining pulse wave velocity in superficial arteries.* J Biomech, 2004. **37**(10): p. 1615-22.

162. Hartley, C.J., et al., *Noninvasive determination of pulse-wave velocity in mice.* Am J Physiol, 1997. **273**(1 Pt 2): p. H494-500.

163. Cinthio, M., et al., *Longitudinal movements and resulting shear strain of the arterial wall.* American journal of physiology. Heart and circulatory physiology, 2006. **291**(1): p. H394-402.

164. Blacher, J., et al., *Aortic pulse wave velocity as a marker of cardiovascular risk in hypertensive patients.* Hypertension, 1999. **33**(5): p. 1111-7.

165. Safar, H., et al., *Aortic pulse wave velocity, an independent marker of cardiovascular risk.* Arch Mal Coeur Vaiss, 2002. **95**(12): p. 1215-8.

166. Mitchell, G.F., et al., *Changes in arterial stiffness and wave reflection with advancing age in healthy men and women: the Framingham Heart Study.* Hypertension, 2004. **43**(6): p. 1239-45.

167. Mahmud, A. and J. Feely, *Effect of smoking on arterial stiffness and pulse pressure amplification.* Hypertension, 2003. **41**(1): p. 183-7.

168. Tomiyama, H., et al., *Arterial-cardiac destiffening following long-term antihypertensive treatment.* Am J Hypertens, 2011. **24**(10): p. 1080-6.

169. Siebenhofer, A., et al., *The reproducibility of central aortic blood pressure measurements in healthy subjects using applanation tonometry and sphygmocardiography.* J Hum Hypertens, 1999. **13**(9): p. 625-9.

170. Safar, M.E., et al., *Central pulse pressure and mortality in end-stage renal disease.* Hypertension, 2002. **39**(3): p. 735-8.

171. Pini, R., et al., *Central but not brachial blood pressure predicts cardiovascular events in an unselected geriatric population: the ICARe Dicomano Study.* J Am Coll Cardiol, 2008. **51**(25): p. 2432-9.

172. Roman, M.J., et al., *Relations of central and brachial blood pressure to left ventricular hypertrophy and geometry: the Strong Heart Study.* J Hypertens, 2010. **28**(2): p. 384-8.

173. Chemaly, E., et al., *[Comparison of central pulse pressure estimated from pulse wave propagation velocity and carotid pulse pressure measured by applantation tonometry].* Arch Mal Coeur Vaiss, 2002. **95**(7-8): p. 637-40.

174. Agabiti-Rosei, E., et al., *Central blood pressure measurements and antihypertensive therapy: a consensus document.* Hypertension, 2007. **50**(1): p. 154-60.

175. Williams, B., et al., *Differential impact of blood pressure-lowering drugs on central aortic pressure and clinical outcomes: principal results of the Conduit Artery Function Evaluation (CAFE) study*. Circulation, 2006. **113**(9): p. 1213-25.

176. Boutouyrie, P., et al., *Local pulse pressure and regression of arterial wall hypertrophy during long-term antihypertensive treatment.* Circulation, 2000. **101**(22): p. 2601-6.

177. Najjar, S.S., et al., *Pulse wave velocity is an independent predictor of the longitudinal increase in systolic blood pressure and of incident hypertension in the Baltimore Longitudinal Study of Aging.* J Am Coll Cardiol, 2008. **51**(14): p. 1377-83.

178. Filipovsky, J., V. Svobodova, and L. Pecen, *Reproducibility of radial pulse wave analysis in healthy subjects.* J Hypertens, 2000. **18**(8): p. 1033-40.

179. Chen, C.H., et al., *Estimation of central aortic pressure waveform by mathematical transformation of radial tonometry pressure. Validation of generalized transfer function.* Circulation, 1997. **95**(7): p. 1827-36.

180. Trudeau, L., *Central blood pressure as an index of antihypertensive control: determinants and potential value.* Can J Cardiol, 2014. **30**(5 Suppl): p. S23-8.

181. Takazawa, K., et al., *Relationship between radial and central arterial pulse wave and evaluation of central aortic pressure using the radial arterial pulse wave.* Hypertens Res, 2007. **30**(3): p. 219-28.

182. Takazawa, K., et al., *Estimation of central aortic systolic pressure using late systolic inflection of radial artery pulse and its application to vasodilator therapy.* J Hypertens, 2012. **30**(5): p. 908-16.

183. Vappou, J., et al., *Non-invasive measurement of local pulse pressure by pulse wave-based ultrasound manometry (PWUM).* Physiol Meas, 2011. **32**(10): p. 1653-62.

184. Moens, A., *Die Pulskurve.* 1878(Leiden, Netherlands).

185. Korteweg, D., *Uber die Fortpflanzungsgeschwindigkeit des Schalles in Elastiischen Rohren.* Ann Phys Chem, 1878. **5**: p. 52-537.

186. Parati, G., et al., *European Society of Hypertension practice guidelines for home blood pressure monitoring.* J Hum Hypertens, 2010. **24**(12): p. 779-85.

187. Tsukamoto, T., Y. Kitano, and S. Kuno, *Blood pressure fluctuation and hypertension in patients with Parkinson's disease.* Brain Behav, 2013. **3**(6): p. 710-4.

188. Li, R.X., W.W. Qaqish, and E. Konofagou, *Performance assessment of Pulse Wave Imaging using conventional ultrasound in canine aortas ex vivo and normal human arteries in vivo.* Artery Res, 2015. **9**.

189. Luo, J. and E. Konofagou, *A fast normalized cross-correlation calculation method for motion estimation.* IEEE transactions on ultrasonics, ferroelectrics, and frequency control, 2010. **57**(6): p. 1347-57.

190. Cavalcante, J.L., et al., *Aortic stiffness: current understanding and future directions.* J Am Coll Cardiol, 2011. **57**(14): p. 1511-22.

191. Jondeau, G., et al., *Central pulse pressure is a major determinant of ascending aorta dilation in Marfan syndrome.* Circulation, 1999. **99**(20): p. 2677-81.

192. Sun, Z., *Aging, arterial stiffness, and hypertension.* Hypertension, 2015. **65**(2): p. 252-6.

193. Avolio, A.P., M. Butlin, and A. Walsh, *Arterial blood pressure measurement and pulse wave analysis--their role in enhancing cardiovascular assessment.* Physiol Meas, 2009. **31**(1): p. R1-47.

194. Nichols, W.W., *Clinical measurement of arterial stiffness obtained from noninvasive pressure waveforms.* Am J Hypertens, 2005. **18**(1 Pt 2): p. 3S-10S.

195. Philippe, E.G., et al., *A comparison between systolic aortic root pressure and finger blood pressure.* Chest, 1998. **113**(6): p. 1466-74.

196. Van Bortel, L.M., et al., *Non-invasive assessment of local arterial pulse pressure: comparison of applanation tonometry and echo-tracking.* J Hypertens, 2001. **19**(6): p. 1037-44.

197. Fung, Y.C., *Biomechanics : mechanical properties of living tissues*. 2nd ed. ed. 1993, New York ; London: Springer-Verlag.

198. Couade, M., et al., *Quantitative assessment of arterial wall biomechanical properties using shear wave imaging.* Ultrasound Med Biol, 2010. **36**(10): p. 1662-76.

199. Meinders, J.M. and A.P. Hoeks, *Simultaneous assessment of diameter and pressure waveforms in the carotid artery.* Ultrasound Med Biol, 2004. **30**(2): p. 147-54.

200. Mahmoud, A.M., et al., *Noninvasive detection of lipids in atherosclerotic plaque using ultrasound thermal strain imaging: in vivo animal study.* J Am Coll Cardiol, 2013. **62**(19): p. 1804-9.

201. Libby, P., P.M. Ridker, and G.K. Hansson, *Progress and challenges in translating the biology of atherosclerosis.* Nature, 2011. **473**(7347): p. 317-25.

202. Carr, S., et al., *Atherosclerotic plaque rupture in symptomatic carotid artery stenosis.* J Vasc Surg, 1996. **23**(5): p. 755-65; discussion 765-6.

203. Mughal, M.M., et al., *Symptomatic and asymptomatic carotid artery plaque.* Expert Rev Cardiovasc Ther, 2011. **9**(10): p. 1315-30.

204. Ross, R., *The pathogenesis of atherosclerosis: a perspective for the 1990s.* Nature, 1993. **362**(6423): p. 801-9.

205. Hicks, C.W., et al., *Development of a duplex-derived velocity risk prediction model of disease progression in patients with moderate asymptomatic carotid artery stenosis.* J Vasc Surg, 2014. **60**(6): p. 1585-92.

206. Rothwell, P.M., J. Slattery, and C.P. Warlow, *A systematic comparison of the risks of stroke and death due to carotid endarterectomy for symptomatic and asymptomatic stenosis.* Stroke, 1996. **27**(2): p. 266-9.

207. *Beneficial effect of carotid endarterectomy in symptomatic patients with high-grade carotid stenosis.* N Engl J Med, 1991. **325**(7): p. 445-53.

208. Ferguson, G.G., et al., *The North American Symptomatic Carotid Endarterectomy Trial : surgical results in 1415 patients.* Stroke, 1999. **30**(9): p. 1751-8.

209. Beach, K.W., et al., *Standardized ultrasound evaluation of carotid stenosis for clinical trials: University of Washington Ultrasound Reading Center.* Cardiovasc Ultrasound, 2010. **8**: p. 39.

210. Chan, J.M., et al., *Imaging of the vulnerable carotid plaque: biological targeting of inflammation in atherosclerosis using iron oxide particles and MRI.* Eur J Vasc Endovasc Surg, 2014. **47**(5): p. 462-9.

211. Moller, M.J., Z. Qin, and B. Toursarkissian, *Tissue markers in human atherosclerotic carotid artery plaque.* Ann Vasc Surg, 2012. **26**(8): p. 1160-5.

212. Lovett, J.K., P.J. Gallagher, and P.M. Rothwell, *Reproducibility of histological assessment of carotid plaque: implications for studies of carotid imaging.* Cerebrovasc Dis, 2004. **18**(2): p. 117-23.

213. Wasserman, B.A., et al., *Low-grade carotid stenosis: looking beyond the lumen with MRI.* Stroke, 2005. **36**(11): p. 2504-13.

214. Lovett, J.K., et al., *Histological correlates of carotid plaque surface morphology on lumen contrast imaging.* Circulation, 2004. **110**(15): p. 2190-7.

215. Barnett, H.J., et al., *Benefit of carotid endarterectomy in patients with symptomatic moderate or severe stenosis. North American Symptomatic Carotid Endarterectomy Trial Collaborators.* N Engl J Med, 1998. **339**(20): p. 1415-25.

216. Xu, D., et al., *Prediction of high-risk plaque development and plaque progression with the carotid atherosclerosis score.* JACC Cardiovasc Imaging, 2014. **7**(4): p. 366-73.

217. Feinstein, S.B., *Contrast ultrasound imaging of the carotid artery vasa vasorum and atherosclerotic plaque neovascularization.* J Am Coll Cardiol, 2006. **48**(2): p. 236-43.

218. Hellings, W.E., et al., *Composition of carotid atherosclerotic plaque is associated with cardiovascular outcome: a prognostic study.* Circulation, 2010. **121**(17): p. 1941-50.

219. Saba, L., et al., *Imaging of the carotid artery vulnerable plaque.* Cardiovasc Intervent Radiol, 2014. **37**(3): p. 572-85.

220. Naghavi, M., et al., *From vulnerable plaque to vulnerable patient: a call for new definitions and risk assessment strategies: Part I.* Circulation, 2003. **108**(14): p. 1664-72.

221. Finn, A.V., et al., *Concept of vulnerable/unstable plaque.* Arterioscler Thromb Vasc Biol, 2010. **30**(7): p. 1282-92.

222. Sakakura, K., et al., *Pathophysiology of atherosclerosis plaque progression.* Heart Lung Circ, 2013. **22**(6): p. 399-411.

223. Seneviratne, A., et al., *Biomechanical factors and macrophages in plaque stability.* Cardiovasc Res, 2013. **99**(2): p. 284-93.

224. Moreno, P.R., et al., *Detection of lipid pool, thin fibrous cap, and inflammatory cells in human aortic atherosclerotic plaques by near-infrared spectroscopy.* Circulation, 2002. **105**(8): p. 923-7.

225. van den Oord, S.C., et al., *Assessment of carotid atherosclerosis, intraplaque neovascularization, and plaque ulceration using quantitative contrast-enhanced ultrasound in asymptomatic patients with diabetes mellitus.* Eur Heart J Cardiovasc Imaging, 2014.

226. Michel, J.B., et al., *From intraplaque haemorrhages to plaque vulnerability: biological consequences of intraplaque haemorrhages.* J Cardiovasc Med (Hagerstown), 2012. **13**(10): p. 628-34.

227. Fleiner, M., et al., *Arterial neovascularization and inflammation in vulnerable patients: early and late signs of symptomatic atherosclerosis.* Circulation, 2004. **110**(18): p. 2843-50.

228. Bentzon, J.F., et al., *Mechanisms of plaque formation and rupture.* Circ Res, 2014. **114**(12): p. 1852-66.

229. Doherty, T.M., et al., *Calcification in atherosclerosis: bone biology and chronic inflammation at the arterial crossroads.* Proc Natl Acad Sci U S A, 2003. **100**(20): p. 11201-6.

230. Underhill, H.R., et al., *A noninvasive imaging approach to assess plaque severity: the carotid atherosclerosis score.* AJNR Am J Neuroradiol, 2010. **31**(6): p. 1068-75.

231. Brewin, M.P., et al., *Carotid atherosclerotic plaque characterisation by measurement of ultrasound sound speed in vitro at high frequency, 20 MHz.* Ultrasonics, 2013. **54**(2): p. 428-41.

232. Goncalves, I., et al., *Elastin and calcium rather than collagen or lipid content are associated with echogenicity of human carotid plaques.* Stroke, 2004. **35**(12): p. 2795-800.

233. Nightingale, K., *Acoustic Radiation Force Impulse (ARFI) Imaging: a Review.* Curr Med Imaging Rev, 2011. **7**(4): p. 328-339.

234. Dumont, D.M., J.R. Doherty, and G.E. Trahey, *Noninvasive assessment of wall-shear rate and vascular elasticity using combined ARFI/SWEI/spectral Doppler imaging system.* Ultrason Imaging, 2011. **33**(3): p. 165-88.

235. Dumont, D., et al., *ARFI imaging for noninvasive material characterization of atherosclerosis.* Ultrasound Med Biol, 2006. **32**(11): p. 1703-11.

236. Doherty, J., et al., *Comparison of Acoustic Radiation Force Impulse Imaging Derived Carotid Plaque Stiffness with Spatially Registered MRI Determined Composition.* IEEE Trans Med Imaging, 2015.

237. Palmeri, M.L., et al., *Ultrasonic tracking of acoustic radiation force-induced displacements in homogeneous media.* IEEE Trans Ultrason Ferroelectr Freq Control, 2006. **53**(7): p. 1300-13.

238. Czernuszewicz, T.J., et al., *Experimental validation of displacement underestimation in ARFI ultrasound.* Ultrason Imaging, 2013. **35**(3): p. 196-213.

239. Grotberg, J.B. and O.E. Jensen, *Biofluid mechanics in flexible tubes.* Annual Review of Fluid Mechanics, 2004. **36**: p. 121-147.

240. Holzapfel, G.A., *Determination of material models for arterial walls from uniaxial extension tests and histological structure.* J Theor Biol, 2006. **238**(2): p. 290-302.

241. Westenberg, J.J., et al., *Bramwell-Hill modeling for local aortic pulse wave velocity estimation: a validation study with velocity-encoded cardiovascular magnetic resonance and invasive pressure assessment.* J Cardiovasc Magn Reson, 2012. **14**: p. 2.

242. Polak, J.F., et al., *Changes in carotid intima-media thickness during the cardiac cycle: the multi-ethnic study of atherosclerosis.* J Am Heart Assoc, 2012. **1**(4): p. e001420.

243. Segers, P., et al., *Functional analysis of the common carotid artery: relative distension differences over the vessel wall measured in vivo.* J Hypertens, 2004. **22**(5): p. 973-81.

244. Cunha, R.S., et al., *Distension capacity of the carotid artery and ambulatory blood pressure monitoring. Effects of age and hypertension.* Am J Hypertens, 1995. **8**(4 Pt 1): p. 343-52.

245. Minin, O., ed. *Ultrafast Ultrasound Imaging*. Ultrasound Imaging - Medical Applications. 2011, InTech: Rijeka.

246. Zaleska-Dorobisz, U., et al., *Ultrasound elastography - review of techniques and its clinical applications.* Adv Clin Exp Med, 2014. **23**(4): p. 645-55.

247. Ophir, J., et al., *Elastography: ultrasonic estimation and imaging of the elastic properties of tissues.* Proc Inst Mech Eng H, 1999. **213**(3): p. 203-33.

248. Lee, W.N. and E.E. Konofagou, *Angle-independent and multi-dimensional myocardial elastography--from theory to clinical validation.* Ultrasonics, 2008. **48**(6-7): p. 563-7.

249. Provost, J., et al., *Imaging the electromechanical activity of the heart in vivo.* Proc Natl Acad Sci U S A, 2011. **108**(21): p. 8565-70.

250. Naim, C., et al., *Characterisation of carotid plaques with ultrasound elastography: feasibility and correlation with high-resolution magnetic resonance imaging.* Eur Radiol, 2013. **23**(7): p. 2030-41.

251. Bunting, E.A., J. Provost, and E.E. Konofagou, *Stochastic precision analysis of 2D cardiac strain estimation in vivo.* Phys Med Biol, 2014. **59**(22): p. 6841-58.

252. Wissler, R.W., *Athecosclerotic plaques : advances in imaging for sequential quantitative evaluation*. 1991, New York, N.Y.: Plenum Press.

253. Fioranelli, M. and G. Frajese, *Sports cardiology from diagnosis to clinical management*. 2012, Springer: Milan.

254. Zhang, S., et al., *Accuracy of MDCT in assessing the degree of stenosis caused by calcified coronary artery plaques.* AJR Am J Roentgenol, 2008. **191**(6): p. 1676-83.

255. Tan, F.P., et al., *Analysis of flow disturbance in a stenosed carotid artery bifurcation using two-equation transitional and turbulence models.* J Biomech Eng, 2008. **130**(6): p. 061008.

256. Hutchison, K.J. and E. Karpinski, *In vivo demonstration of flow recirculation and turbulence downstream of graded stenoses in canine arteries.* J Biomech, 1985. **18**(4): p. 285-96.

257. Lee, S.E., et al., *Direct numerical simulation of transitional flow in a stenosed carotid bifurcation.* J Biomech, 2008. **41**(11): p. 2551-61.

258. Luo, J. and E.E. Konofagou, *Imaging of wall motion coupled with blood flow velocity in the heart and vessels in vivo: a feasibility study.* Ultrasound Med Biol, 2011. **37**(6): p. 980-95.

259. Ino-Oka, E., et al., *Evaluation of carotid atherosclerosis from the perspective of blood flow reflection.* Clin Exp Hypertens, 2009. **31**(3): p. 188-200.

260. Watanabe, H., et al., *Estimation of intraoperative blood flow during liver RF ablation using a finite element method-based biomechanical simulation.* Conf Proc IEEE Eng Med Biol Soc, 2011. **2011**: p. 7441-5.

261. Teng, Z., et al., *3D critical plaque wall stress is a better predictor of carotid plaque rupture sites than flow shear stress: An in vivo MRI-based 3D FSI study.* J Biomech Eng, 2010. **132**(3): p. 031007.

262. Tang, D., et al., *Effect of stenosis asymmetry on blood flow and artery compression: a three-dimensional fluid-structure interaction model.* Ann Biomed Eng, 2003. **31**(10): p. 1182-93.

263. Park, S., et al., *Computational modeling with fluid-structure interaction of the severe m1 stenosis before and after stenting.* Neurointervention, 2013. **8**(1): p. 23-8.

264. Imparato, A.M., *The carotid bifurcation plaque--a model for the study of atherosclerosis.* J Vasc Surg, 1986. **3**(2): p. 249-55.

265. Schulz, U.G. and P.M. Rothwell, *Major variation in carotid bifurcation anatomy: a possible risk factor for plaque development?* Stroke, 2001. **32**(11): p. 2522-9.

266. Perktold, K. and G. Rappitsch, *Computer simulation of local blood flow and vessel mechanics in a compliant carotid artery bifurcation model.* J Biomech, 1995. **28**(7): p. 845-56.

267. Otsuka, F., A.V. Finn, and R. Virmani, *Do vulnerable and ruptured plaques hide in heavily calcified arteries?* Atherosclerosis, 2013. **229**(1): p. 34-7.

268. Wexler, L., et al., *Coronary artery calcification: pathophysiology, epidemiology, imaging methods, and clinical implications. A statement for health professionals from the American Heart Association. Writing Group.* Circulation, 1996. **94**(5): p. 1175-92.

269. Swirski, F.K. and M. Nahrendorf, *Leukocyte behavior in atherosclerosis, myocardial infarction, and heart failure.* Science, 2013. **339**(6116): p. 161-6.

270. Dong, L., et al., *Cardiovascular magnetic resonance in carotid atherosclerotic disease.* J Cardiovasc Magn Reson, 2009. **11**: p. 53.

271. Oliver, T.B., et al., *Atherosclerotic plaque at the carotid bifurcation: CT angiographic appearance with histopathologic correlation.* AJNR Am J Neuroradiol, 1999. **20**(5): p. 897-901.

272. Matrone, G., et al., *The delay multiply and sum beamforming algorithm in ultrasound B-mode medical imaging.* IEEE Trans Med Imaging, 2015. **34**(4): p. 940-9.

273. Lim, H.B., et al., *Confocal microwave imaging for breast cancer detection: delay-multiply-and-sum image reconstruction algorithm.* IEEE Trans Biomed Eng, 2008. **55**(6): p. 1697-704.

274. Goshtasby, A., *Image and Vision Computing*. On edge focusing, ed. B.-H. Ltd. Vol. 12. 1994.

275. Bergholm, F., *Edge focusing.* IEEE Trans Pattern Anal Mach Intell, 1987. **9**(6): p. 726-41.

276. Apostolakis, I., S. Nandlall, and E. Konofagou, *Piecewise Pulse Wave Imaging (pPWI) for detection and monitoring of focal vascular disease in murine aortas and carotids in vivo.* IEEE Trans Med Imaging, 2015.

277. Hou, G.Y., et al., *Sparse matrix beamforming and image reconstruction for 2-D HIFU monitoring using harmonic motion imaging for focused ultrasound (HMIFU) with in vitro validation.* IEEE Trans Med Imaging, 2014. **33**(11): p. 2107-17.

278. Kononenko, I., *Machine learning for medical diagnosis: history, state of the art and perspective.* Artif Intell Med, 2001. **23**(1): p. 89-109.

279. Bowd, C., et al., *Bayesian machine learning classifiers for combining structural and functional measurements to classify healthy and glaucomatous eyes.* Invest Ophthalmol Vis Sci, 2008. **49**(3): p. 945-53.

280. Kalinli, A., et al., *Performance comparison of machine learning methods for prognosis of hormone receptor status in breast cancer tissue samples.* Comput Methods Programs Biomed, 2013. **110**(3): p. 298-307.

281. Cruz, J.A. and D.S. Wishart, *Applications of machine learning in cancer prediction and prognosis.* Cancer Inform, 2006. **2**: p. 59-77.

282. Beck, D. and J.A. Foster, *Machine learning techniques accurately classify microbial communities by bacterial vaginosis characteristics.* PLoS One, 2014. **9**(2): p. e87830.

283. Libbrecht, M.W. and W.S. Noble, *Machine learning applications in genetics and genomics.* Nat Rev Genet, 2015. **16**(6): p. 321-32.

284. Greenstein, D., et al., *Using multivariate machine learning methods and structural MRI to classify childhood onset schizophrenia and healthy controls.* Front Psychiatry, 2012. **3**: p. 53.

285. McEvoy, F.J. and J.M. Amigo, *Using machine learning to classify image features from canine pelvic radiographs: evaluation of partial least squares discriminant analysis and artificial neural network models.* Vet Radiol Ultrasound, 2013. **54**(2): p. 122-6.

286. Peissig, P.L., et al., *Relational machine learning for electronic health record-driven phenotyping.* J Biomed Inform, 2014. **52**: p. 260-70.

287. Jordan, M.I. and T.M. Mitchell, *Machine learning: Trends, perspectives, and prospects.* Science, 2015. **349**(6245): p. 255-60.

288. Cai, Z., et al., *Classification of lung cancer using ensemble-based feature selection and machine learning methods.* Mol Biosyst, 2015. **11**(3): p. 791-800.

289. Nattkemper, T.W. and A. Wismuller, *Tumor feature visualization with unsupervised learning.* Med Image Anal, 2005. **9**(4): p. 344-51.

290. Prosperi, M.C., et al., *Challenges in identifying asthma subgroups using unsupervised statistical learning techniques.* Am J Respir Crit Care Med, 2013. **188**(11): p. 1303-12.

291. Suzuki, K., et al., *Machine learning in medical imaging.* Int J Biomed Imaging, 2012. **2012**: p. 123727.

292. Bleich-Cohen, M., et al., *Machine learning fMRI classifier delineates subgroups of schizophrenia patients.* Schizophr Res, 2014. **160**(1-3): p. 196-200.

293. Pereira, F., T. Mitchell, and M. Botvinick, *Machine learning classifiers and fMRI: a tutorial overview.* Neuroimage, 2009. **45**(1 Suppl): p. S199-209.

294. Juntu, J., et al., *Machine learning study of several classifiers trained with texture analysis features to differentiate benign from malignant soft-tissue tumors in T1-MRI images.* J Magn Reson Imaging, 2010. **31**(3): p. 680-9.

295. Suzuki, K., *Pixel-based machine learning in medical imaging.* Int J Biomed Imaging, 2012. **2012**: p. 792079.

296. Vlachopoulos, C., et al., *Pulse wave analysis in the assessment of patients with left ventricular assist device.* J Heart Lung Transplant, 2001. **20**(1): p. 98-102.

297. Prince, C.T., et al., *Pulse wave analysis and prevalent cardiovascular disease in type 1 diabetes.* Atherosclerosis, 2010. **213**(2): p. 469-74.

298. Hope, S.A., et al., *Arterial pulse wave velocity but not augmentation index is associated with coronary artery disease extent and severity: implications for arterial transfer function applicability*. J Hypertens, 2007. **25**(10): p. 2105-9.

299. Braber, T.L., et al., *Identifying Coronary Artery Disease in Asymptomatic Middle-Aged Sportsmen: The Additional Value of Pulse Wave Velocity*. PLoS One, 2015. **10**(7): p. e0131895.

300. Kotecha, D., et al., *Radial artery pulse wave analysis for non-invasive assessment of coronary artery disease.* Int J Cardiol, 2013. **167**(3): p. 917-24.

301. Clark, N.R. and A. Ma'ayan, *Introduction to statistical methods to analyze large data sets: principal components analysis.* Sci Signal, 2011. **4**(190): p. tr3.

302. Timmerman, M.E., et al., *Subspace K-means clustering.* Behav Res Methods, 2013. **45**(4): p. 1011-23.

Appendix

Full derivation of the tradeoff between spatial and temporal resolution

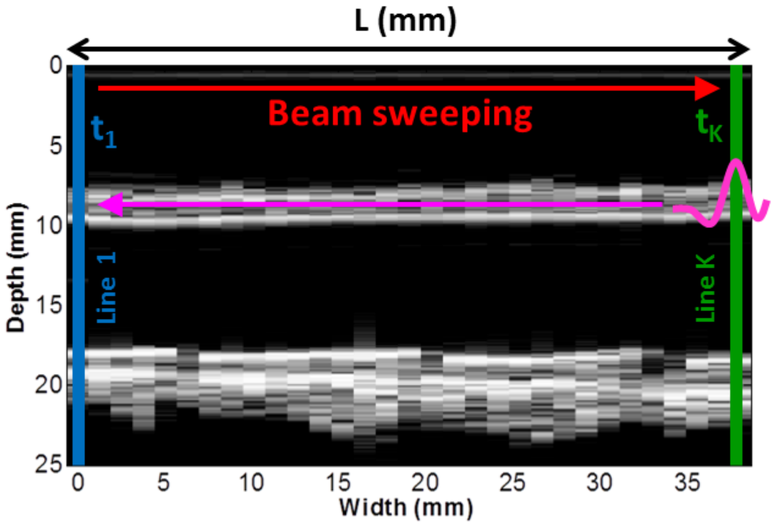

Figure A: B-mode image of an *ex vivo* canine aorta acquired in the reverse scan orientation, used to illustrate the theoretical framework on the tradeoff between temporal and spatial resolution. In the field of view, the pulse wave (pink arrow) propagates in the same direction as that of beam sweeping (red arrow). The pulse wave is captured by beam 1 at time t_1 and reaches the lateral position insonicated by beam K at time $t_K = t_1 + \frac{N}{FR}$ where FR is the frame rate.

Previous PWI studies (Luo *et al* 2012, Vappou *et al* 2010) have recognized that orienting the transducer such that the pulse wave propagates opposite the direction of beam sweeping (i.e. reverse scan) is advantageous because it allows for a wider range of PWVs to be measured. Figure A depicts the B-mode image from an *ex vivo* canine aorta. The entire field of view is covered by sweeping the ultrasound beam from left to right in the imaging plane (red arrow) so that K scan lines are acquired. In the reverse scan orientation, the pulse wave (pink) arrives at the lateral position insonicated by the K^{th} (i.e. right-most) beam and propagates towards the lateral position insonicated by the first (i.e. left-most) beam.

If the pulse wave is captured at the K^{th} scan line position at time t_K and arrives at the first scan line position after N frames, then the pulse transit time is equal to N/FR where FR is the frame rate. The time at which the first beam captures the pulse wave can be expressed as

$$t_1 = t_K + \frac{N}{FR} \qquad \text{[A1]}$$

However, this is the arrival time as “seen” by the imaging system, not the true arrival time. Since the ultrasound beam is being swept across the field of view as the pulse wave is propagating in the opposite direction, the travel time of the beam must be accounted for. In conventional ultrasound, the beam sweeping-induced time delay τ between each scan line is equal to the time to acquire one beam:

$$\tau = \frac{1}{FR*K} \qquad \text{[A2]}$$

The pulse wave arrival time captured by the K^{th} beam is delayed by the time it takes to sweep the ultrasound beam across in the imaging plane, which is equal to $(K\text{-}1)\tau$ seconds. This means that to obtain the true arrival time detected at the first lateral position, the $(K\text{-}1)\tau$ term must subtracted:

$$t_1 = t_K + \frac{N}{FR} - (K-1)\tau \qquad \text{[A3]}$$

The true pulse transit time is then expressed as:

$$\Delta t_{PW} = t_1 - t_K = \frac{N}{FR} - (K-1)\tau \qquad \text{[A4]}$$

Assuming a constant PWV throughout the imaged segment length L, the expected true PWV is expressed as

$$PWV = \frac{L}{\Delta t_{PW}} = \frac{L}{t_1 - t_K} = \frac{L}{\frac{N}{FR} - (K-1)*\tau} = \frac{L}{\frac{N}{FR} - \frac{K-1}{FR*K}} = \frac{L*K*FR}{(K*N)-(K-1)} \qquad \text{[A5]}$$

Eqn. A5 can be used to evaluate the tradeoff between spatial and temporal resolution given a high r^2. Assuming a fixed PWV, increasing the number of scan lines may provide more spatial samples to improve the sensitivity of the PWV measurement at the expense of lower frame rate and fewer temporal samples (i.e. *N*, the number of frames over which the pulse wave propagates). *K*, *FR*, and the transducer orientation are set prior to imaging and *L* is measured within the field of view, leaving *N* as the only parameter that varies depending on the PWV. Therefore, to establish the upper limit on the PWV measurement, the minimum number of temporal samples must be considered. For velocity measurement, the frame rate must be sufficiently high such that the pulse wave can be captured in at least two frames before it travels the length of the imaged segment (i.e. Nyquist rate). Substituting the condition $N \geq 2$ into Eqn. A5, we obtain the upper limit on the PWV measurement:

$$PWV_{max} = \frac{L*K*FR}{(K*2)-(K-1)} = \frac{L*K*FR}{3K-1} = \frac{K}{K+1}(L*FR) \qquad [A6]$$

Any PWV measurement that exceeds the upper limits established by Eqn. A6 may likely have arisen from aliasing due to insufficient frame rate and may be deemed invalid.